

THE UNIVERSITY OF HULL

Biomedical ultrasonics, cavitation, and sonoporation

being a Thesis submitted for the Degree of Doctor of Philosophy

in the University of Hull

by

Mr Spiros Kotopoulos, BEng (Hons)

May 2011

Biomedical ultrasonics, cavitation, and sonoporation

Spiros Kotopoulos

Acknowledgements

First and foremost I would like to thank my academic supervisor **Prof. Dr. Michiel Postema**. It has been an honour to be his first Ph.D. student. His leadership, guidance, attention to detail, support, and continuous hard work have truly set an example I can only hope to match. I am sincerely grateful for all his contributions, ideas, help, and truly countless hours he has spent helping me make this Ph.D. experience extremely productive, stimulating and educational.

I would express my gratitude to my second supervisor, **Prof. Dr. Thomas Walther**. His help in cell culturing was invaluable.

Furthermore, I would like to thank **Prof. Dr. Sandy Cochran** and **Dr. Paul Prentice**, both from The Institute for Medical Science and Technology, The University of Dundee, and **Prof. Dr. Chantal Pichon** from Centre de Biophysique Moléculaire, affiliated to the University of Orléans, for use of their facilities and sharing their knowledge.

I would like to thank **Dr. Andrew Hurrell** from Precision Acoustics, for sharing his knowledge in transducer manufacture and helping me as best possible in his field of expertise. I would like to acknowledge **Mr. Adrian Walker** from the EPSRC Engineering Instrument Loan Pool for his continuous support with the use of high-speed cameras of which without, this work would not be possible.

I would like to thank my fellow Ph.D. student **Anthony Delalande** who has helped to greatly forward our research, and continuously helped me understand the complex world of cell biology.

Finally I would like to thank **The Department of Engineering**, The University of Hull, for its support throughout my whole Ph.D.

Contents

Acknowledgements	3
Symbols and abbreviations	9
1 Introduction and outline	11
1.1 Ultrasound	11
1.2 Transducers	13
1.3 Cyanobacteria	13
1.4 Microfoams	14
1.5 Cavities	14
1.6 Sonopores	14
1.7 Safety	15
2 LiNbO₃ transducers for microsurgery	19
2.1 Introduction	20
2.2 Methodology	21
2.2.1 Lithium niobate	21
2.2.2 Transducer manufacture	22
2.2.3 Acoustic pressure	23
2.2.4 LiNbO ₃ properties	24
2.2.5 Acoustic radiation	25
2.2.6 MRI temperature measurements	25
2.2.7 Tissue sonication	25
2.3 Results and discussion	26
2.3.1 LiNbO ₃ properties	26
2.3.2 Acoustic pressure	26
2.3.3 Acoustic radiation power	28
2.3.4 MRI temperature measurements	28
2.3.5 MRI artefacts	30

2.3.6	Tissue sonication	30
2.4	Conclusions	31
3	Sonic cracking of blue-green algae	35
3.1	Introduction	36
3.2	Material and methods	37
3.2.1	Brightness measurements	39
3.2.2	Viability measurements	40
3.2.3	Post-sonication growth measurements	41
3.3	Results and discussion	41
3.4	Conclusions	46
4	Microfoam formation in a capillary	47
4.1	Introduction	48
4.2	Theory	49
4.3	Materials and methods	52
4.3.1	Ultrasound	54
4.3.2	Ultrasound contrast agent	54
4.4	Results and discussion	55
4.5	Conclusions	63
5	Laser-nucleated ultrasonic acoustic cavitation	65
5.1	Introduction	66
5.2	Methodology	68
5.2.1	Acoustics	68
5.2.2	Optics	71
5.3	High-speed photography	73
5.4	Results and discussion	74
5.5	Conclusions	78
6	Sonoporation at a low MI	81
6.1	Introduction	82
6.1.1	Mechanical index	83
6.1.2	Sonoporation	84
6.2	Materials and methods	86
6.2.1	Sonoporation configuration	86
6.2.2	Fluorescence configuration	87
6.3	Results and discussion	88
6.4	Conclusions	96

	7
7 Summary and discussion	97
List of publications	121
About the author	123

Symbols and abbreviations

		MLTI Θ dimensions
APO	apochromatic	
BW	bandwidth	T^{-1}
CCD	charged coupled device	
c	speed of sound	$L T^{-1}$
c_p	longitudinal wave speed	$L T^{-1}$
d	distance between molecules	L
d_v	vessel diameter	L
E	Young's modulus	$ML^{-1} T^{-2}$
EPI	echo planar image	
F_d	drag force	$ML T^{-2}$
F_r	primary radiation force	$ML T^{-2}$
FUS	focussed ultrasound surgery	
f	center frequency	T^{-1}
f_0	resonance frequency	T^{-1}
f_c	cluster resonance frequency	T^{-1}
h	distance travelled	L
K	bulk modulus	$ML^{-1} T^{-2}$
k	wave number	L^{-1}
HIFU	high-intensity focussed ultrasound	
m	mass	M
MI	mechanical index	
MRI	magnetic resonance imaging	
Mfps	million frames per second	
NA	numerical aperture	
NIR	near infrared	
PVDF	polyvinylidene fluoride	
PZT	lead zirconate titanate	

Nd:YAG	neodymium-doped yttrium aluminium garnet	
p_0	ambient pressure	$ML^{-1} T^{-2}$
p_a	peak rarefactional acoustic pressure	$ML^{-1} T^{-2}$
RF	radio frequency	
R_0	equilibrium radius	L
SODAR	sonic detection and ranging	
SONAR	sound navigation and ranging	
TE	echo time	T
TI	thermal index	
TR	repetition time	T
UV	ultraviolet	
V_{pp}	peak-to-peak voltage	$ML^2 T^{-3} I^{-1}$
v	velocity	LT^{-1}
W	power	$ML^2 T^{-3} ML^2 T^{-3}$
W_{deg}	power needed to raise the temperature by 1°C	$ML^2 T^{-3}$
Z	impedance	$ML^{-2} T^{-1}$
Γ	polytropic exponent	
δ	damping coefficient	
δ_s	shell damping coefficient	
ϵ	shell thickness	L
ζ	electric potential	$ML^2 T^{-3} I^{-1}$
η	dynamic viscosity	$ML^{-1} T^{-1}$
κ	bubble compressibility	$M^{-1} L T^{-2}$
κ_c	cluster compressibility	$M^{-1} L T^{-2}$
κ_f	free gas bubble compressibility	$M^{-1} L T^{-2}$
λ	wave length	L
ν	Poisson's ratio	
ρ	density	ML^{-3}
σ	surface tension	MT^{-2}
$\Delta\phi$	phase difference	
χ	elasticity	MT^{-2}
\varnothing	diameter	L

1

Introduction and outline

1.1 Ultrasound

Sound waves are a form of mechanical vibration. They correspond to particle displacements in matter. Unlike electromagnetic waves, which can propagate in a vacuum, sound waves need matter to support their propagation: a solid, a liquid, or a gas. The ear is an excellent acoustic detector in air but its sensitivity is limited to an interval between 20 Hz and 20 kHz [44]. Audio-frequency sound is essential in communication and entertainment. The acoustics of buildings, particularly concert halls, has been the subject of considerable study. Unwanted audio-frequency sound is called noise. The study of noise and noise control is an important part of engineering.

Ultrasound refers to sounds and vibrations at frequencies above the upper audible limit of 20 kHz to values that can reach 1 GHz, as shown in Figure 1.1. Consequently, ultrasonics involve higher frequencies and smaller wavelengths than audio acoustics. The highest theoretical ultrasonic frequency that can be generated

Based on: Kotopoulis S, Delalande A, Pichon C, Postema M. On cells and sound. In: Korneliussen RJ, Ed. *Proceedings of the 34th Scandinavian Symposium on Physical Acoustics, Geilo, Norway, 30 January – 2 February 2011*. Trondheim: Norwegian Physical Society **2011** accepted; and Chapter 1 of Postema M. *Fundamentals of Medical Ultrasonics*. London: Spon press **2011**.

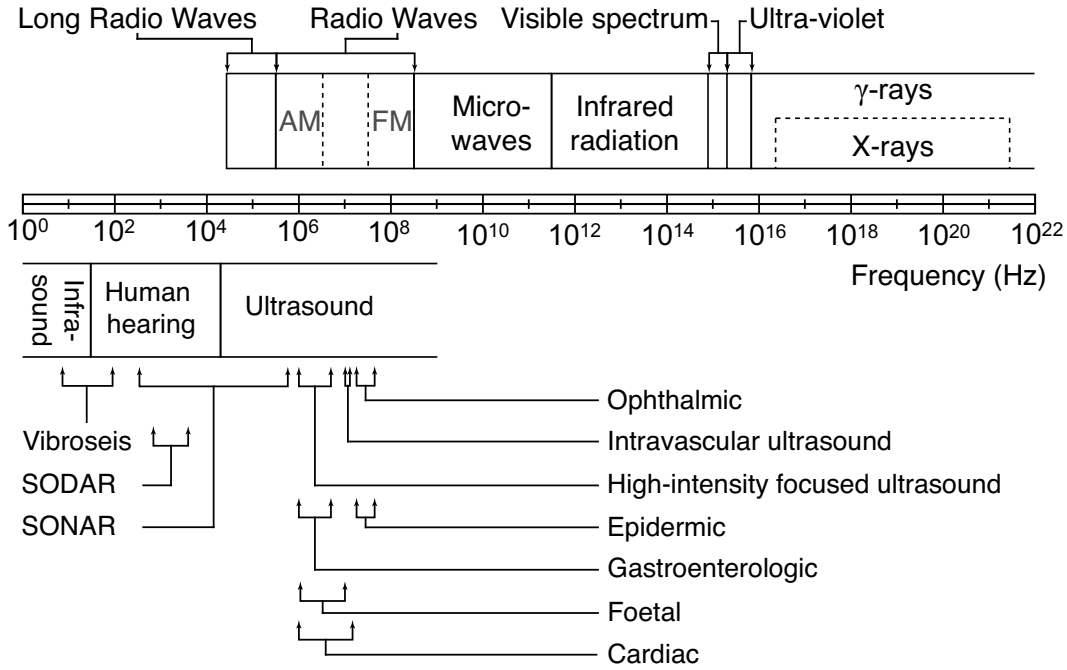


Figure 1.1: Typical applications of electromagnetic (top) and acoustic (bottom) frequencies.

has been elegantly derived by Kuttruff [72]. Consider a crystal consisting of molecules separated by a distance d , through which a monotone longitudinal (pressure) wave with speed c_p is travelling. The phase difference $\Delta\phi$ between two molecules is then

$$\Delta\phi = kd = 2\pi\frac{fd}{c_p}, \quad (1.1)$$

here f is the sound frequency and k is the wave number. Note that the speed of sound is a material property, which depends on the elasticity parameters of the medium and its density. Since the human body consists mostly of water and other fluids [51], transversal (shear) waves are generally ignored in medical ultrasonics. The speed of sound of a medium refers to the speed of the pressure wave through that medium. The speed of sound in blood is slightly higher than that in water [79].

If adjacent masses oscillate in opposite phase, the situation is that of a standing wave. Therefore, the highest theoretical ultrasonic frequency must be the frequency where $\Delta\phi = \pi$ or

$$f = \frac{c_p}{2d}. \quad (1.2)$$

Conversely, infrasound involves sounds and vibrations at low frequencies (below 20 Hz) and long wavelengths. Because the physiological sensation of sound has disappeared at these frequencies, our perceptions of infrasound and ultrasound are different [92]. Ultrasonic waves in fluids and solids are used for non-destructive

evaluation. The general principle is to excite and detect a wave at ultrasonic frequencies and to deduce information from the signals detected. Example applications include the detection of flaws and inhomogeneities in solids, SONAR, SODAR, medical imaging, and acoustic microscopy. The medical ultrasound range is between 0.5 and 100 MHz. Ultrasound as a therapeutic means is increasing in popularity, owing to its non-invasiveness and low cost.

1.2 Transducers

The device used for transmitting and receiving ultrasound is called a transducer. Traditional diagnostic transducers use lead zirconate titanate (PZT) materials to send and receive the ultrasound. The acoustic pressures generated by diagnostic transducers have an upper limit due to de-poling [130]. For some therapeutic applications, where higher acoustic amplitudes are desirable, different piezo-electric materials have been investigated. In Chapter 2 of this thesis the manufacture of a transducer with therapeutic potential using the piezo-electric material lithium niobate is described.

Focussed ultrasound surgery (FUS) is based on the application of high-intensity focussed ultrasound (HIFU) to heat tissue to a temperature that causes protein denaturation and coagulative necrosis [143]. Typical lesions have been found to be ellipsoidal in shape with typical lengths of 1 cm after application of 1-MHz ultrasound [20]. FUS is used for treatment of malignant diseases in bone and breast. Smaller lesions are necessary for microsurgery.

1.3 Cyanobacteria

Such disruptive effects of ultrasound also have applications outside medicine, for instance in ecology. In sonochemistry, large-scale ultrasonic cleaning has become an important field of study. The physical effects were investigated on a smaller scale. Since cyanobacteria contain gas vesicles [10], it was hypothesised that these can be disrupted with the aid of ultrasound. Chapter 3 covers an approach to the eradication of blue-green algae at clinical diagnostic ultrasonic settings.

From the physics point of view, cyanobacteria can be considered as microbubbles with a stiff encapsulating shell, *i.e.*, the cytoskeleton. Hence, the disruption thresholds must be similar as those of ultrasound contrast agents.

1.4 Microfoams

The density and compressibility parameters of blood cells hardly differ from those of plasma [79]. Therefore, blood cells are poor scatterers in the clinical diagnostic frequency range. Since imaging blood flow and measuring organ perfusion is desirable for diagnostic purposes [18, 30, 146], markers should be added to the blood to differentiate between blood and other tissue types. Such markers must be acoustically active in the medical ultrasonic frequency range. The resonance frequencies of encapsulated microbubbles, *i.e.*, gas-filled bubbles with resting diameters between 1 and 10 μm , lie well within the clinical diagnostic frequency range. Based on their acoustic properties, microbubbles are well suited as an ultrasound contrast agent.

In high microbubble concentrations, microbubbles can attract each other and form microfoam. Chapter 4 analyses the formation of microfoam in artificial capillary vessels, using continuous ultrasound at low acoustic amplitudes.

1.5 Cavities

Pre-fabricated ultrasound contrast agents consist of slow diffusibility gas microbubbles encapsulated by biodegradable shells [126]. These have been injected into the blood stream for diagnostic, but more recently, also for therapeutic purposes. However, bubbles can also be generated in the human body without injecting an agent. Inertial cavitation is the formation of new cavities, starting at an inhomogeneity in the liquid, called a cavitation nucleus. Acoustic cavitation and optical cavitation have been of particular interest for noninvasive surgery. Studying acoustic cavitation has been challenging, because its occurrence is hard to control. In Chapter 5, optically nucleated acoustic cavitation is presented.

1.6 Sonopores

It has been proven by numerous groups, that the cellular uptake of drugs and genes is increased, when the region of interest is under sonication, and even more so when an ultrasound contrast agent is present [106]. This increased uptake has been attributed to the formation of transient porosity in the cell membrane, constituted by pores which are big enough for the transport of drugs into cells. If therapeutic agents can be coupled to the shells of ultrasound contrast agent microbubbles or be incorporated inside microbubbles, and these microbubbles could be directed to or

into cells with the use of ultrasound, this could contribute an economic revolution in drug and gene delivery.

To study these rapid cell–ultrasound and cell–microbubble interactions, high-speed photography combined with optical microscopy is required. Phenomena during a single ultrasound cycle need to be recorded at MHz frame rates whereas slower phenomena such as microbubble dissolution or microbubble translation still require kHz frame rates, as opposed to acoustic streaming and fluid flow which can be recorded at standard frame rates.

The transient permeabilisation and resealing of a cell membrane in an ultrasound field is called sonoporation [6]. There are five non-exclusive hypotheses for the sonoporation phenomenon. It has been noted, that, if microbubbles can create pores, it is also possible to create severe cell and tissue damage [7]. There is an inverse correlation between cell permeability and cell viability [48, 60, 86, 140], *i.e.*, not all cell membrane pores are temporary. This indicates that sonoporation is just a transitory membrane damage in the surviving cell [60]. Cell lysis results from irreversible mechanical cell membrane damage [34], which allows intracellular content to leak out [6]. Only recently, ultrasound-induced programmed cell death (apoptosis) has been observed with cancer cells *in vitro* [4, 34], also in the presence of an ultrasound contrast agent [1]. Apart from situations where lysis is desired [87], ultrasonic settings should be chosen such that cell lysis is minimal. Side-effects observed are capillary rupture, haemorrhages, and dye extravasation [7]. These side effects, however, have been associated with relatively high microbubble concentrations, long ultrasonic pulse lengths, and high acoustic intensities [7]. Chapter 6 gives examples of the effects of *in vitro* ultrasound on bubbles and cells.

1.7 Safety

There are three standards for the safe use of biomedical and underwater sound, the mechanical index (MI), the NATO Undersea Research Centre (NURC) Human Diver and Marine Mammal Risk Mitigation Rules and Procedures, and the thermal index (TI). Two of these are represented in Figure 1.2. The MI is a measure for the safe use of clinical diagnostic ultrasound and is defined by:

$$\text{MI} = \frac{p_a}{\sqrt{f}}, \quad (1.3)$$

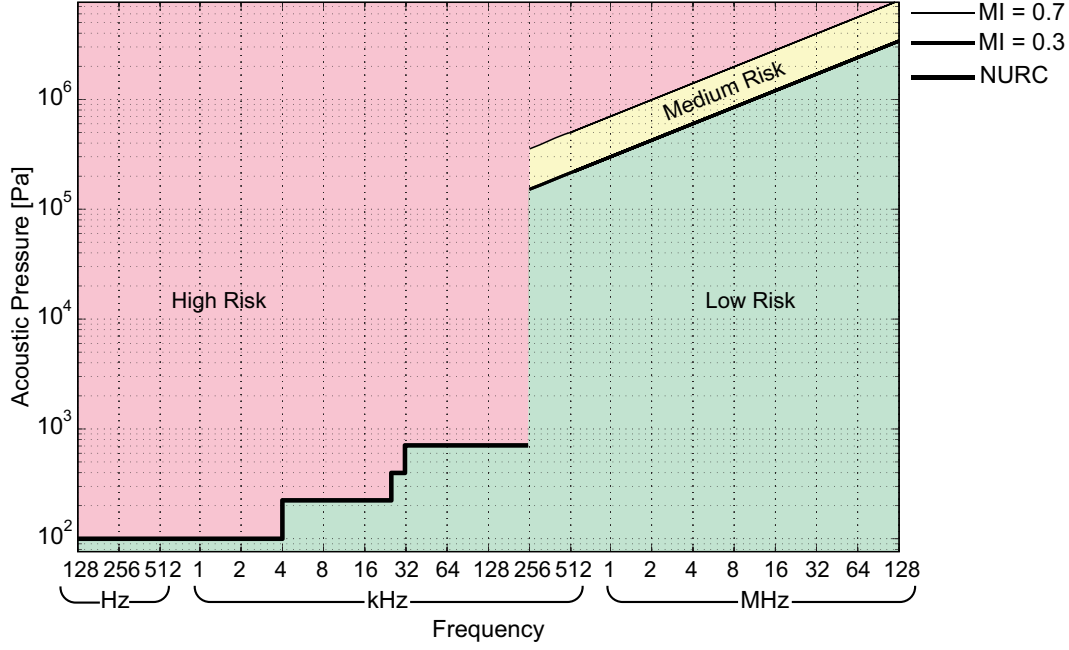


Figure 1.2: Guidelines for the safe use of biomedical sound.

here p_a is the maximum value of peak negative pressure anywhere in the ultrasound field, measured in water but reduced by an attenuation factor equal to that which would be produced by a medium having an attenuation coefficient of $0.3 \text{ dB cm}^{-1} \text{ MHz}^{-1}$, normalised by 1 MPa , and f is the centre frequency of the ultrasound normalised by 1 MHz [90]. For $\text{MI} < 0.3$, the ultrasonic amplitude is considered low. In clinical diagnostics there is a possibility of minor damage to neonatal lung or intestine for $0.3 < \text{MI} < 0.7$ [90]. These are considered moderate acoustic amplitudes. For $\text{MI} > 0.7$, there is a risk of cavitation if gas cavitation nuclei are present, and there is a theoretical risk of cavitation without the presence of ultrasound contrast agents [45]. The risk increases with MI values above this threshold [90]. These are considered high acoustic amplitudes.

According to the NURC Human Diver and Marine Mammal Risk Mitigation Rules and Procedures [91], the maximum acoustic pressure to which mammals can be exposed is 708 Pa at frequencies up to 250 kHz . This corresponds to a mechanical index $\text{MI} < 0.01 \ll 0.3$.

The TI is a measure of tissue heating during ultrasonic exposure. It is defined by

$$\text{TI} = \frac{W}{W_{\text{deg}}}, \quad (1.4)$$

where W is the transmitted power and W_{deg} is the estimated power needed to raise the tissue temperature by 1°C . The TI does not indicate the actual temperature rise in tissue as different tissues have different W_{deg} . For this reason several thermal indices

have been introduced. Three common thermal indices are the thermal index for soft tissue (TIS), the thermal index of bone (TIB) and the thermal index of cranial bone (TIC). The World Federation for Ultrasound in Medicine and Biology Temperature states that a temperature rise of $\leq 1.5^{\circ}\text{C}$ can be used without reservations but an increase of 4°C for 5 minutes is potentially hazardous, whereas the FDA does not regulate the TI [94].

Most obstetric investigation are carried out with MI and TI lower than 1.0; higher values only occur for short periods during Doppler application [26, 120]

When bubbles are present, these safety guidelines may be misleading.

2

Lithium niobate transducers for MRI-guided ultrasonic microsurgery

Abstract

Focused ultrasound surgery (FUS) is usually based on frequencies below 5 MHz, typically around 1 MHz. Whilst this allows good penetration into tissue, it limits the minimum lesion dimensions that can be achieved. In the study reported here, devices that allow FUS at much higher frequencies, therefore in principle reducing the minimum lesion dimensions were investigated. The methodology used to build high-frequency high-intensity transducers using Y-36° cut lithium niobate is explained. This material was chosen as its low losses give it the potential to allow very high-frequency operation at harmonics of the fundamental operating frequency. A range of single element transducers with a centre frequency between

Based on: Kotopoulis S, Wang H, Cochran S, Postema M. Lithium niobate transducers for MRI-guided ultrasonic microsurgery. *IEEE Trans Ultrason Ferroelectr Freq Control* **2011** accepted; and Kotopoulis S, Wang H, Cochran S, Postema M. Lithium niobate ultrasound transducers for high-resolution focussed ultrasound surgery. *Proc IEEE Ultrason Symp* **2010** accepted

This work has been supported by UK EPSRC Grants EP/F037025/1 and EP/G01213X/1, DFG Emmy Noether Programme Grant 38355133, and HERI Research Pump Priming Fund. The authors would like to thank Logitech Ltd. (Glasgow, United Kingdom) for the lapping/polishing and dicing equipment and Alex Volovick of InSightec Ltd. (Haifa, Israel) for assistance with the MRI measurements.

6.6 MHz and 20.0 MHz were built and the transducers' efficiency and acoustic power output were measured. A focussed 6.6-MHz transducer was built with multiple elements operating together and tested using an ultrasound phantom and MRI scans. It was shown to increase phantom temperature by 32°C in a localised area of 2.5 mm × 3.4 mm in the plane of the MRI scan. Tests on poultry tissue were also performed and shown to create lesions of similar dimensions. This study therefore demonstrates that it is feasible to produce high-frequency transducers capable of high-resolution FUS using lithium niobate.

2.1 Introduction

Focused ultrasound surgery (FUS) is based on the application of high intensity focussed ultrasound (HIFU) to heat tissue to a temperature that causes protein denaturation and coagulative necrosis [147]. The required temperature to generate lesions is between 56–60°C [46,52]. The frequency of ultrasound used is generally around 1 MHz, generating characteristic ellipsoidal lesions on the order of 1 cm in length. Higher frequencies in the region of 4 MHz are also used where more precise treatment is needed, for example in the prostate where tumour sizes may be < 1 mm long yet surrounded by sensitive tissue [117]. At such frequencies, conventional piezoelectric transducers can be used, based on hard piezo-ceramic with high drive capability. The use of FUS is increasing as a non-invasive form of surgery and the need for even higher precision is increasing for example for use in aesthetic facial rejuvenation [145], ultrasonic thrombolysis [127] and treatment of malignant disease in breast [55] whilst helping maintain a patient's quality of life when compared to invasive surgery [116].

In this chapter, the type of device that could be used to apply HIFU at much higher frequencies, ultimately targeting 50–100 MHz was considered. As the attenuation coefficient of human tissue has a near linear dependence on frequency [80] greater intensity fields are necessary at higher frequencies in order to be able to penetrate deep enough into human tissue. Piezo-ceramic is expected to be incapable of sustaining sufficiently high-power operation at such frequencies because of mechanical fragility, losses, and electrical breakdown. Instead, the investigation was based on lithium niobate, LiNbO₃ [144]. As a single crystal, this can be thinned easily without disintegrating, unlike ceramics. In addition LiNbO₃ can sustain high electric fields, and its low losses allow the use of harmonics. The use of single crystals and LiNbO₃ for high frequency ultrasound has been explored before, but only for high-resolution imaging [12, 124].

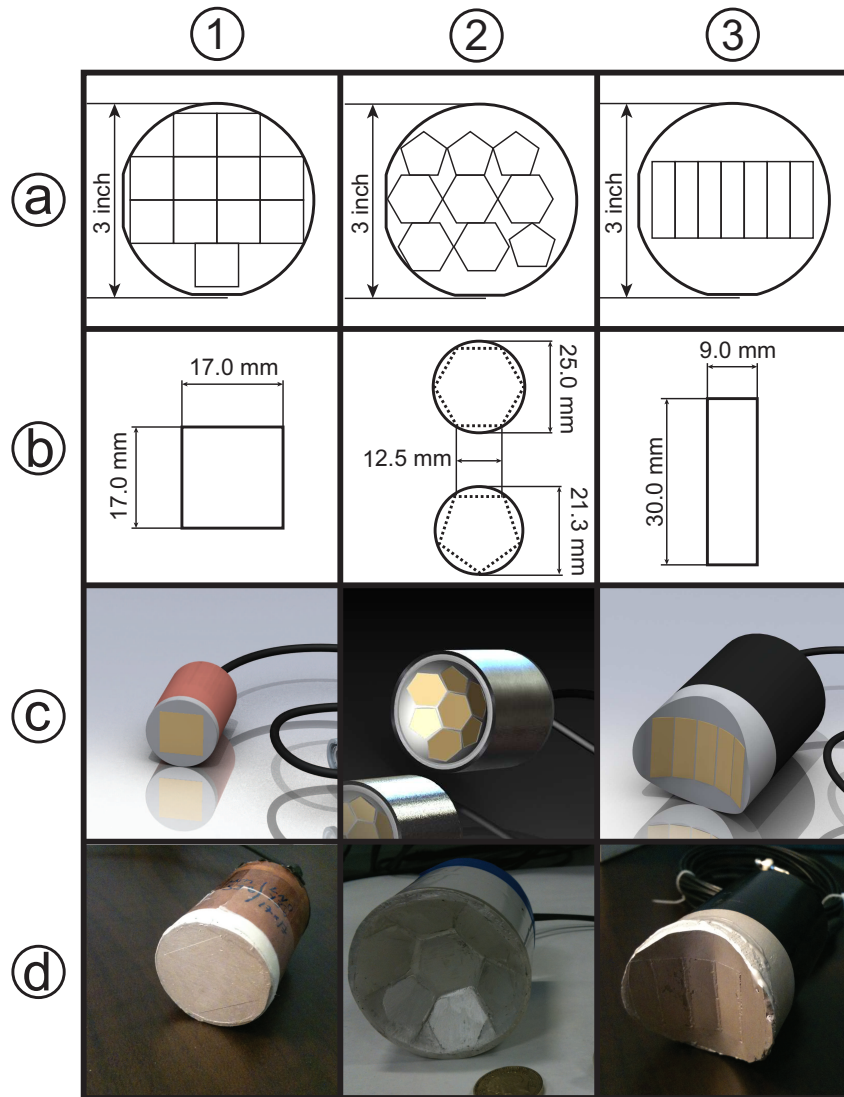


Figure 2.1: Transducer manufacturing: (a) position of plates in single wafer used for each transducer, (b) dimensions of plates for each transducer, (c) computer-aided design representation of transducers, and (d) completed transducers.

2.2 Methodology

2.2.1 Lithium niobate

As it was expected that piezo-ceramics would be unable to produce HIFU at high frequencies and harmonics due to de-poling or cracking, Y-36° LiNbO₃ was explored. As well as its basic advantages, it has a high resonant frequency of 3.3 MHz mm⁻¹, thus allowing for thicker elements at higher frequencies for cost effective manufacturing compared to piezo-ceramics, and it has the highest electromechanical coupling coefficient compared to other LiNbO₃ cuts [142].

2.2.2 Transducer manufacture

Three transducer designs were prepared as shown in Fig.2.1: unfocussed single elements with $17 \times 17 \text{ (mm)}^2$ square LiNbO_3 plates (xDucer 1); a 2D faceted bowl with three pentagonal and four hexagonal plates to mimic a spherically-focussed device (xDucer 2); and a 1D faceted cylindrical section with five, $9 \times 30 \text{ (mm)}^2$ rectangular plates to mimic a cylindrically focussed device (xDucer 3). The equivalent radii of curvature for xDucer 2 and xDucer 3 were 50 mm and 30 mm respectively.

To prepare the plates for each transducer, Y-36° cut, 3-inch diameter, 0.5-mm thick LiNbO_3 wafers (Boston Piezo-Optics, Inc, Boston, MA) were obtained, polished on one side and lapped on the other. Figure 2.1 shows the position of each element from each wafer for each of the three transducer designs. Separation of the plates was performed with a programmable APD1 saw (Logitech Ltd., Glasgow, UK) with a spindle speed of 2900 rpm and a feed rate of 0.160 mm s^{-1} .

For the xDucer 1 devices, the 11 square elements cut from a single wafer were lapped individually in steps of $30 \text{ }\mu\text{m}$ starting from $500 \text{ }\mu\text{m}$ down to $200 \text{ }\mu\text{m}$ using a PM5 precision lapping and polishing machine (Logitech Ltd.). The force applied during lapping was adjusted depending on the sample size, typically in the range 400–900 g. A slurry of $20\text{-}\mu\text{m}$ calcined Al_2O_3 powder in water was used as abrasive. Once the elements reached within $25 \text{ }\mu\text{m}$ of the target thickness, $9\text{-}\mu\text{m}$ calcined Al_2O_3 powder was used to avoid scratching. The lapping machine was programmed to ensure maximum flatness.

The true thickness of the samples was measured and verified at regular intervals using a CG-10 Precision Electronic Measurement System (Logitech Ltd.). Once each element was flat at the desired thickness, it was removed from the glass lapping plate and re-measured to verify the thickness. The elements were continuously checked using a stereo microscope for flaws which could act to concentrate stress and lead to cracking.

An electrode was hand painted on to the lapped side using ELECTRODAG 1415 silver paint (Acheson Colloids BV, Scheemda, Netherlands). Excess paint around the edges was removed using a scalpel and acetone. The polished side of each element was then attached to the adhesive side of Adwill D-210 UV tape (Lintec of America, Inc., Phoenix, AZ). RG174A/U $50 \text{ }\Omega$ coaxial cable was connected to the plates using Ag-loaded conductive epoxy, curing taking place at 80°C for 10 min.

For xDucer 1 devices, Cu tubing with an internal diameter of 28 mm was cut into lengths of 50 mm and placed over the LiNbO_3 plates onto the adhesive side of the UV tape. Epoxy was then introduced around the sides of the LiNbO_3 plate to

join it to the Cu tube. The case for the 2D faceted array, xDucer 2, had a height of 75 mm, outer diameter of 70 mm and a wall thickness of 2 mm. The case for the curvilinear array, xDucer 3, had a height of 75 mm, outer diameter of 50 mm and all thickness of 1.5 mm. For operation within a magnetic resonance imaging (MRI) system, the cases of xDucer 2, and 3 were polyvinyl chloride (PVC), coated with a thin layer of Ag paint so they could be used as the electrical ground connections to the front face of each transducer.

To support the fragile LiNbO_3 , Epofix resin (Struers, Ballerup, Denmark) was mixed with S38 glass microballoons (Lawrence Industries, Tamworth, UK) with a weight ratio of 35 : 65 respectively. The microballoon-epoxy mix was poured into the transducer casing. The xDucer 1 devices were filled to a depth of 16 mm whereas xDucers 2 and 3 were filled to a depth of 22 mm. It was found that the acoustic output of the single element transducers with the backing material was reduced by 5 % when compared to the devices made without backing. The backing was left to cure at room temperature. The earth cable was attached to the shell using conductive Ag-epoxy. The UV tape was then exposed to UV light and peeled off. Any remaining adhesive residue was removed manually.

The exposed LiNbO_3 was cleaned using solvent then the front surfaces and part of each case were painted with Ag paint. The cases were then filled with 5368 silicone (Henkel AG & Co. KGaA, Düsseldorf, Germany) to waterproof the electrical connections and 50- Ω BNC RG-174 plugs were connected to the ends of the coaxial cables.

2.2.3 Acoustic pressure

Each transducer was driven by a continuous wave at its fundamental frequency, generated by an AFG3102 waveform generator (Tektronix, Everett, WA). The signal was passed through a 20-dB attenuator before being used as the input to an RF power amplifier. The single element transducers were tested using a 3100LA, 55-dB RF amplifier (Electronics & Innovation Ltd., Rochester, NY). To test xDucer 2, the pentagonal elements were linked and driven by a 2100L, 50-dB RF amplifier (Electronics & Innovation Ltd.) and the hexagonal elements were linked and driven by the 3100LA amplifier. This was done to give the ability to improve on the alignment of the multiple sound fields by shifting the phase of each group of elements. The pressure outputs were measured using a calibrated fibre-optic hydrophone (Precision Acoustics Ltd., Dorchester, UK) and verified using a calibrated HGL-0200 piezoelectric hydrophone (Onda, Sunnyvale, CA). The curvilinear transducer, (xDucer 3), was tested using a 150A250, 150 RF

Property	Parameter (unit)	Z-cut	Y-36° cut
Density	ρ (kg m ⁻³)	4650	4650
Thickness mode velocity	v (m s ⁻¹)	7380	7260
Acoustic impedance	Z (MRayl)	34.2	33.8
Elastic constants	c_{11}^E (Nm ⁻²) $\times 10^9$	203	185
	c_{33}^E (Nm ⁻²) $\times 10^9$	245	185
	c_{33}^D (Nm ⁻²) $\times 10^9$	252	245
Dielectric constants	$\epsilon_{33}^T/\epsilon_0$	29.8	41.9
	$\epsilon_{33}^S/\epsilon_0$	25.7	37.6
Piezoelectric constants	e_{33} (Cm ⁻²)	1.3	4.47
	h_{33} (Vm ⁻¹) $\times 10^9$	5.71	13.4
	d_{33} (mV ⁻¹) $\times 10^{-12}$	5.15	18.2
Electromechanical coupling coefficient	k_T	0.171	0.495

Table 2.1: Mechanical and Piezoelectric Properties for Lithium Niobate

amplifier (Amplifier Research, Souderton, PA). The acoustic pressure was measured at the acoustic focus, 13 mm from the transducer face using the HGL-0200 hydrophone. For all measurements, the free field was manually scanned using a M-652 x - y - z micro-translation stage (Newport, Didcot, Oxfordshire, UK) to locate the acoustic focus.

2.2.4 LiNbO₃ properties

Data available for the properties of Y-36° LiNbO₃ were found to be limited and incomplete in the literature so values for one-dimensional simulations were obtained using PRAP version 2.2 software (TASI Technical Software Inc, Ontario, Canada) using electrical impedance data from a plate measured using a 4395A

impedance analyser (Agilent, Santa Clara, CA). Table 2.1 shows the measured properties for Y-36° cut LiNbO₃, with figures for Z-cut material shown for comparison. The resonance frequencies of the transducers were also measured using the same impedance analyser.

2.2.5 Acoustic radiation

The acoustic radiation force output of the transducers was measured using an EMS Model 67 ultrasound radiation force balance (EMS Physio Ltd., Wantage, UK). The transducers were placed within 20 mm of the surface of the ultrasound absorber in the balance to ensure that the total radiated flux was incident on it. The output voltage of the waveform generator was increased and the amplifier forward and reflected power, in addition to the transducers acoustic power, were recorded.

2.2.6 MRI temperature measurements

MRI guidance is used for FUS [57] as it allows precise targeting of the HIFU fields and direct temperature measurement at the focus. For MRI-guided focussed ultrasound surgery (MRgFUS) tests in the present work, xDucer 3 and a tissue mimicking DQA Gel Phantom (ATS Laboratories, Bridgeport, CT) placed in a cylindrical perspex chamber filled with tap water were tested in a GE Signa HDx 1.5T MRI system (GE Healthcare, Waukesha, WI). A gradient echo planar image (EPI) was recorded with TE=17.0 ms, TR=230.0 ms, and BW=62.0 kHz to capture the temperature increase of the phantom. The curvilinear transducer was turned on at $t = 0$ s with a peak-to-peak input voltage of 101 V, equivalent to 8 W acoustic power and 32 W forward electrical power. The transducer was turned off after 55 s. The size of the acoustic focus was determined by the area heated above the surrounding phantom ambient temperature.

2.2.7 Tissue sonication

To test the effect of the HIFU field on tissue, two boneless, skinless chicken breasts (Tesco, Cheshunt, UK) were cut into 12, $2 \times 2 \times 8$ (cm)³ strips. The strips were placed in a $10 \times 15 \times 5$ (cm)³ container filled with tap water at room temperature and xDucer 3 was clamped vertically with the acoustic focus on the surface of the tissue. Each sample was sonicated once. For tests beneath the surface of the tissue the transducer was lowered closer to the chicken. In all experiments it was ensured that the transducer surface was not in contact with the tissue. The chicken breast

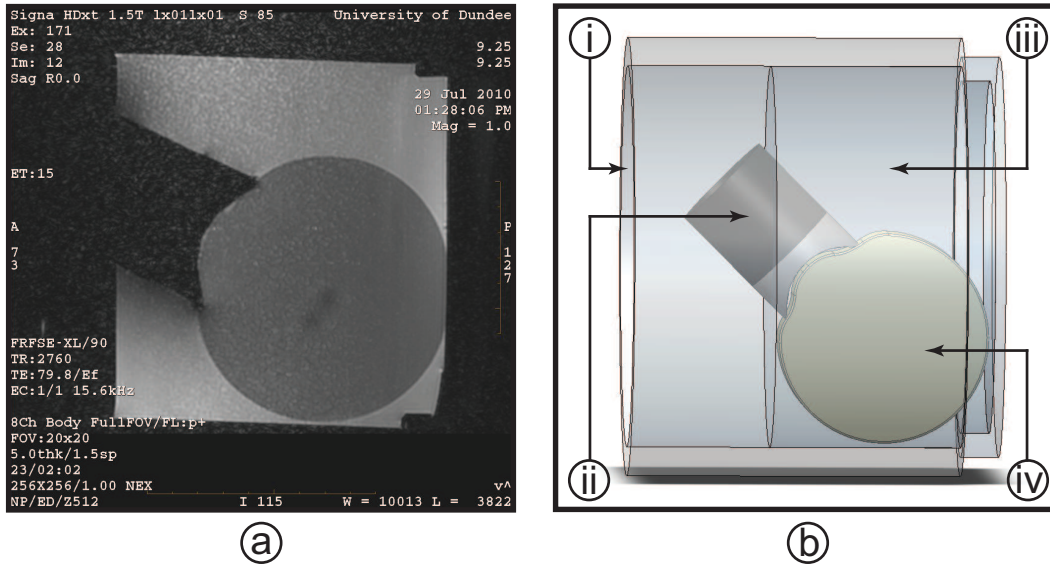


Figure 2.2: (a) MRI side view of sonication setup where brightness indicates water content. Image is rotated 90° anticlockwise from true position. (b) Schematic representation of sonication setup (i) perspex water bath, (ii) xDucer 3, (iii) water, (iv) DQA gel phantom. The transducer generates negligible artefacts in the MRI image. The minor artefacts generated by the silver paint and coaxial cable are not in the acoustic path thus do not affect the image or temperature measurement.

was sonicated using the same settings as in the MRgFUS measurements. Sonication time was increased in steps of 10 s. Lesion sizes were measured manually from digital photographs using ImageJ (National Institutes of Health, Bethesda, MD).

2.3 Results and discussion

2.3.1 LiNbO₃ properties

The resonant frequency and third harmonic of the xDucer 1 devices made with different LiNbO₃ thicknesses are compared to one-dimensional modelling (ODM) for both Z-cut and Y-36° cut LiNbO₃ in Fig. 2.3. Although the simulated Z-cut material gave a higher frequency for a given material thickness, other key properties such as d_{33} and k_T are much lower, hence the preference for Y-36° cut material.

2.3.2 Acoustic pressure

The single element xDucer 1 device produced a maximum peak-to-peak pressure of 14 MPa at the natural acoustic focus of 12 mm from the front face of the

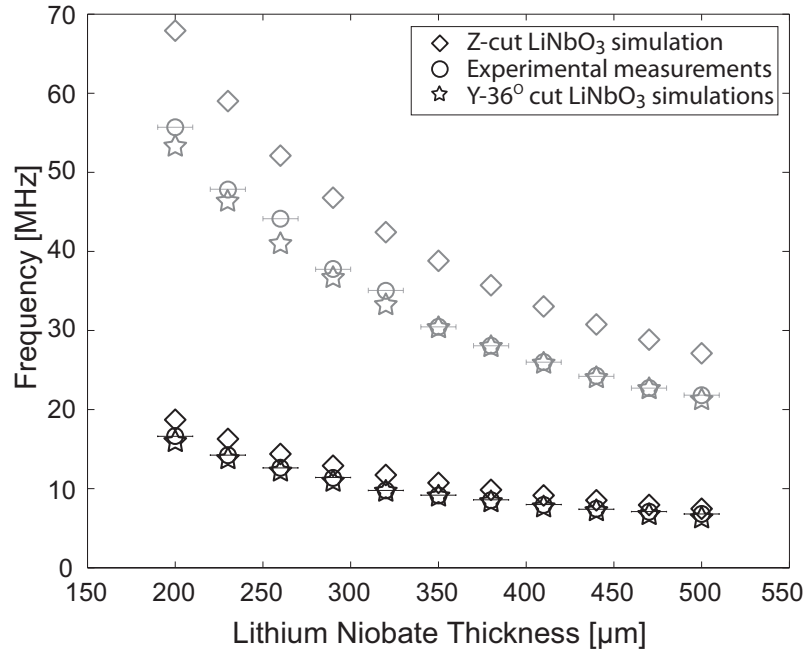


Figure 2.3: Resonance frequency and third harmonic as a function of element thickness for single element LiNbO₃ microballoon backed transducers. The diamonds indicate the Z-cut LiNbO₃ simulations, the circles indicated the experimental measurements and the five-point stars indicate the Y-36° LiNbO₃ cut simulations. The grey data points show the 3rd harmonic.

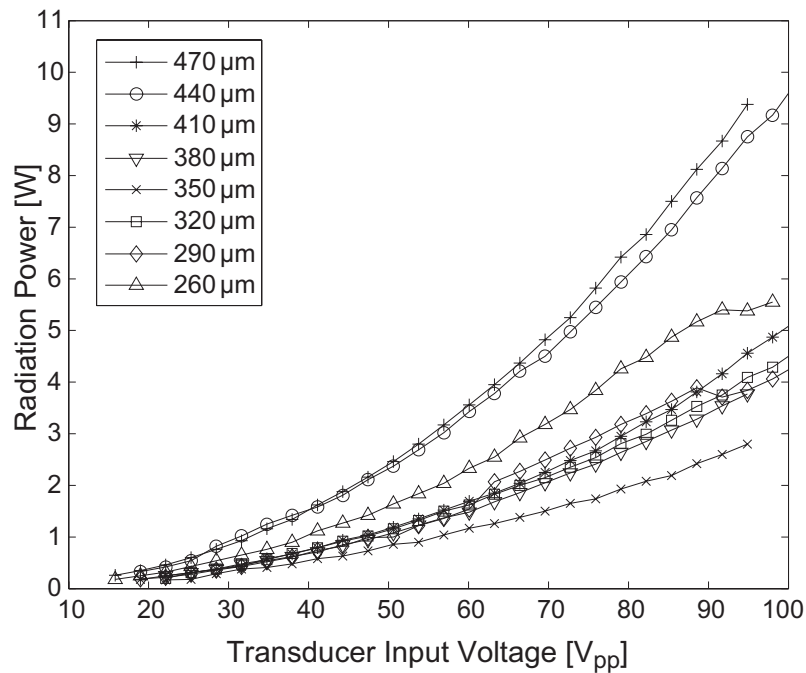


Figure 2.4: Acoustic power as a function of transducer input voltage for 17×17 (mm)² single element LiNbO₃ transducers.

transducer at the fundamental frequency of 6.6 MHz. At the 3rd and 5th harmonics, corresponding to frequencies (wavelengths) of 21 MHz (77 μm) and 35 MHz (44 μm), the xDucer 1 device produced peak-to-peak pressures of 6.6 MPa and 4.3 MPa respectively. The xDucer 2 device generated a modulated sound field. It was possible to improve the output and reduce the envelope frequency of the modulation by shifting the phase of each set of elements. At the resonance frequency of 6.6 MHz the highest peak-to-peak output of 24.3 MPa, equivalent to MI=4.7, and lowest modulation frequency of 550 kHz was achieved with a phase difference of 12°. The curvilinear transducer generated a maximum peak-to-peak pressure of 16.7 MPa at the fundamental frequency of 6.6 MHz, equivalent to MI=3.3.

2.3.3 Acoustic radiation power

The acoustic power generated by the xDucer 1 devices is shown in Fig. 2.4. Efficiency for these devices was found to be 33 \pm 5% throughout the frequency spectrum. The output power is seen to drop as the element thickness decreases. This is due to the increasing electrical impedance mismatch shown in Fig. 2.5. For maximum output power the impedance magnitude and phase should be 50 Ω and 0° respectively. As the element thickness decreases the impedance magnitude also decreases. This is seen for both the fundamental resonance and 3rd harmonic. The phase of the 3rd harmonic increases as the element thickness decreases due to the inductance generated by the cable at higher frequencies. Factors such as amount of Ag-loaded epoxy and cable length were seen to affect the impedance of the transducers [121]. The impedance of the xDucer 3 device in the frequency range from 1–60 MHz is shown in Figure 2.6. The transducer was naturally matched at 7.1 MHz but was not operated at this frequency as the LiNbO₃ was resonant at 6.6 MHz. At 6.6 MHz, its impedance and phase of 46 Ω and 2° respectively, was considered close enough to allow efficient operation. The xDucer 3 device had an efficiency of 25 \pm 2% whereas an industrial 3.28-MHz, 58-mm diameter, PZT, HIFU transducer (Precision Acoustics Ltd.) was measured to have an efficiency of 20 \pm 1%.

2.3.4 MRI temperature measurements

Figure 2.2 is an MRI image of xDucer 3 positioned on the DQA gel phantom. Figure 2.7 shows the area heated by xDucer 3 in the plane of the MRI scan, aligned with its focus. The surface area of heating after 55 s of sonication

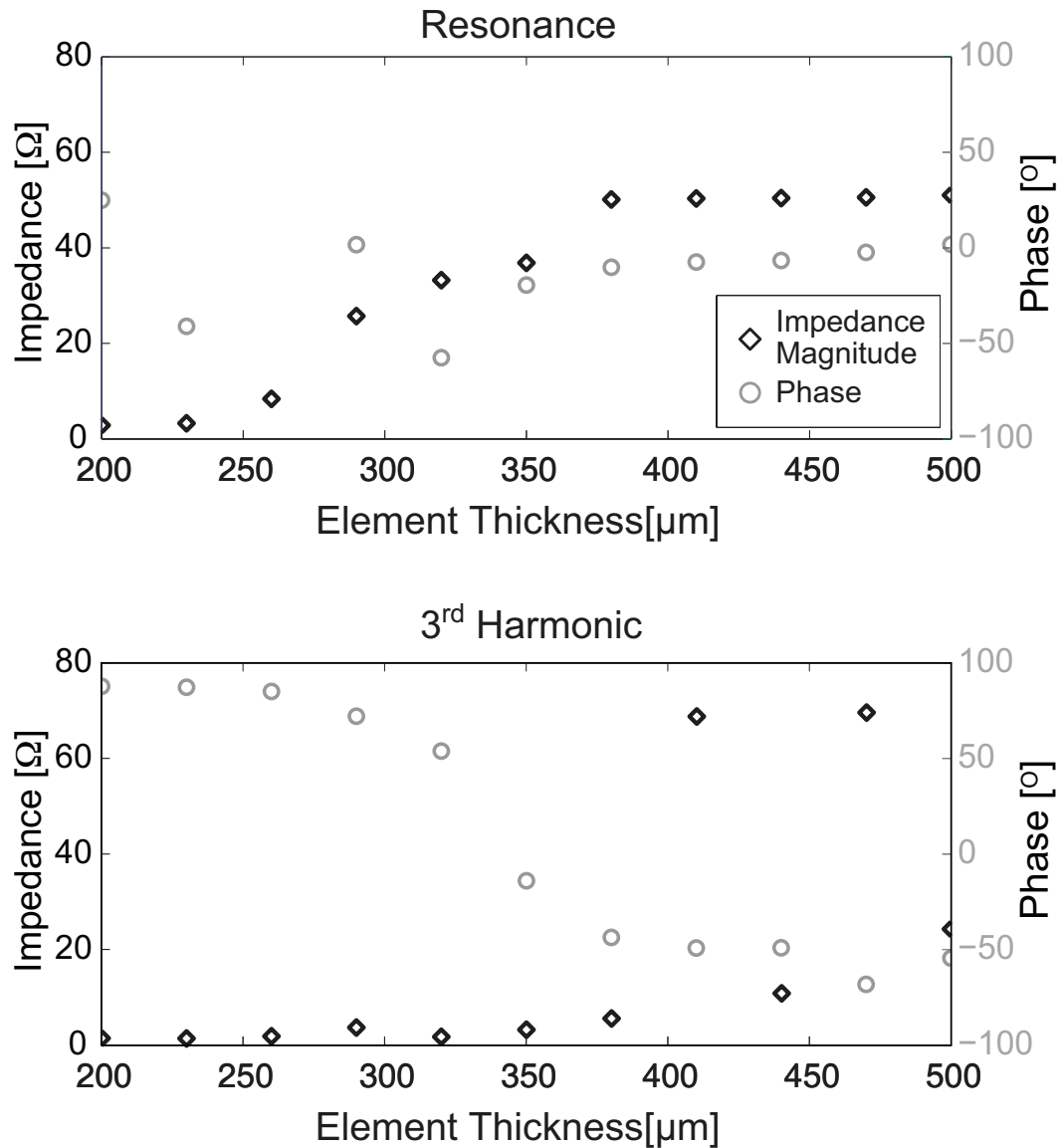


Figure 2.5: Minimum impedance magnitude and equivalent phase as a function of element thickness for single-element LiNbO_3 microballoon-epoxy backed transducers. The black diamonds indicate the impedance magnitude whereas the grey circles indicate the phase.

was $2.5 \text{ mm} \times 3.4 \text{ mm}$. Within 31 s the temperature in the acoustic focus of the transducer had increased 18°C above ambient to a temperature of 38°C . A peak temperature of 52°C was reached after 55 s of sonication, 32°C above ambient, as shown in Fig. 2.8. The acoustic intensity at the focus of the transducer was equivalent to 163 W cm^{-2} . After sonication, cavitation related bubbles formed on the front surface of the transducer, shown in Fig. 2.2.

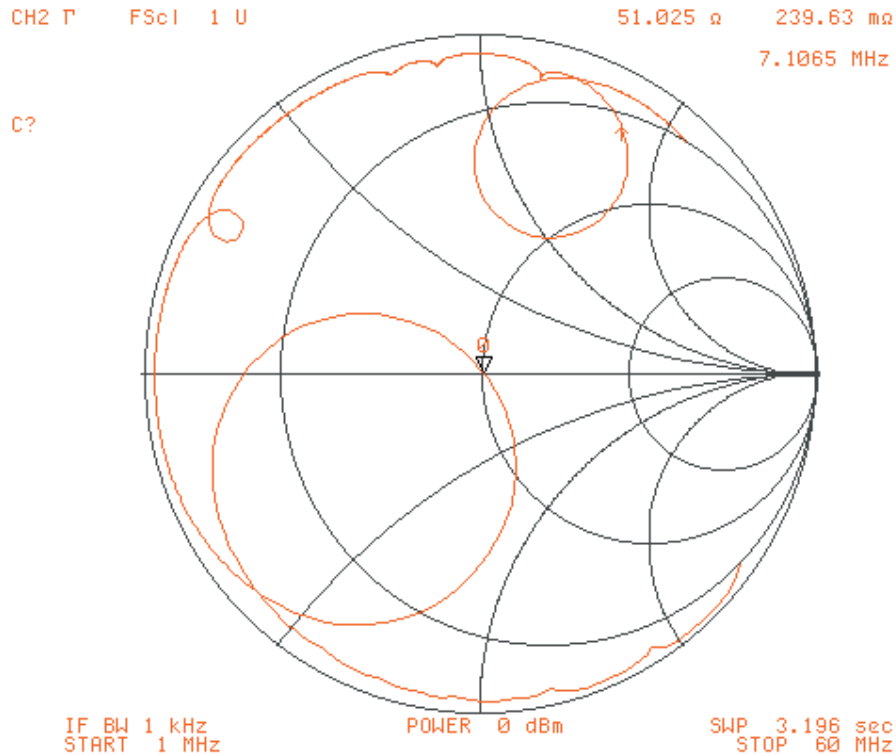


Figure 2.6: Electrical impedance of xDucer 3 device in the frequency range from 1–60 MHz plotted on a Smith chart.

2.3.5 MRI artefacts

Minor artefacts were generated at the PVC/Ag paint boundary seen in Fig. 2.2. These artefacts were not in the vicinity of focus and thus did not influence the MRI results. As better impedance matching values were seen at 7.1 MHz for xDucer 3, both 7.1 MHz and 6.6 MHz were tested in the MRI. Figure 2.9 shows artefacts generated in the MRI image once sonication started at 7.1 MHz. As these artefacts may lead to temperature misreadings, this arrangement was not used. No MRI testing was possible with the single element transducers due to eddy current generated, halo-like artefacts from the copper cases.

2.3.6 Tissue sonication

Figure 2.10 shows the effect of xDucer 3 on chicken breast. An increased sonication time was necessary in order to induce a lesion beneath the tissue surface, of similar size to the MRI measured results. This is partially due to scattering and gas content in the tissue. The lesions dimensions after 90 s of sonication at 6.6 MHz matched those measured with the MRI. In Fig. 2.10ⓐ the chicken has been sliced open to locate the region of coagulation. The lesion was formed 6 mm beneath the

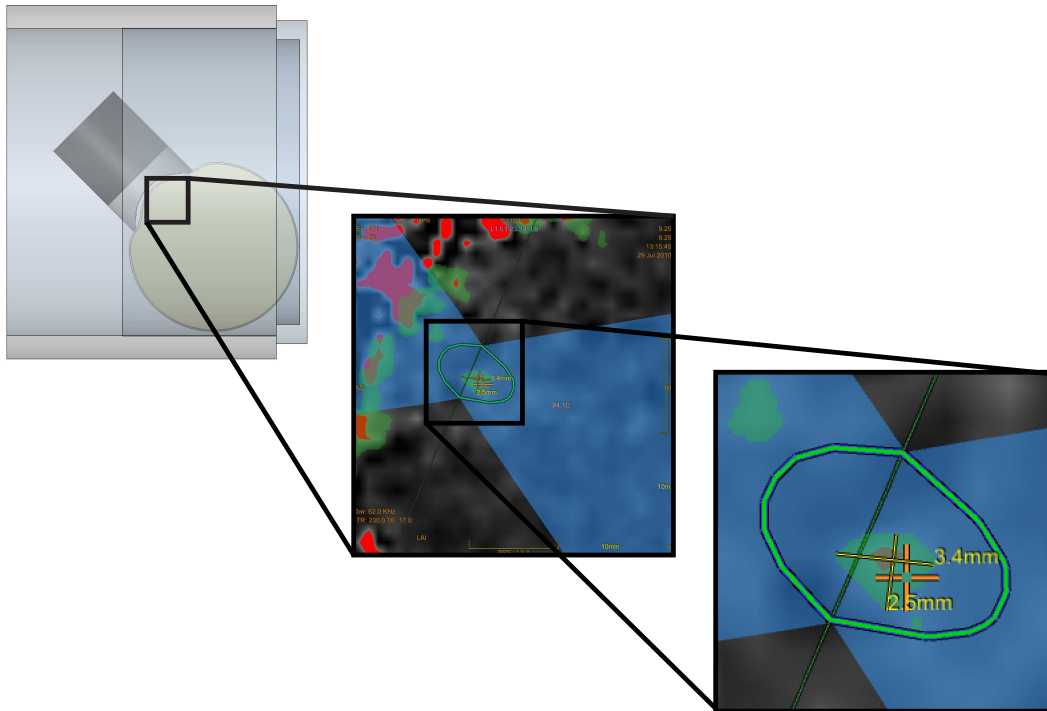


Figure 2.7: MRI view of sonication area. The focal region had a size of $2.5 \times 3.4 \text{ (mm)}^2$. The orange cross indicates the temperature measurement marker. The green areas represent pixels of equal temperature, the blue areas represent the acoustic field, whereas the red areas represent pixels of temperature $> 70^\circ\text{C}$.

surface of the tissue without affecting the upper tissue boundary or the surrounding tissue. Figure 2.11 shows the size of the lesions on the chicken breast as a function of time. The maximum lesion area after 120 s sonication was $16.1 \pm 0.3 \text{ (mm)}^2$, corresponding to a circular lesion of 4 mm diameter. In further tests, after two minutes continuous sonication, when the transducer surface was in contact with the chicken tissue, the LiNbO_3 was hot enough to cause protein denaturation on the chicken surface.

2.4 Conclusions

In conclusion, it has been shown that it is feasible to manufacture high-frequency, high-intensity, focussed ultrasound transducers based on $\text{Y-}36^\circ$ cut LiNbO_3 . In a range of tests, operating frequencies up to more than 50 MHz using the 3rd harmonic of 200- μm thick LiNbO_3 , focal pressures of 4 MPa at 35 MHz, and $\text{MI}=4.7$ at 6.6 MHz were demonstrated. Two of the devices made, with faceted bowl and faceted cylindrical sections respectively, were designed to be operated under MRI guidance. It was shown that this design was successful and have used one of the

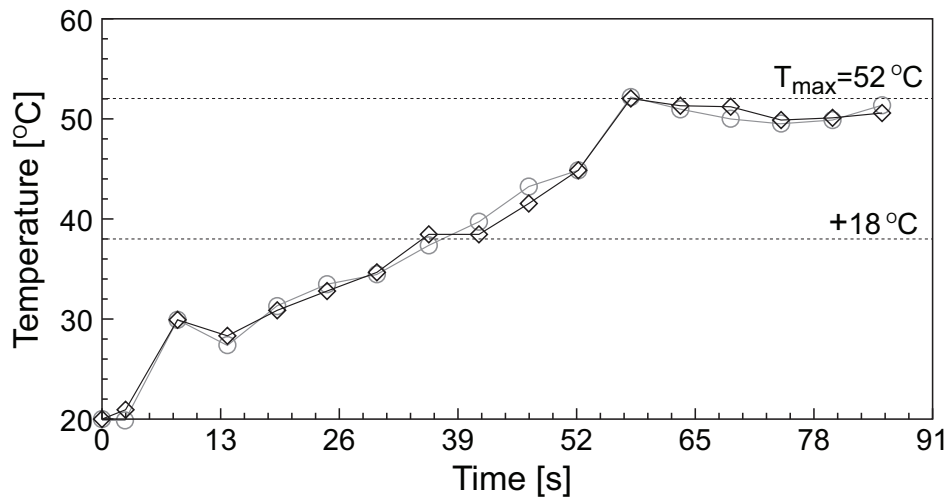


Figure 2.8: Temperature increase was a function of time for xDucer 3 at the acoustic focus in ultrasonic phantom measured using MRI. The black diamonds indicate the temperature of the selected pixel, whereas the grey circles indicate average temperature of the eight surrounding pixels.

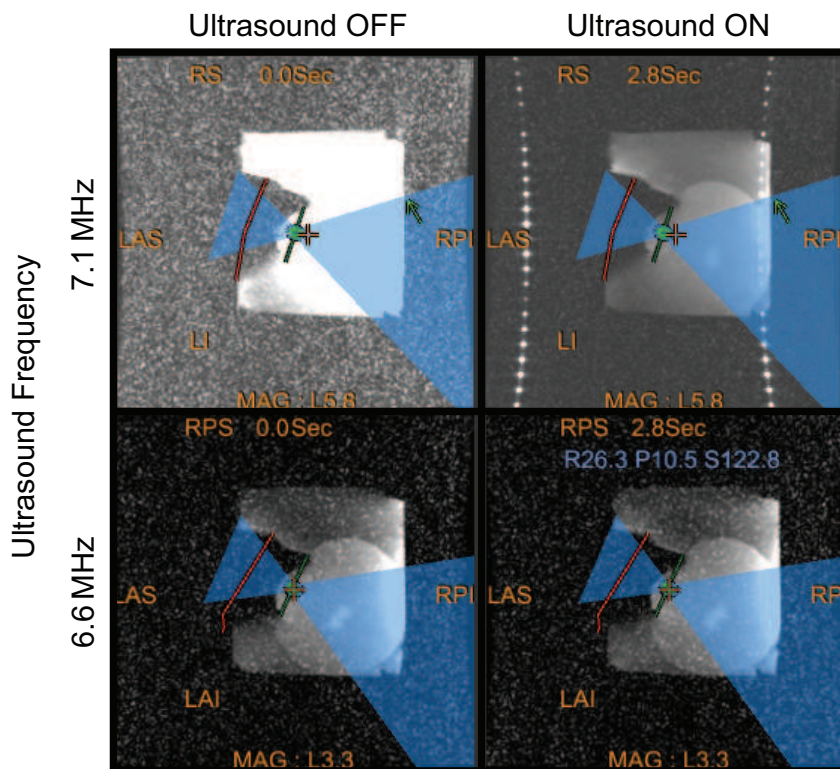


Figure 2.9: MRI view of sonication setup using xDucer 3. During sonication at certain frequencies artefacts are generated with MRI. The blue area represents the acoustic field.

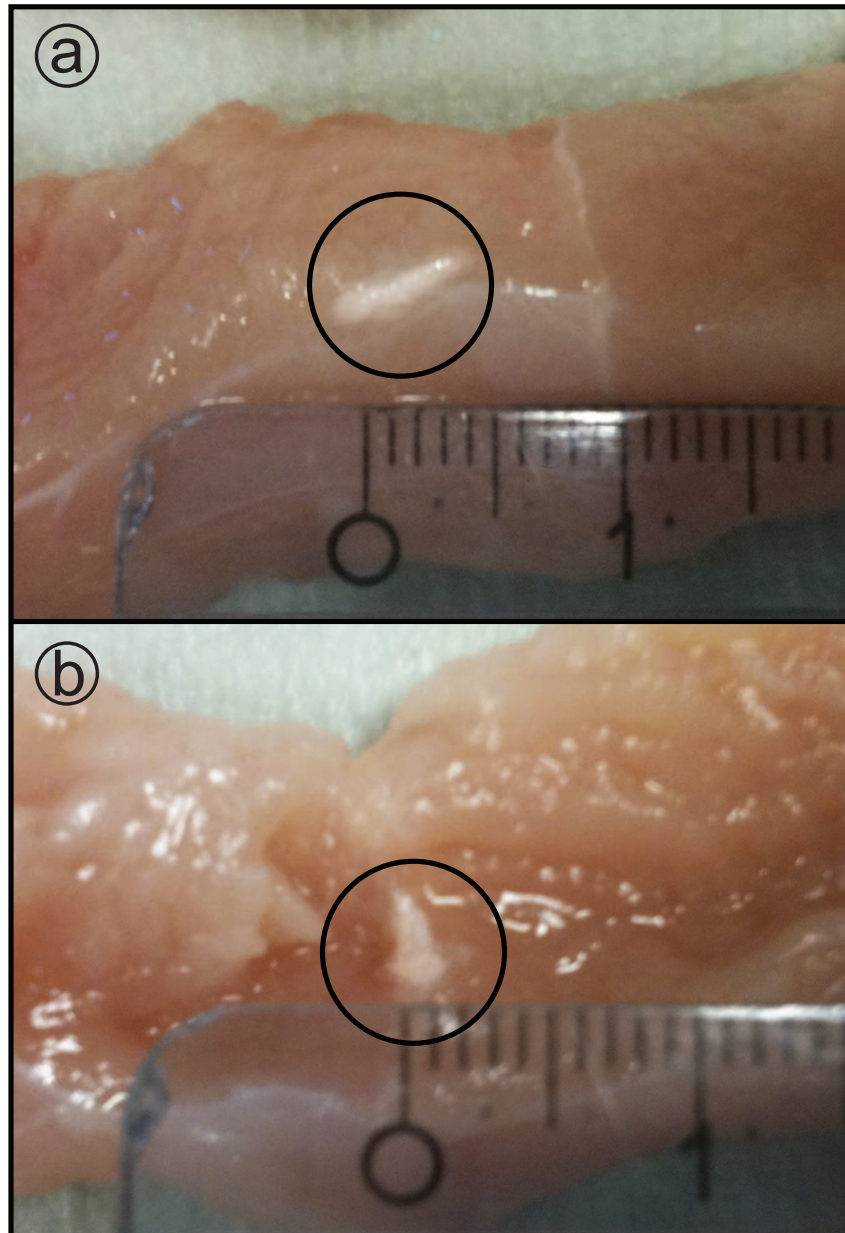


Figure 2.10: Photographs showing lesions formed on chicken tissue using xDucer3. (a) lesion formed after 30 s sonication with the acoustic focus on tissue surface, (b) lesion formed after 90 s sonication with the acoustic focus beneath tissue surface. The lesion was formed 6 mm beneath the tissue surface.

devices to increase the temperature within a gel phantom, measured with MRI, to more than 50°C following sonication of 55 s with an equivalent acoustic intensity of 163 W cm^{-2} . Equivalent sized lesions in chicken tissue after 90 s sonication were also created.

Several aspects can be addressed in order to improve the performance of the transducers. At high acoustic intensities the Ag-paint electrode was damaged.

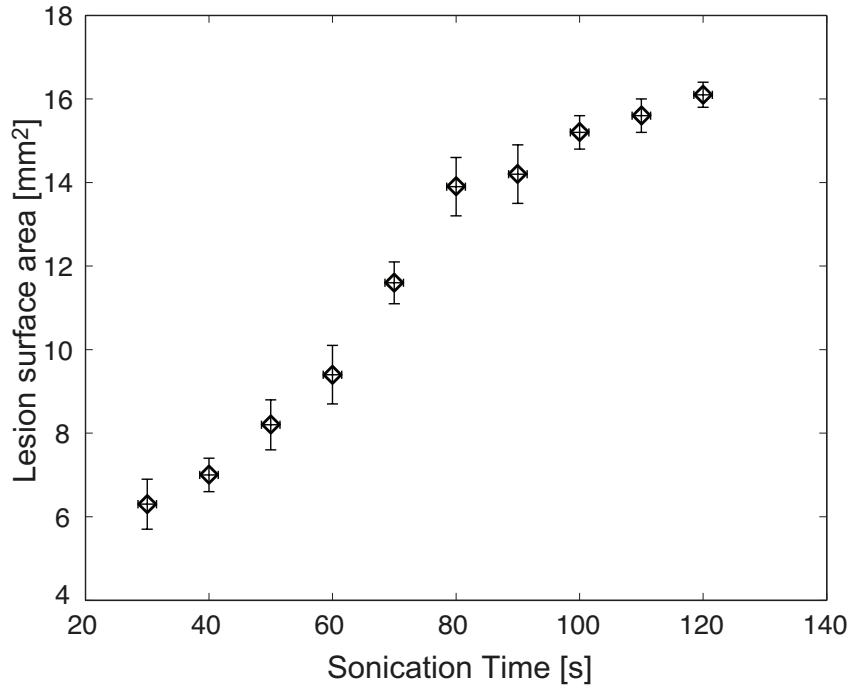


Figure 2.11: Lesion size on chicken breast surface as a function of sonication time using xDucer 3 set at 8-*W* acoustic power output.

This is attributed to air pockets trapped between the electrode and the LiNbO_3 . The use of thin film Cr-Au, Ti-Pt or Al electrodes would be better acoustically and electrically compared to conductive Ag paint [89]. The cases of the devices for MRI guidance were made with PVC tubing coated with Ag paint; using an alternative such as Cu-epoxy composite [40] would aid manufacture and reliability and assist with shielding. The thin LiNbO_3 piezoelectric elements were supported by microballoon-filled epoxy backing; this reduced the transducer output, thus necessitating exploration of support materials with a lower acoustic impedance or other methods to support the plates. Finally, electrical impedance matching was neglected. However, as frequency increases electrical impedance decreases and sustained operation would be enhanced by electrical impedance matching.

3

Sonic cracking of blue-green algae

Abstract

Algae are aquatic organisms classified separately from plants. They are known to cause many hazards to humans and the environment. Blue-green algae strands contain gas vesicles that help them float. At low acoustic amplitudes, microbubbles pulsate linearly but at higher acoustic amplitudes, the elongated expansion phase may result in microbubble disruption; this is known as sonic cracking. It is hypothesised that if the membranes of these gas vesicles are disrupted by means of ultrasound, the gas may be released analogous to sonic cracking, causing the strands to sink. This is a desirable ecological effect, because of the resulting suppressed release of toxins into the water.

Small quantities of blue-green algae of the *Anabaena sphaerica* species were subjected to ultrasound of frequencies and pressures in the clinical diagnostic range, and observed the changes in brightness of these solutions over time. Blue-green algae were forced to sink at all ultrasonic frequencies studied, supporting the

Based on: Kotopoulis S, Schommartz A, Postema M. Sonic cracking of blue-green algae. *Appl Acoust* **2009** 70(10):1306–1312; and Kotopoulis S, Schommartz A, Postema M. Safety radius for algae eradication at 200 kHz–2.5 MHz. *Proc IEEE Ultrason Symp* **2008** 1706–1709.

This work has been supported by EPSRC Grant EP/F037025/1 and the HERI Research Pump Priming Fund. I would like to thank John Adams, The University of Hull, for support with the experimental setup.

hypothesis that the gas vesicles crack under ultrasound sonication in the clinical diagnostic range.

Although the acoustic fields used to eradicate blue-green algae are perfectly safe in terms of mechanical index, the acoustic pressures surpass the NURC Rules and Procedures by over 35 dB. Therefore, caution should be taken when using these techniques in a surrounding where aquatic or semi-aquatic animals are present.

3.1 Introduction

Algae are aquatic, eukaryotic, photosynthetic organisms, ranging in size from single-celled forms to large kelps. Algae are classified separately from plants since they lack true roots, stems, leaves and embryos. Blue-green algae are known to cause many health hazards to humans including skin rashes, gastrointestinal, respiratory [135], allergic reactions [125] and liver cancer [36]. In addition, blue-green algae may have implications on aquatic and semi-aquatic animals [11]. Eutrophication is the increase in chemical nutrients within the ecosystem, causing blooms of algae and plant life and the subsequent decomposition of blue-green algae by bacteria; an oxygen-consuming process [118]. When billions of such bacterial cells die simultaneously after a bloom, the water becomes oxygen-depleted, killing off oxygen-dependent organisms [56].

The main factors that influence algae growth are temperature and light [2, 23]. At low temperatures and low light conditions, the algae do not photosynthesise and therefore do not bloom. Blue-green algae strands contain nitrogen-producing cells (heterocysts) shown in Fig. 3.1, these cells have a diameter between 5 and 7 μm . These store the necessary nitrogen and distribute it to other cells [73].

It is hypothesised that if the membranes of the gas vesicles are disrupted by means of ultrasound, the gas may be released analogous to sonic cracking [102], causing the gas to diffuse and have no means to replenish, thus forcing the strands to sink. At the lake bed, illumination is lower, thus reducing blue-green algae growth. This is a desirable ecological effect, because of resulting suppressed release of toxins into the water.

There are chemical methods to control certain species of blue-green algae but these have side-effects such as promotion and growth of other species of algae [35] whilst also affecting aquatic life in fresh water ponds and lakes. Therefore, ultrasonic algae control has been under investigation [49, 81, 131, 149–151]. In [49, 81, 131, 149–151], ultrasonic sonication of different species of algae led to a decrease in algae concentration in the frequency range 20 kHz–1.7 MHz, which is in

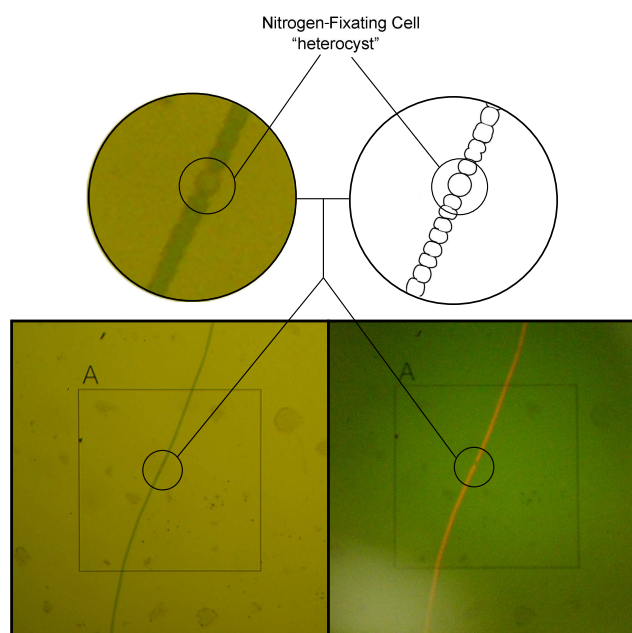


Figure 3.1: Nitrogen-fixing body in *Anabaena sphaerica* algae. Under fluorescent light the body does not illuminate red, proving there is no chlorophyll in the body. Each frame corresponds to $565 \times 565 \mu\text{m}^2$.

contrast with [14], where ultrasound was observed to strengthen the cell membranes of red algae. In these studies the exact acoustic conditions have not been specified other than the frequency and power input. Hence, from the acoustics point of view, they are not repeatable. More importantly, the mechanism causing algae eradication or membrane disruption had not been investigated.

Most commercially available equipment works in the lower ultrasonic range [99]. There have been speculations about the physical mechanism behind the algae eradication, specifically about the role of cavitation. In this study, the effectiveness of ultrasonic sonication in the clinical diagnostic range on *Anabaena sphaerica* was investigated.

In this chapter, acoustic fields in the lower clinical diagnostic range were used, taking into account the MI and NURC guidelines.

3.2 Material and methods

To investigate the effect of diagnostic ultrasound on blue-green algae eradication, three ultrasound transducers were used. A 200-kHz, single element transducer containing a PIC155 piezo crystal (PI Ceramics, Lederhose, Germany), a PA188

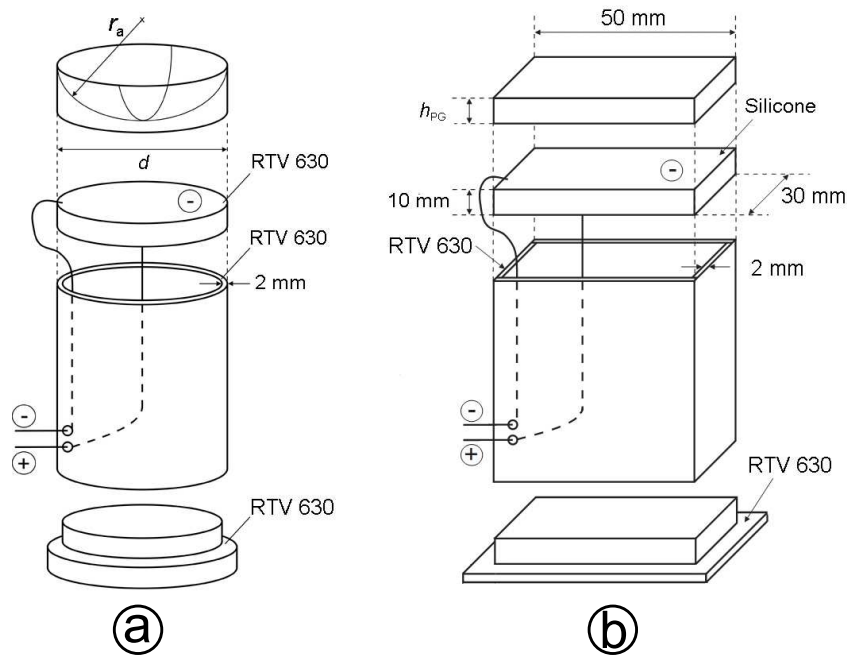


Figure 3.2: (a) 2.2-MHz ultrasound transducer with $d = 1''$ diameter and $r_a = 35$ mm acoustic lens. (b) 200-kHz ultrasound transducer with $h_{PG} = 10$ mm matching layer.

(Precision Acoustics Ltd., Dorchester, UK) 1-MHz, single element transducer, and a 2.2-MHz, single element transducer containing a Pz37 piezo crystal (Ferroperm Piezoceramics A/S, Kvistgård, Denmark). The focal distance of the 2.2-MHz transducer was 73 mm. The design of two transducers is shown in Fig. 3.2. The transducers were subjected to 260-V_{pp} sinusoidal pulses at a 11.8-kHz pulse repetition rate transmitted by a V1.0 pulser-receiver (Sonemat, Coventry, UK). Low acoustic amplitudes were used in order to comply with $MI < 0.3$ [90]. The acoustic amplitudes were measured in a separate water tank in the acoustic foci of the transducers with a 0.2-mm needle hydrophone (Precision Acoustics Ltd.) connected to a TDS 420A digitising oscilloscope (Tektronix Inc, Beaverton). The peak-negative acoustic pressures were 40 kPa for the 1-MHz transducer and 68 kPa for the 2.2-MHz transducer, *i.e.*, $MI \ll 0.1$.

The blue-green algae used were of the *Anabaena* species. The *Anabaena* were obtained from a natural lake and cultured in 2 L of Jaworski's medium [22] at room temperature near a South-facing window in an Erlenmeyer flask for 11 days. Prior to adding the blue-green algae the Jaworski's medium was put in a Swirtlock 2000 autoclave (Astell Scientific, Kent, UK) at 15-lb pressure for 15 minutes.

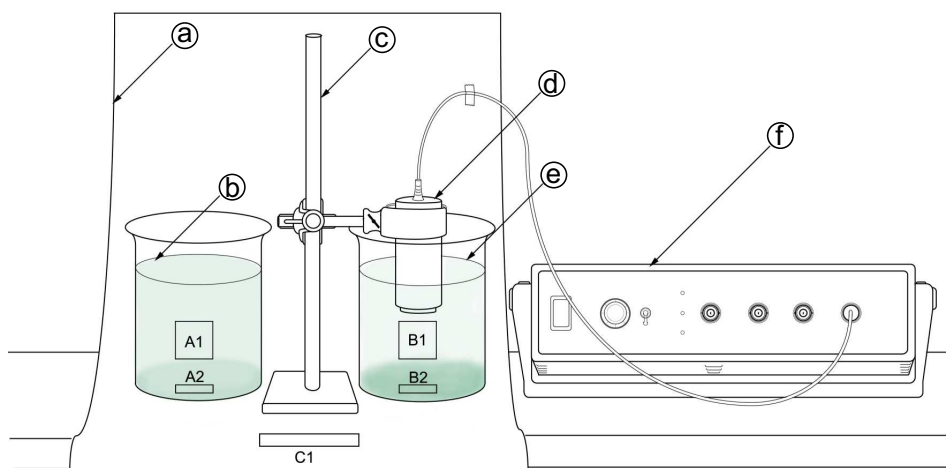


Figure 3.3: Experimental setup: ① white paper sheet; ② control sample; ③ clamp stand; ④ transducer; ⑤ sonicated sample; ⑥ pulser-receiver. Areas A1–B2 represent brightness measurement areas, C1 represents the calibration area.

3.2.1 Brightness measurements

To measure the time-dependent change in brightness of water containing blue-green algae, the culture was split equally into four 250-mL Perspex beakers: one beaker for each transducer and one control beaker. The transducers were inserted separately in each beaker with the acoustic focus within the sample. Each transducer was turned on for 1 hour. The experimental setup is shown in Fig. 3.3. A digital photograph of the solution was taken every five minutes using an EOS 350D digital photo camera (Canon Inc, Tokyo, Japan). The lighting and exposure settings were controlled and maintained throughout the sonication. Full manual settings were used: 100 ISO, shutter speed of 1/50 s, $f3.50$, focal length of 18 mm, no flash, centre weighted metering mode, custom white balance with a B4,0 shift. The digital photographs were converted to 8-bit grey scale. On the photographs of the sonicated solution and control solution, a square area of 160×160 pixels (A1 and B1) in the middle of the beaker, and an area of 160×50 pixels (A2 and B2), at the base of the beaker, was selected, whose average grey-scale depth was calculated using MATLAB[®] (The Mathworks[™], Natick, MA). The change in shade between the first image taken just before sonication and each sequential image after sonication was calculated and graphed for all 18 sonicated and control samples. A white sheet was placed behind the beakers to maintain a constant background. The grey scale of the sheet was also measured and used to calibrate the results. In total, 575 measurements were analysed from 122 photographs.

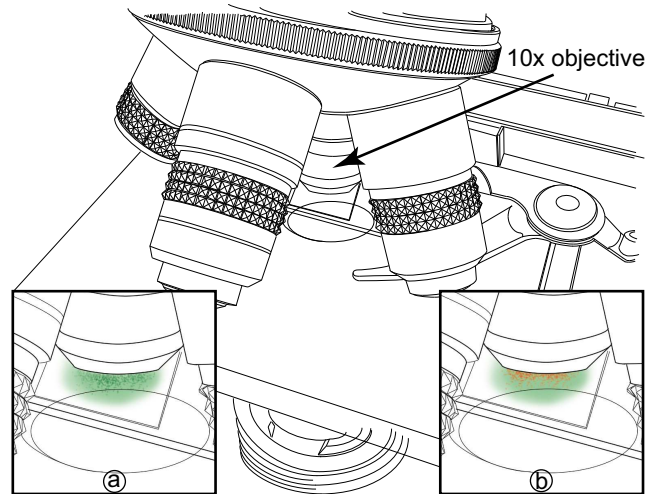


Figure 3.4: Schematic showing use of microscope. A 10× objective lens was used. ① Blue-green algae under tungsten lighting; ② Blue-green algae under fluorescent lighting.

3.2.2 Viability measurements

Every 10 minutes, a 20- μ L sample was taken from the sonicated solution. Samples were put on a test slide and observed through a CHA microscope (Olympus Corporation, Tokyo, Japan) with an MPlan 10 \times /0.30 NA objective lens (Olympus Corporation) *cf.* Fig. 3.4. Digital photographs were captured from the microscope's eye piece using an FE-230 digital camera (Olympus Corporation). Automatic settings were used with *Super Macro* mode and a -1.0 exposure adjustment. From these digital images deterioration in chlorophyll activity and cell damage was determined. To investigate the effect of ultrasound on the viability of the cells, fluorescent light was used. When fluorescent light is projected onto chlorophyll, it is absorbed and re-emitted as a red glow. The red glow denotes that the chlorophyll is still active and can photosynthesise, thus the blue-green algae strands are still alive. Fluorescent light was used as the method to check the viability of the chlorophyll, since it is a standardised and accepted method in detecting chlorophyll activity in plants [83, 138]. Fluorescent light was projected onto these samples for no more than 10 seconds in order to capture the digital image. It may assume that there are no disadvantageous effects of the fluorescent light on the blue-green algae [65, 95]. The samples were discarded after being exposed to fluorescent light.

Three trials of each frequency were performed. One hundred and thirty-one photographs were taken of the microscopic cell structure.

3.2.3 Post-sonication growth measurements

To measure the effect of ultrasound on blue-green algae growth post-sonication, twenty-four 1-mL samples were removed from three solutions that had been subjected to 1 hour sonication with 200-kHz, 1.0-MHz and 2.2-MHz ultrasound and put into a culture tray with 96 compartments. Twenty-four control samples were taken. The culture tray was left in sunlight for 30 days. The grey scale value was measured for each compartment.

3.3 Results and discussion

Figure 3.5 shows the microscopic effect of ultrasound on floating bodies in the blue-green algae solution. From 0 minutes to 60 minutes of sonication, no change was seen in the physical structure of the blue-green algae for all three frequencies. Fluorescent illumination showed that the ultrasound had no effect on the chlorophyll activity for the all frequencies tested. The active chlorophyll shows that the blue-green algae strands are still alive and able to photosynthesise after 60 minutes sonication. This indicates that the ultrasound transmitted does not affect the chlorophyll in the cells.

However, Fig. 3.6 shows that at all frequencies, for the floating bodies, the sonicated samples showed greater brightness than the control samples. For the sunken bodies, all sonicated samples showed reduced clarity when compared to the control samples. Thus, the ultrasound has caused the algae to sink. For example, after 60 minutes, the beakers subjected to 200-kHz sonication were $92 \pm 12\%$ brighter than the control samples, contrasted by the beaker bottoms, which were $53 \pm 27\%$ darker than the control samples.

Clearly, the blue-green algae that were floating in the beaker dropped to the bottom at a faster rate than the control sample. This has been attributed to the disruption of the floating bodies by the ultrasound. This is supported by Fig. 3.7, which shows that the sunken bodies still have active chlorophyll but less dense kelps were found.

Figure 3.8 shows the viability of the culture 30 days after sonication in terms of sample brightness. At 200 kHz, 1.0 MHz, and 2.2 MHz, the samples were $39 \pm 14\%$, $45 \pm 17\%$, and $46 \pm 17\%$ brighter than the control samples, respectively. All samples were significantly brighter than the control samples, even at the lower boundaries of the standard deviation. Thus, these results support the hypothesis that the blue-green algae that have sunk are less capable of multiplying. Hence, sonication may prevent blue-green algae bloom.

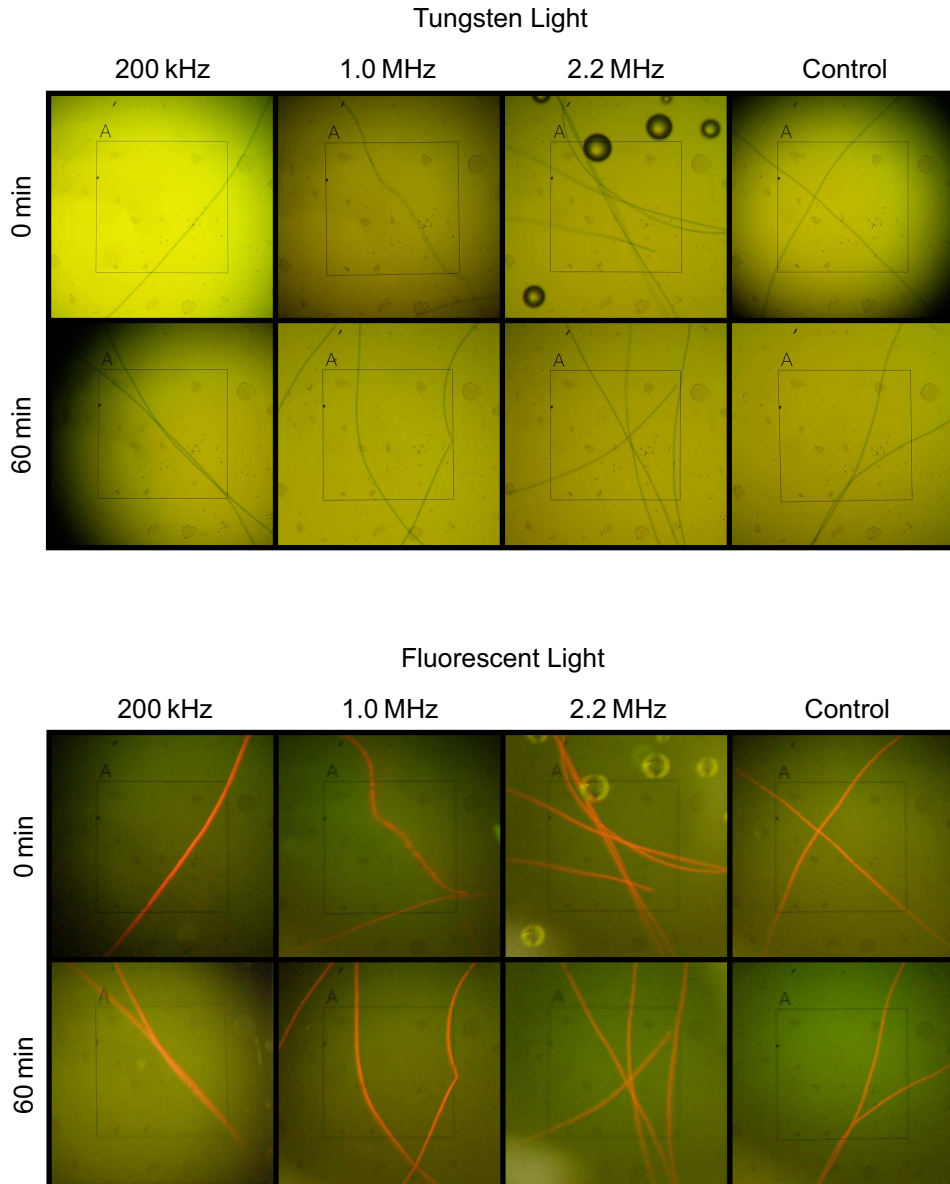


Figure 3.5: Microscopic image sequence showing the effect of 200 kHz–2.2 MHz ultrasound on the floating bodies of blue-green algae. Each frame corresponds to $565 \times 565 \mu\text{m}^2$.

The results can be interpreted as follows. When a gas vesicle is subjected to an ultrasound pulse it expands during the rarefaction phase [111]. If the acoustic amplitude is sufficiently high, the encapsulating membrane cannot withhold the bubble from further expanding, resulting in its rupture. This phenomenon is similar to the sonic cracking of micrometer-sized membrane-encapsulated bubbles observed in [102]. Sonic cracking exclusively occurs during the expansion phase of a bubble [113].

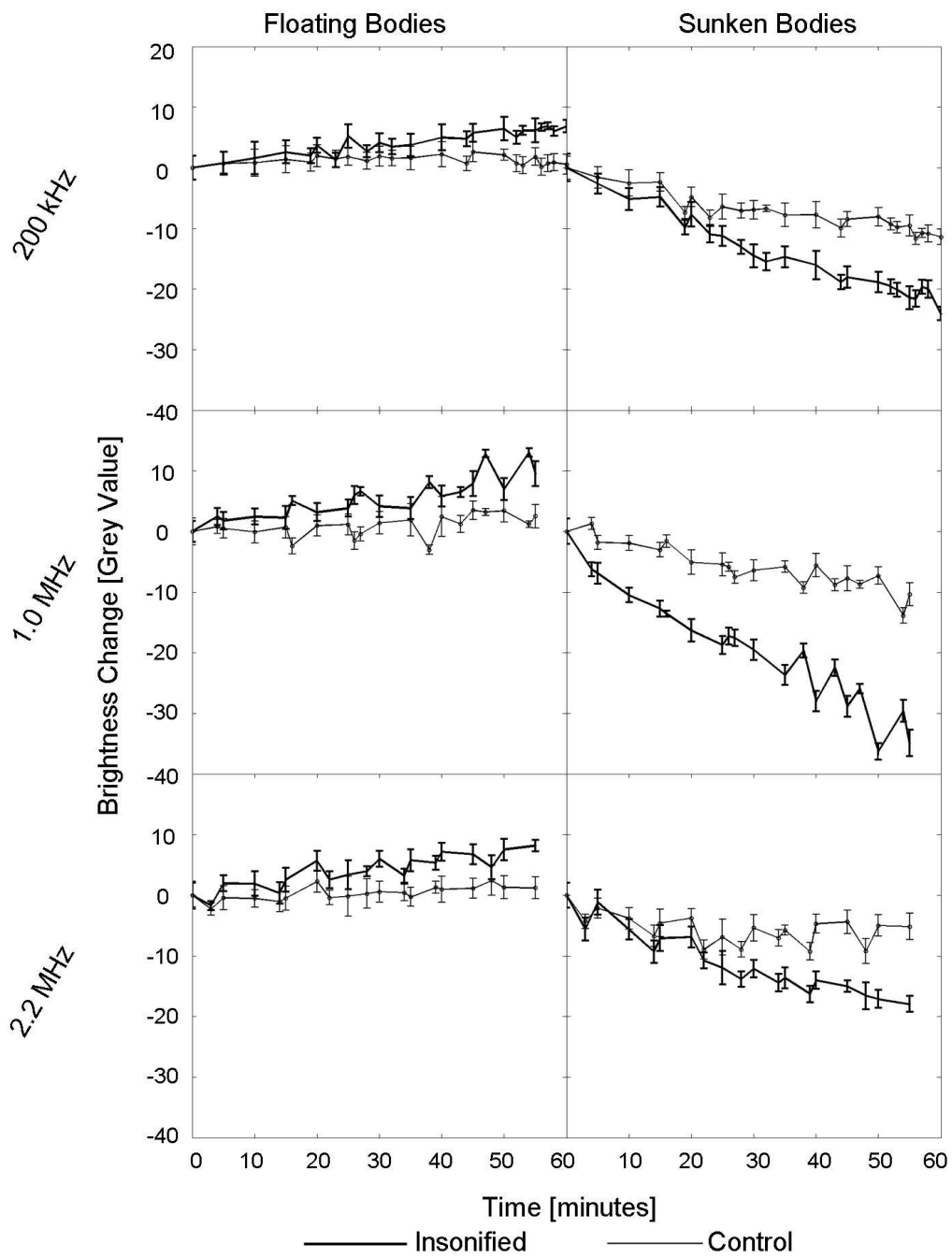


Figure 3.6: Water brightness as a function of ultrasonic exposure time for samples containing floating blue-green algae or sunken blue-green algae.

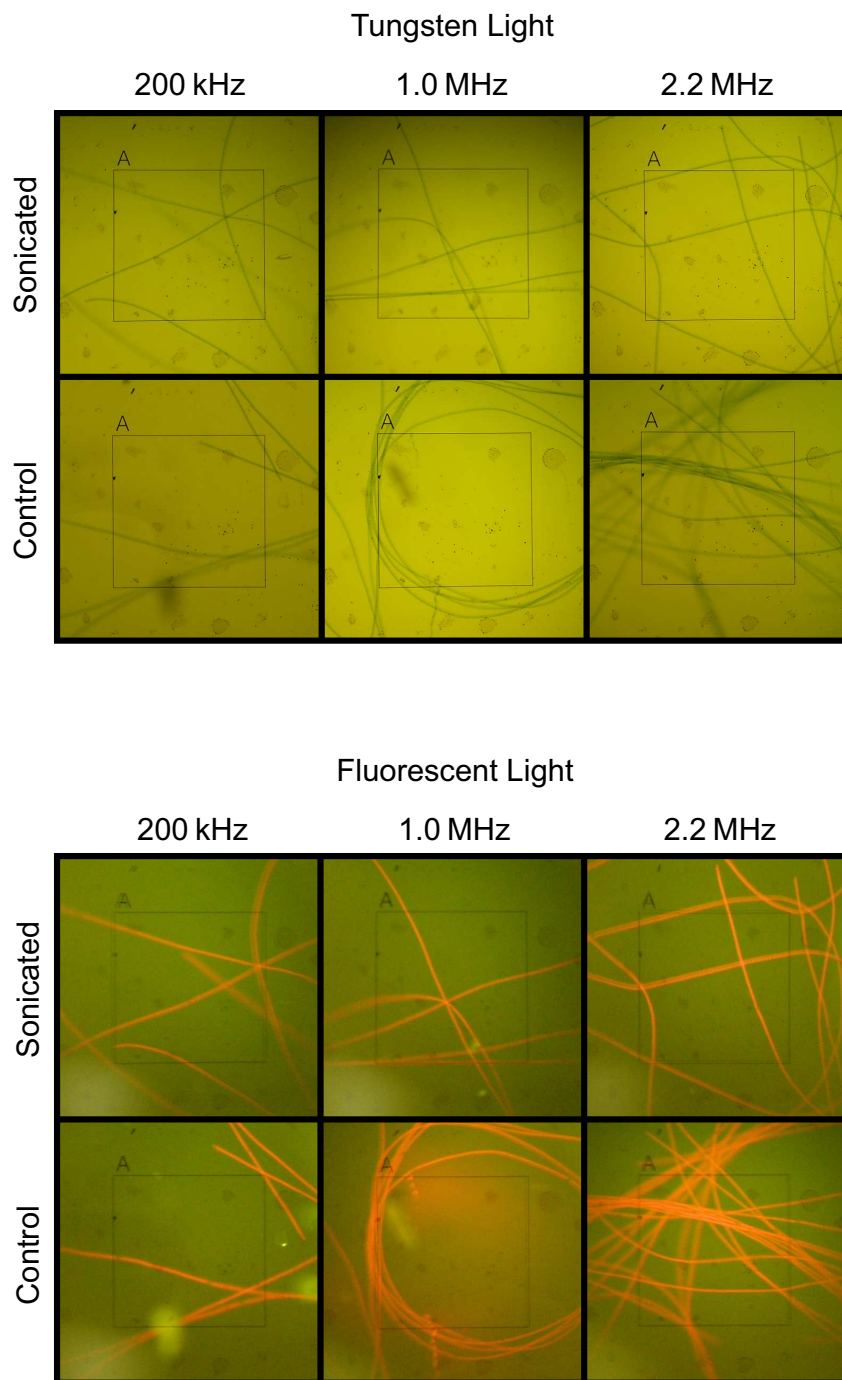


Figure 3.7: Microscopic image sequence showing the effect of 200 kHz–2.2 MHz ultrasound on sunken blue-green algae. Each frame corresponds to $565 \times 565 \mu\text{m}^2$.

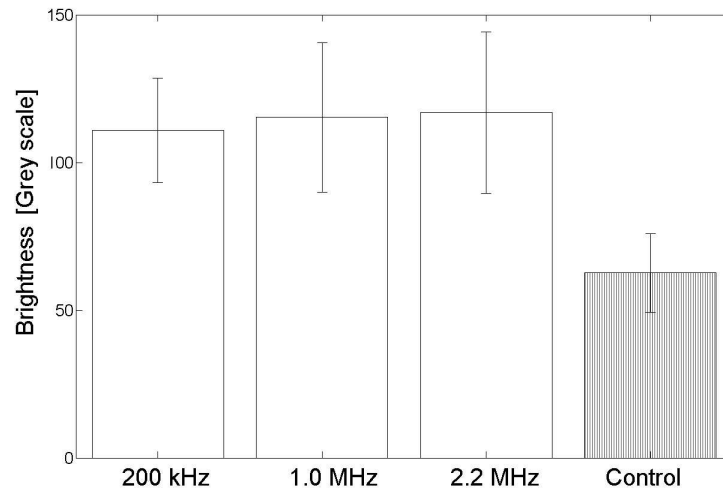


Figure 3.8: Water clarity 30 days after sonication.

The resonance frequency f_0 of a an encapsulated microbubble is given by [110]:

$$f_0 = \frac{1}{2\pi} \sqrt{\left(\frac{3\Gamma}{R_0^2 \rho}\right) \left(p_0 + \frac{2\sigma}{R_0} + \frac{2\chi}{R_0}\right) - \left(\frac{2\sigma + 6\chi}{R_0^3 \rho}\right)}, \quad (3.1)$$

where p_0 is the ambient pressure, R_0 is the bubble radius, Γ is the polytropic exponent of the gas, ρ is the liquid density, σ is the surface tension, and χ is the elasticity of the encapsulation [110]. Using $p_0=1.013 \times 10^5$ Pa, $R_0=3 \mu\text{m}$, $\Gamma=1.4$, ρ is 998 kg m^{-3} , $\sigma=0.072 \text{ N m}^{-1}$, and assuming that the membrane elasticity is similar to that of a lipid encapsulation, $\chi=0.044 \text{ N m}^{-1}$ [42], it can be estimated $f_0 \approx 1 \text{ MHz}$ for *Anabaena* cells used in these experiments. Since the greatest change in clarity was seen at this particular frequency, it can safely be stated that ultrasound sonication close to gas vesicle resonance frequency leads to a more effective eradication.

The quick decrease in live blue-green algae is similar to that in previous studies [49, 81, 131, 149–151]. It can be assumed that the correlation between (high) frequency and algae eradication in these studies is related to the ultrasound proximity to gas vesicle resonance as well.

According to the NURC Rules and Procedures [91], the maximum acoustic pressure to which mammals can be exposed is 708 Pa at frequencies up to 250 kHz. The transducers used had acoustic pressures of 40 kPa and 68 kPa at driving frequencies 1.0 MHz and 2.2 MHz, respectively. These pressures surpass the NURC Rules and Procedures by over 35 dB.

3.4 Conclusions

At any ultrasonic frequency studied, blue-green algae were forced to sink. This supports the hypothesis that the gas vesicles release their gas under ultrasound sonication in the clinical diagnostic range. As supported by previous studies, under identical pulse length and pulse repetition, eradication is most effective close to gas vesicle resonance, at a driving frequency of roughly 1 MHz.

Although the acoustic fields used to eradicate blue-green algae are safe in terms of mechanical index, the acoustic pressures surpass the NURC Rules and Procedures by over 35 dB. Therefore, caution should be taken when using these techniques in a surrounding where aquatic or semi-aquatic animals are present.

4

Microfoam formation in a capillary

Abstract

The ultrasound-induced formation of bubble clusters may be of interest as a therapeutic means, if the clusters behave as one entity, *i.e.*, one mega-bubble, as its ultrasonic manipulation towards a boundary is straightforward and quick. If the clusters can be forced to accumulate to a microfoam, entire vessels might be blocked on purpose using an ultrasound contrast agent and a sound source.

In this chapter, how ultrasound contrast agent clusters are formed in a capillary and what happens to the clusters if sonication is continued, using continuous driving frequencies in the range 1–10 MHz is analysed. Furthermore, high-speed camera footage of microbubble clustering phenomena is shown.

The following stages of microfoam formation were observed within a dense population of microbubbles before ultrasound arrival. After the sonication started, contrast microbubbles collided, forming small clusters, owing to secondary

Based on: Kotopoulis S, Postema M. Microfoam formation in a capillary. *Ultrasonics* **2010** 50(2):260–268; and Kotopoulis S, Postema M. Forming morphing microfoam. *Proc Int Cong Acoust* **2010** #25.

The authors are grateful to Lantheus Medical Imaging, North Billerica, MA, USA, for supplying the ultrasound contrast agent DEFINITY®. This work has been supported by DFG Emmy-Noether Programme grant 38355133, EPSRC grant EP/F037025/1 and the HERI Research Pump Priming Fund.

radiation forces. These clusters coalesced within the space of a quarter of the ultrasonic wavelength, owing to primary radiation forces. The resulting microfoams translated in the direction of the ultrasound field, hitting the capillary wall, also owing to primary radiation forces.

It was demonstrated that as soon as the bubble clusters are formed and as long as they are in the sound field, they behave as one entity. At given acoustic settings, it takes seconds to force the bubble clusters to positions approximately a quarter wavelength apart. It also just takes seconds to drive the clusters towards the capillary wall.

Subjecting an ultrasound contrast agent of given concentration to a continuous low-amplitude signal will make it cluster to a microfoam of known position and known size, allowing for sonic manipulation.

4.1 Introduction

Ultrasound contrast agents are used in diagnostic imaging. They consist of microscopically small bubbles containing slowly diffusing gas encapsulated by biodegradable shells. When inserted in the blood stream, these bubbles oscillate upon ultrasonic sonication, thereby creating detectable ultrasound themselves. A brief overview of the most common ultrasound contrast agents has been presented in [119]. It follows that albumin and lipids are currently the most common bubble encapsulation materials. Because of the proven feasibility to attach therapeutic compounds to albumin and lipids, therapeutic application of contrast agents have become of interest [69, 77, 104, 136]. It is desirable that the therapeutic load of any such contrast agent is released close to the vessel wall. Therefore, pushing bubbles towards boundaries by means of primary radiation forces has been studied [24]. Both primary and secondary radiation forces resulting from oscillating bubbles, may cause the repulsion or mutual attraction, and eventual collision and coalescence, of contrast agent bubbles. This phenomenon has been less studied.

From the therapeutic point of view, the formation of bubble clusters may be of interest. If the clusters behave as one entity, *i.e.*, one mega-bubble, its ultrasonic manipulation towards a boundary is fairly straightforward and quick. If the clusters can be forced to accumulate to a microfoam, entire vessels might be blocked on purpose using an ultrasound contrast agent and a sound source.

In this chapter, how ultrasound contrast agent clusters are formed and what happens to the clusters if sonication is continued is analysed. Furthermore,

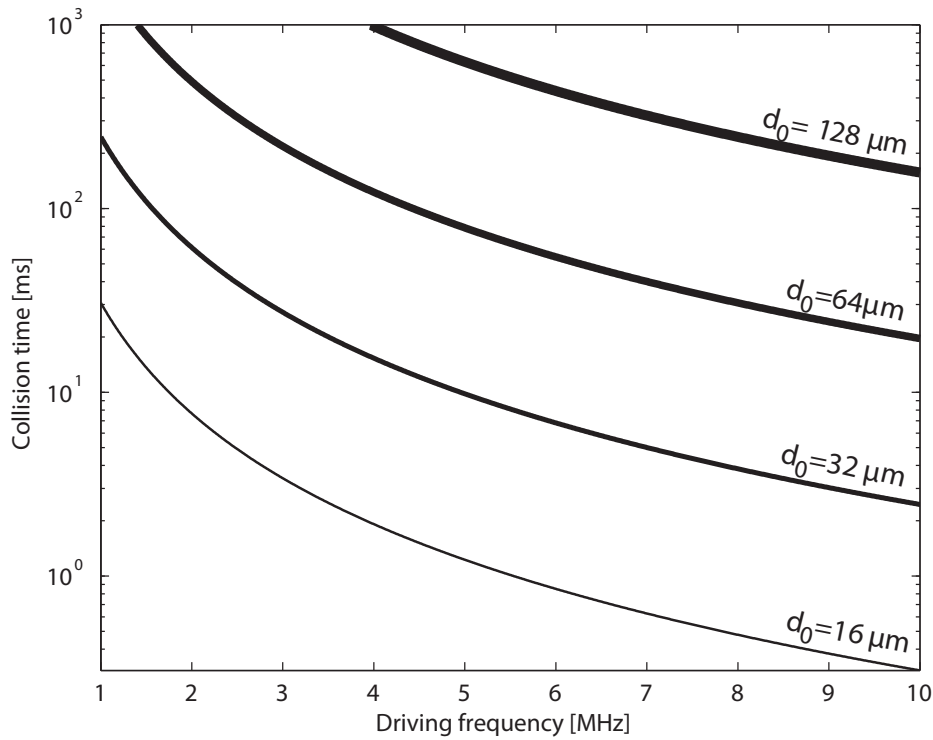


Figure 4.1: Collision times of individual encapsulated microbubbles as a function of driving frequency at given distances d_0 , using $p_a=20$ kPa, $R_0=1.25 \mu\text{m}$, $\kappa=5 \times 10^{-6} \text{ m}^2 \text{ N}^{-1}$ and $\rho=998 \text{ kg m}^{-3}$.

high-speed camera footage of microbubble clustering phenomena is shown and the therapeutic consequences of these findings is discussed.

4.2 Theory

A brief overview of theory on radiation forces and ultrasound contrast agent has been given in [109]. Bubble translation in the direction of the sound field is caused by a primary radiation force resulting from a pressure gradient across the bubble surface. The translation is maximal during the contraction phase. The velocity v of a bubble in a steady fluid subjected to an ultrasound field can be calculated using [25]:

$$F_r + F_d - \frac{d(mv)}{dt} \approx 0, \quad (4.1)$$

where F_r is the primary radiation force, F_d is the drag force, $m = \frac{2}{3}\pi\rho R_0^3$ is the added mass of the translating bubble, equivalent to half the mass of the displaced surrounding fluid, in which R_0 is the equilibrium bubble radius and ρ is the density of the surrounding fluid. Averaging over one acoustic cycle, the primary radiation

force is given by [21, 25, 134]:

$$F_r = \frac{p_a^2 R_0}{\rho c f} \frac{\delta \left(\frac{f_0}{f} \right)}{\left[\left(\frac{f_0}{f} \right)^2 - 1 \right]^2 + \left[\delta \frac{f_0}{f} \right]^2}, \quad (4.2)$$

where c is the speed of sound, p_a is the peak rarefactional acoustic pressure, δ is the dimensionless total damping coefficient [84], f is the driving frequency, and f_0 is the bubble resonance frequency [84]. The drag force is given by [84, 134]:

$$F_d = -\frac{\pi \eta}{4} C_d \text{Re} R_0 v(t), \quad (4.3)$$

where η is the shear (dynamic) viscosity of the fluid, $\text{Re} = \frac{2\rho R_0}{\eta} |v(t)|$ is the Reynolds number, and

$$C_d = \frac{24}{\text{Re}} (1 + 0.15 \text{Re}^{0.687}) \quad (4.4)$$

is the drag coefficient of a contaminated system [31], such as a contrast agent.

Combining Eqns. 4.1 – 4.3 and integrating over dt gives the following expression for the average velocity of a bubble:

$$v = \frac{4p_a^2}{\rho c f \eta C_d \text{Re}} \frac{\delta \left(\frac{f_0}{f} \right)}{\left[\left(\frac{f_0}{f} \right)^2 - 1 \right]^2 + \left[\delta \left(\frac{f_0}{f} \right) \right]^2} \left[1 - e^{\left(-\frac{3\eta C_d \text{Re}}{8\rho R_0^2} t \right)} \right]. \quad (4.5)$$

Secondary radiation forces, resulting from oscillating bubbles under sonication, may cause the mutual attraction and subsequent coalescence of contrast microbubbles. Two bubbles that oscillate in phase approach each other, whereas two bubbles that oscillate out of phase recede from each other [76, 111]. At low acoustic amplitudes, the phase angle difference ϕ between excursion of the oscillating bubble and the incident sound field is given by [21, 76, 111]:

$$\phi = \pi + \arctan \left(\frac{\delta \left(\frac{f}{f_0} \right)}{1 - \left(\frac{f}{f_0} \right)^2} \right). \quad (4.6)$$

The presence of an encapsulating shell increases the damping coefficient by a term δ_s [58]

$$\delta_s = \frac{S_f}{2\pi m f_0}, \quad (4.7)$$

and increases the squared resonance frequency f_0^2 by a term f_s^2 [58]

$$f_s^2 = \frac{\chi}{2\pi R_0^3 \rho}, \quad (4.8)$$

where S_f is the shell friction [58] and χ is the shell stiffness parameter [58, 111]

$$\chi = \frac{E\epsilon}{1-\nu}, \quad (4.9)$$

where E is Young's modulus, ϵ is the shell thickness, and ν is Poisson's ratio.

The mean approach velocity v of two identical bubbles is given by [25]:

$$v = \frac{dd}{dt} = -\frac{(2\pi f p_a)^2}{27\eta} \rho \kappa^2 \frac{R_0^5}{d^2}, \quad (4.10)$$

where d is the distance between the centres of the two bubbles and κ is the compressibility of the bubble. Integrating from the initial distance between the bubbles d_0 to 0 yields the collision time (Eqn. 4.11) shown in Fig. 4.1.

$$t_c = -\int_{d_0}^0 \frac{27\eta}{(2\pi f p_a)^2 \rho \kappa^2 R_0^5} d^2 dd = \frac{9\eta}{(2\pi f p_a)^2 \rho \kappa^2 R_0^5} \frac{d_0^3}{3}, \quad (4.11)$$

In a standing wave field, bubbles with resonance frequencies higher than the transmitted sound field aggregate at the pressure antinodes, whereas bubbles with resonance frequencies lower than the transmitted sound field aggregate at the pressure nodes [76]. Hence, the ultimate distance d_∞ between clusters must be a quarter of the wavelength, *i.e.*,

$$d_\infty = \frac{\lambda}{4} = \frac{c}{4f}. \quad (4.12)$$

Both processes of bubble clusters aggregating and the movement of clusters in the direction of the sound field can be described by a simplified version of Eqn. 4.5.

$$v = \frac{dh}{dt} \approx \frac{p_a^2}{6\rho c f \eta} \frac{\delta\left(\frac{f_c}{f}\right)}{\left[\left(\frac{f_c}{f}\right)^2 - 1\right]^2 + \left[\delta\left(\frac{f_c}{f}\right)\right]^2}, \quad (4.13)$$

where h is the distance travelled by the cluster and f_c is the cluster resonance frequency, for which $f_c < f_0$ must hold, since the bubble cluster radius $R_c > R_0$. For the bubble cluster compressibility κ_c , $\kappa \leq \kappa_c < \kappa_f$ must hold, in which κ_f is the compressibility of a free (unencapsulated) gas bubble.

Bubble coalescence is the fusion of two or more bubbles. As adjacent bubbles

collide or expand, the pressure in the film between them increases, resulting in a deformation (flattening) of the bubble surfaces. The continuing bubble expansion causes drainage of the interposed film. This thinning continues until a critical thickness around $0.1\ \mu\text{m}$ is reached, at which the Van der Waals attractive forces result in film rupture and bubble coalescence [32]. Film drainage is generally much faster for free (unencapsulated) bubbles than for encapsulated bubbles, as a result of the flow pattern in the draining film [108].

The coalescence mechanism of lipid-encapsulated microbubbles was investigated, based on high-speed optical observations of sonicated ultrasound contrast agent microbubbles [108]. It was found that, when sonicated at high acoustic amplitudes, lipid-encapsulated microbubbles expose free surfaces during the expansion phase, speeding up the coalescence process dramatically. Hence, for the formation of bubble clouds or microfoams, the use of low acoustic amplitudes is desirable.

4.3 Materials and methods

A schematic overview of the experimental setup for simultaneous optical observation during sonication is shown in Fig. 4.2.

A polycarbonate container was built with internal dimensions of $24 \times 18 \times 15\ (\text{cm})^3$. To give access to a microscope objective lens and reduce optic aberrations, a 11-mm diameter hole was drilled in the base, covered with a 2-mm thick test slide (Jencons (Scientific) Ltd., Leighton Buzzard, Bedfordshire, UK). The container was filled with 2.6L tap water. The container was locked in place on an $x - y$ translation stage of a DM IRM inverted microscope (Leica Microsystems GmbH, Wetzlar, Germany) with two objective lenses: a 506075 C-Plan $10\times/0.22$ NA objective lens (Leica Microsystems GmbH), and a 506236 N-Plan $50\times/0.50$ NA (Leica Microsystems GmbH) objective lens. A Mille Luce™ Fibre Optic Illuminator Model M1000 (StockerYale, Inc., Salem, NH) was connected to an optic fibre with a 7-mm diameter leading into the water of the container. It was placed in line with the objective lens, as shown in Fig. 4.3.

The charge coupled device (CCD) of a FASTCAM MC-1 high-speed camera (Photron (Europe) Limited, West Wycombe, Bucks, United Kingdom) was mounted to the C-Mount of the microscope and connected to its processing unit, which was capable of recording images up to 10,000 frames per second. The camera was controlled by a laptop computer.

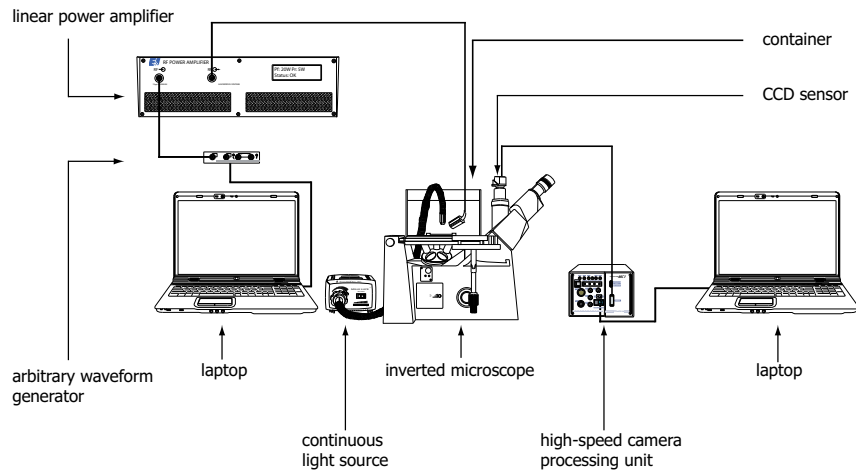


Figure 4.2: Schematic overview of the experimental setup.

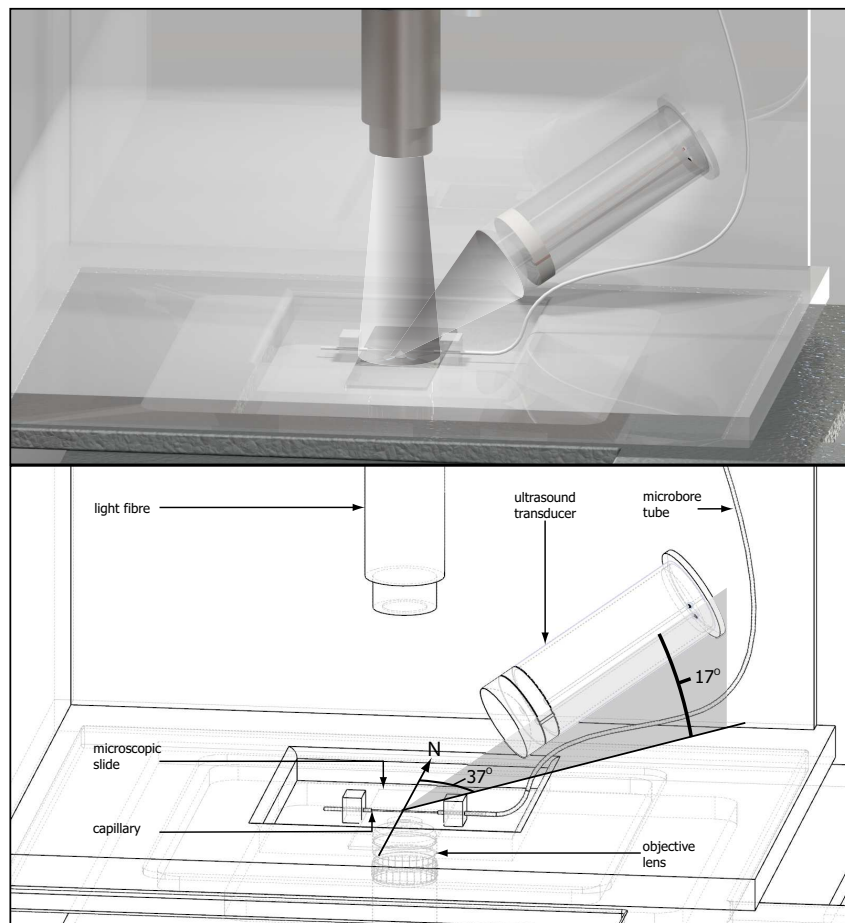


Figure 4.3: Close-up of the sonication tank with coinciding sound, light beam, and objective focus (top) and definitions of the azimuth and elevation of the transducer relative to the North of the container (bottom).

4.3.1 Ultrasound

A laptop computer triggered a DATAMAN-530 arbitrary waveform generator (Dataman Programmers Ltd., Maiden Newton, Dorset, UK), which was connected to a 2100L, 50-dB RF power amplifier (Electronics & Innovation Ltd., Rochester, NY). The power amplifier was connected to a single element transducer containing a Pz37 Piezoelectric ceramic (Ferroperm Piezoceramic A/S, Kvistgård, Denmark) with a centre frequency of 2.2 MHz. The design of the transducer is shown in Fig. 3.2. Transmitted signals were continuous waves with frequencies in the range 1–10 MHz. The peak-negative acoustic pressures were determined using a PVDF needle hydrophone system with a 0.2-mm active element (Precision Acoustics Ltd., Dorchester, Dorset, UK) connected to a TDS 420A digitising oscilloscope (Tektronix, Inc., Beaverton, OR).

The ultrasound transducer was positioned in the container using a clamp stand, at a focal distance of 38 mm from the region of interest to be studied. The azimuth of the length axis of the transducer to the relative North of the container was 37° and the elevation of the length axis of the transducer relative to the base of the container was 17° , as shown in Fig. 4.3.

4.3.2 Ultrasound contrast agent

Definity[®] (Lantheus Medical Imaging, North Billerica, MA) consists of C_3F_8 gas microbubbles with mean diameter between 1.1 and 3.3 μm , encapsulated by a lipid/surfactant shell. Its resonance frequency has been measured to be 2.7 MHz [61]. The 1.5-ml vials used in these experiments were stored at 9°C . Each vial was shaken for 15 s using a Vialmix[®] device (Lantheus Medical Imaging, North Billerica, MA). Before introducing the ultrasound contrast agent, it was further diluted using a 0.9% saline solution.

The diluted ultrasound contrast agent was inserted using a syringe into a micro-bore tube with a 0.51-mm inner diameter. The tube led to a CUPROPHAN[®] RC55 cellulose capillary (Membrana GmbH, Wuppertal, Germany) with a 200- μm inner diameter and 8- μm wall thickness. The middle of the capillary coincided with the optical focus of the objective lens and with the acoustic focus of the ultrasound transducer, as shown in Fig. 4.3. The typical field of view using the 10 \times objective lens was $500 \times 500 (\mu\text{m})^2$, whereas the diameter of the acoustic focus was greater than 5 mm. Hence, the whole field of view could be considered in acoustic focus. The capillary was positioned 2 mm above base of the container. The flow speed of the ultrasound contrast agent through the capillary was manually controlled.

In total, 48 experiments were performed. Bubble and cluster sizes were measured and tracked using Image-Pro Plus (Media Cybernetics, Inc., Bethesda, MD). Further analysis was done using MATLAB® (The Mathworks™, Natick, MA).

4.4 Results and discussion

At the high concentration used, clustering started instantaneously after the ultrasound source activated. Fig. 4.4 illustrates the speed of cluster formation of DEFINITY® ultrasound contrast agent that had been further diluted to 1:20 v/v.

With distances between microbubbles of only few micrometers, collision times from Eqn. 4.11 should be within a second, as shown in Fig. 4.1. Also from Eqn. 4.11 and Fig. 4.1 it is explained why cluster formation must be faster at higher frequencies, if the other acoustic parameters and the concentration are not changed, or, after a fixed duration, larger clusters must have formed using higher frequencies, since bubbles can approach from larger d_0 at higher f . These deductions are confirmed by the following experimental observations. In Fig. 4.4, after 233 ms two clusters have been formed of approximately 15 μm diameter each. These started to approach in the subsequent frames. Overall, newly-formed clusters collided to form larger clusters. This is illustrated in Figs. 4.5 & 4.6.

Each branch represents a cluster. The branches coming together represent the collision and coalescence of clusters into larger clusters. The velocities of clusters are on the order of tens of micrometers per second. Although increasing the acoustic pressure would increase the cluster velocities dramatically, as evident from Eqn. 4.13, they would also lead to microbubble disruption [111]. At the frame rates used phenomena associated with microbubble disruption were not observed.

The larger a cluster grows, the lower its resonance frequency becomes. Hence, the velocity of a cluster in the direction of the sound field, defined by Eqn. 4.13, should decrease in time. If two identical clusters with resonance frequency f_0 merge, the resulting resonance frequency is $f'_c \approx \left(2^{-\frac{1}{3}}\right) f_0 = 0.79 f_0$ [110]. Assuming that the compressibility and damping coefficient do not substantially change, a similar decrease in cluster velocity is expected. However, the decrease in slope magnitude of the main branch in Fig. 4.5 is negligible. This might be explained if the resulting cluster is much stiffer than the original clusters, increasing the damping coefficient.

Also, 7 MHz must be further off the cluster resonance frequency than 2 MHz. Hence, the magnitudes of the slopes in Fig. 4.6 are lower than those in Fig. 4.5. Secondary radiation forces of clusters onto each other do not explain the cluster

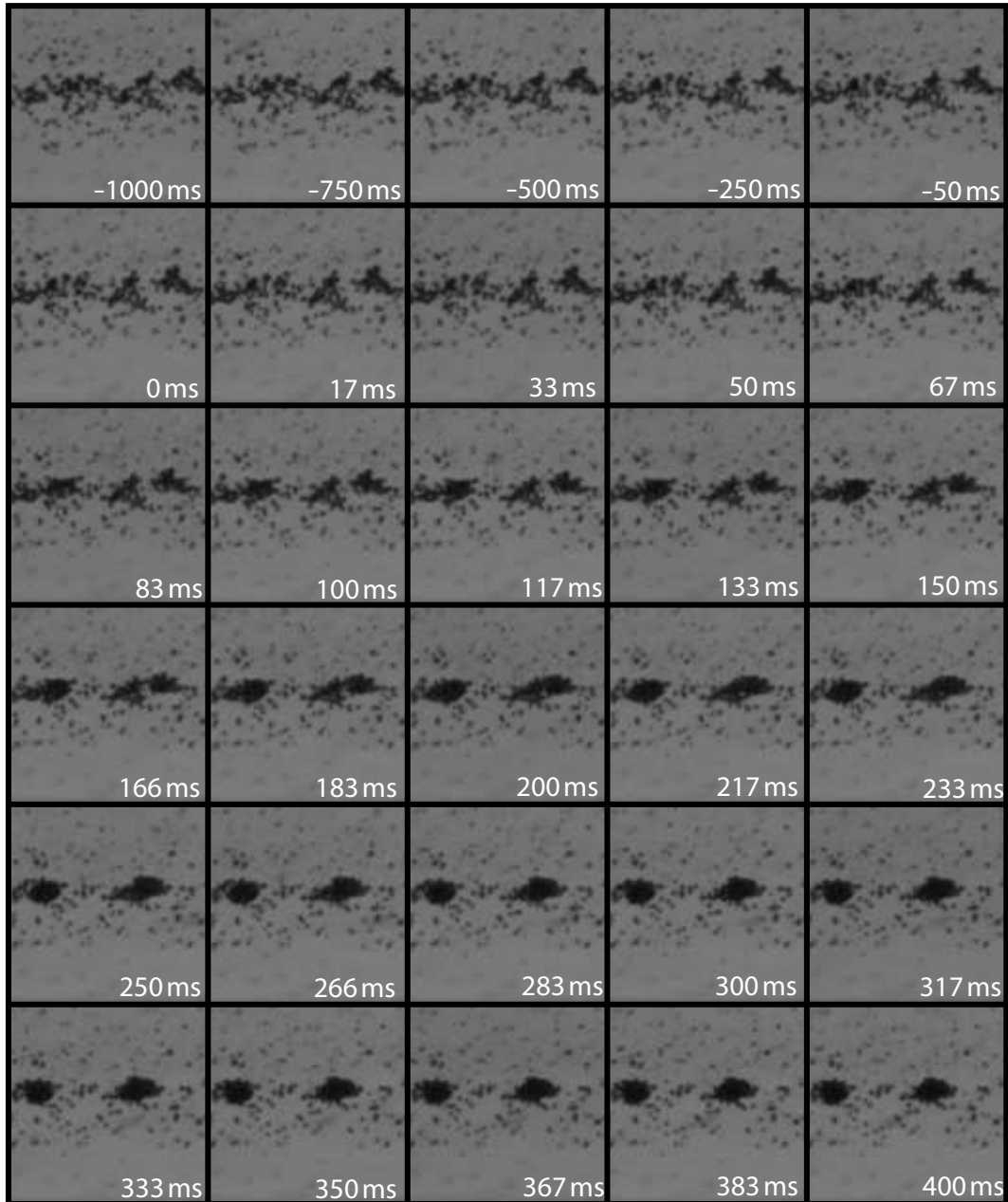


Figure 4.4: Microfoam formation during continuous sonication at 2 MHz and 20-kPa peak-negative acoustic pressure. Each frame corresponds to a $120 \times 120 (\mu\text{m})^2$ area. Time $t = 0$ was defined by the start of the sonication.

colliding times observed. Even if the compressibility of the clusters would be equal to that of a single ultrasound contrast agent microbubble, under the acoustic conditions used the collision times from Eqn.4.11 would be just milliseconds. Hence, the bubble clusters cannot be regarded as identical monopoles in this setting. A close-up of two colliding clusters with 22- μm diameters forming a 25- μm cluster is shown in Fig.4.7. The total time spanning this process is slightly less than 1.8 s.

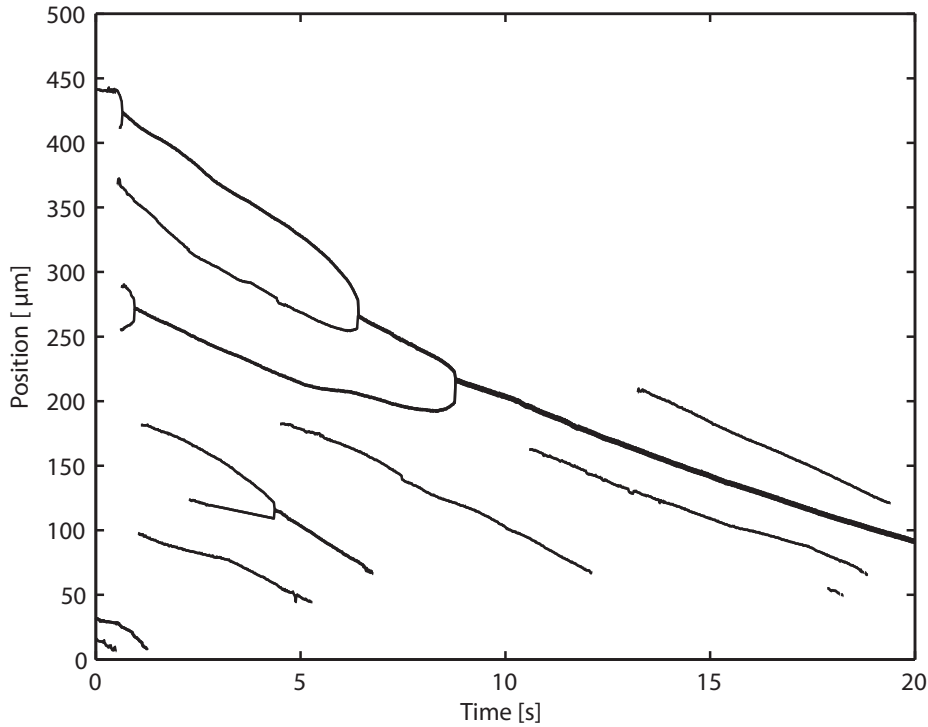


Figure 4.5: Cluster positions as a function of time, during continuous sonication at 2 MHz and 20-kPa peak-negative acoustic pressure. Position in the capillary is defined from East ($0 \mu\text{m}$) to West ($500 \mu\text{m}$). Bold lines indicate merged clusters. The beginning (left) of a line indicated the formation of a cluster of diameter $>6.8 \mu\text{m}$. The end (right) of a line indicates the disintegration or contraction of a cluster to a diameter $<6.8 \mu\text{m}$.

The clusters were initially formed in the middle of the capillary. These clusters were located at distances $d_0 < \frac{1}{4}\lambda$, as demonstrated in Fig. 4.8. However, following further cluster coalescence during 17.55 s of sonication, the final distance between the larger clusters corresponded to $\frac{1}{4}\lambda = 54 \mu\text{m}$. These had been pushed towards the lower capillary wall, owing to primary radiation forces.

The clusters velocities towards the capillary wall were between $5 \mu\text{m s}^{-1}$ at 7 MHz and 22 kPa peak-negative pressure and $15 \mu\text{m s}^{-1}$ at 2 MHz and 20 kPa peak-negative pressure sonication. These are of the same order as the left hand side term in Eqn. 4.13. The magnitudes of the slopes in Fig. 4.6 did not change close to the capillary wall. Hence, in this experimental setup, any effect of the capillary wall on cluster translation was neglected.

At these bulk concentrations, clusters were formed within seconds with diameters $25 \pm 2 \mu\text{m}$. Taking into account the diameters and assuming a spherical shape, it can be estimated that the clusters contain 2,000 microbubbles each.

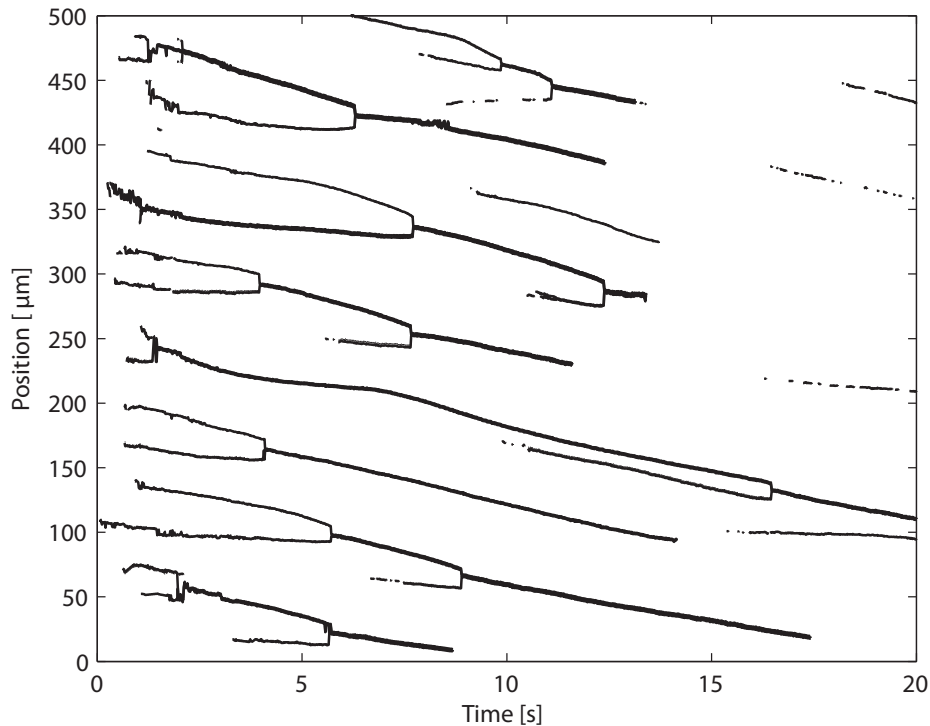


Figure 4.6: Cluster positions as a function of time, during continuous sonication at 7 MHz and 22 kPa peak-negative acoustic pressure. Position in the capillary is defined from East ($0\ \mu\text{m}$) to West ($500\ \mu\text{m}$). Bold lines indicate merged clusters. The beginning (left) of a line indicated the formation of a cluster of diameter $>6.8\ \mu\text{m}$. The end (right) of a line indicates the disintegration or contraction of a cluster to a diameter $<6.8\ \mu\text{m}$.

The clusters interact, owing to primary and secondary Bjerknes forces, creating morphing microfoams. Figure 4.9 shows four interacting clusters in steady liquid. Primary Bjerknes forces push the clusters in the direction of the sound field at an average speed of $4\ \text{mm s}^{-1}$. The shear of the capillary wall caused a rotation of the interacting clusters.

Figure 4.10 shows at least eight interacting clusters. Again, a rotation motion can be observed. Also, individual ultrasound contrast agent microbubbles can be seen to hop from cluster to cluster. This microscopic scale behaviour can be attributed to very subtle changes in the acoustic field, causing ever-changing local nodes and antinodes.

With cluster diameters less than $30\ \mu\text{m}$, buoyancy effects may be neglected at these timescales as well.

In summary, the following stages of microfoam formation, illustrated in Fig. 4.11 were observed. The initial situation was a dense, random

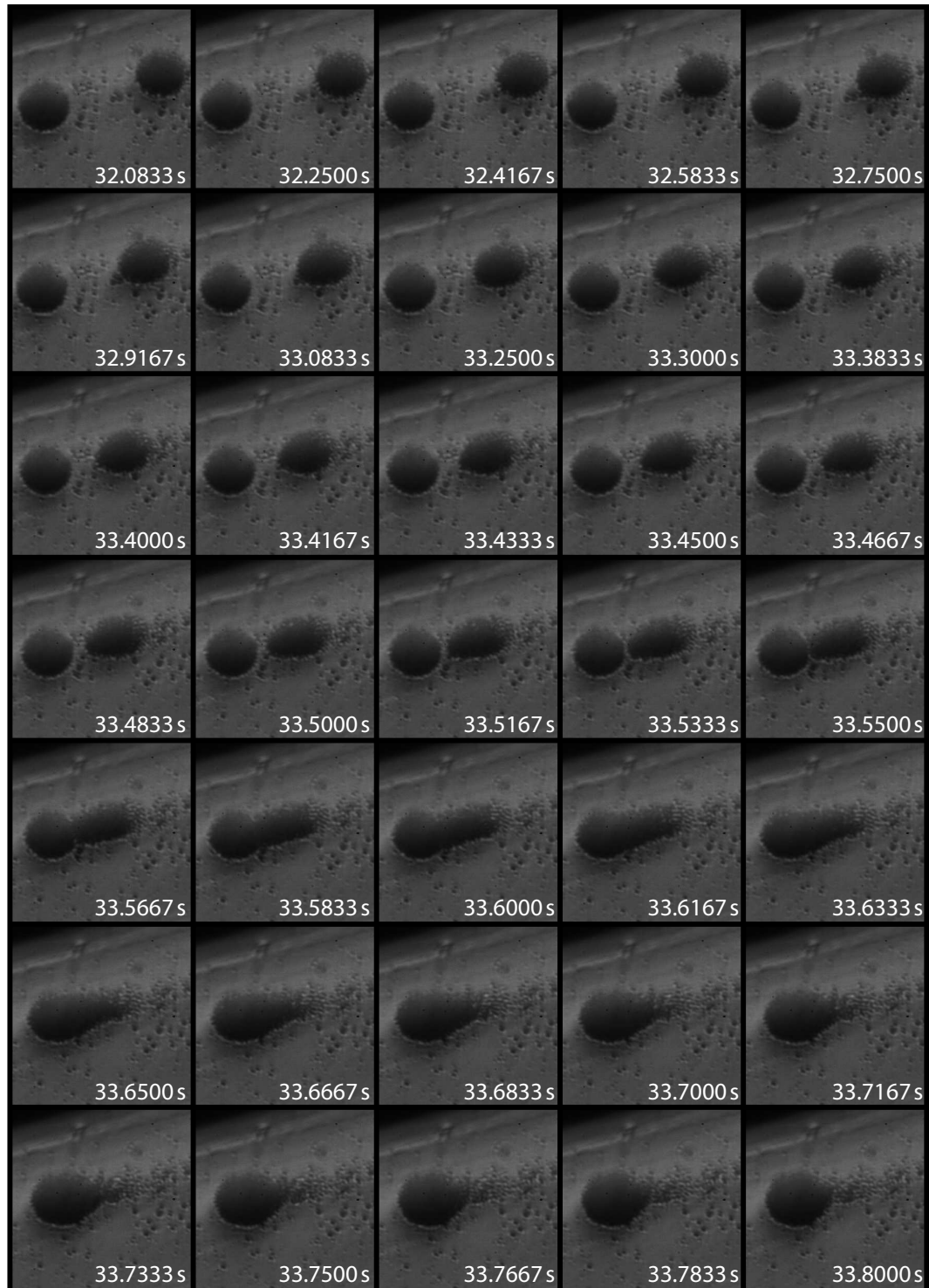


Figure 4.7: Two clusters, with 22- μm diameters and an initial distance of 55- μm , colliding and merging during continuous sonication at a 2-MHz driving frequency and a 20-kPa peak-negative pressure. The frame size corresponds to $81 \times 81 (\mu\text{m})^2$. Times are relative to the start of the sonication ($t = 0$).

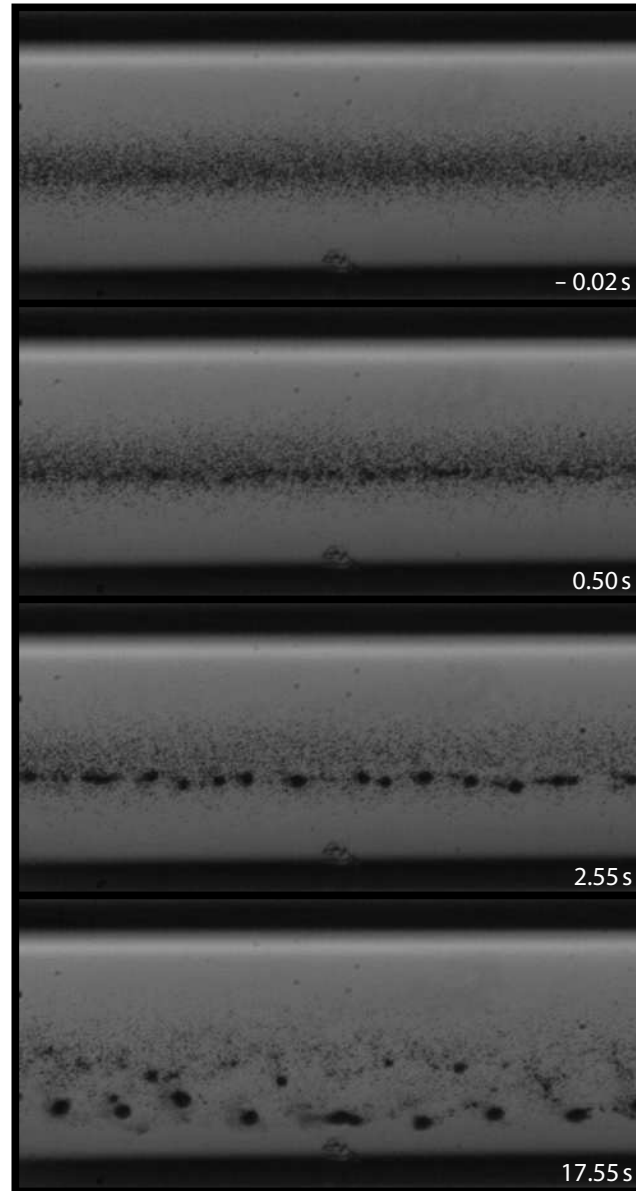


Figure 4.8: Clusters forming during sonication at 7 MHz and 22 kPa peak-negative pressure. The frame size corresponds to $560 \times 264 \text{ } (\mu\text{m})^2$. Time $t = 0$ was defined by the start of the sonication.

bubble distribution before ultrasound arrival. After sonication started, contrast microbubbles collided, owing to secondary radiation forces. Subsequently, these clusters merged within the space of a quarter of the wavelength, owing to primary radiation forces. The resulting microfoams translated in the direction of the ultrasound field, owing to primary radiation forces.

Small deviations in microbubble sizes or shell properties lead to deviations in individual bubbles' resonance frequencies, as expressed in Eqn. 4.8. These in turn cause oscillation phase differences, as expressed in Eqn. 4.6, big enough to be

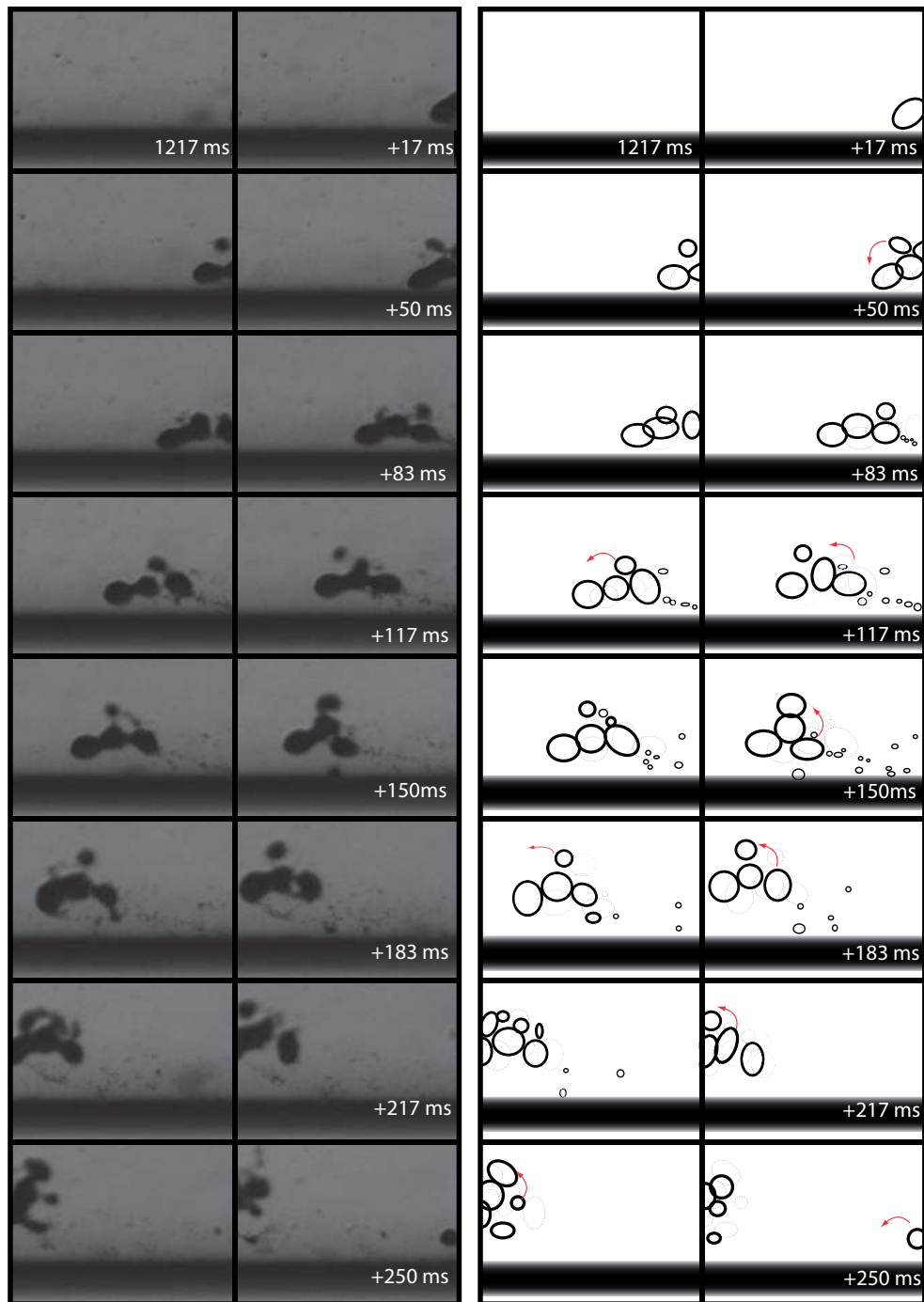


Figure 4.9: Morphing microfoam during sonication at 7 MHz and 86 kPa peak-negative pressure, and a schematic representation of the event. The frame size corresponds to $274 \times 198 (\mu\text{m})^2$. Time $t = 0$ was defined by the start of the sonication.

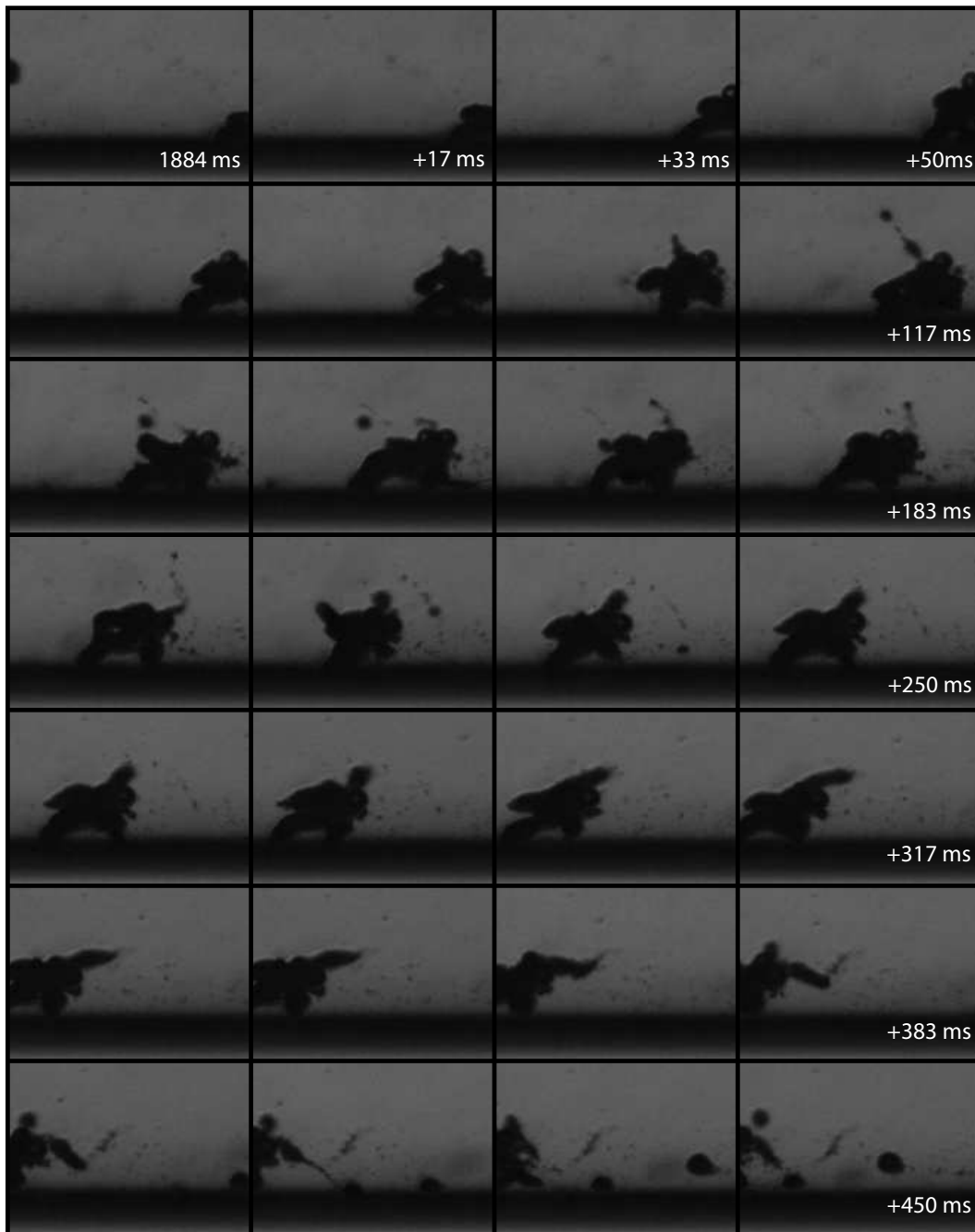


Figure 4.10: Morphing microfoam during sonication at 7 MHz and 86 kPa peak-negative pressure, and a schematic representation of the event. The frame size corresponds to $274 \times 198 (\mu\text{m})^2$. Time $t = 0$ was defined by the start of the sonication.

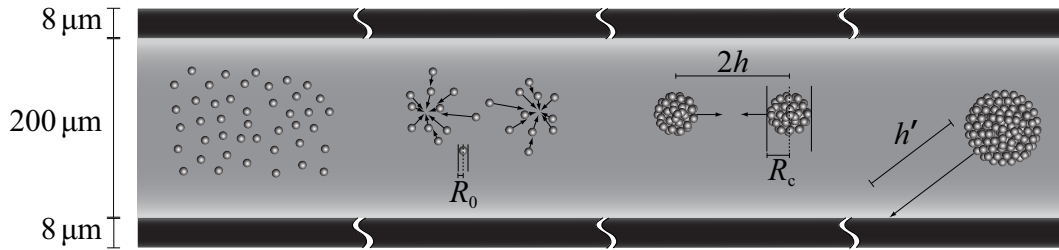


Figure 4.11: Schematic representation of the four stages of microfoam formation in a capillary: (left-right) random bubble distribution before ultrasound arrival, bubbles colliding during sonication, cluster meroence within the space of a quarter of the wavelength, microfoam translation.

observed [109]. Therefore, predicting and manipulating individual microbubbles is technically challenging. It has been demonstrated that as soon as the bubble clusters were formed and as long as they were in the sound field, they behaved as one entity. At the acoustic settings used, it took seconds to force the bubble clusters to positions approximately $\frac{1}{4}\lambda$ apart. It also just took seconds to drive the clusters towards a boundary.

It may assume that vessel blocking can only be successful if a microfoam is created with a diameter equal to or greater than the vessel diameter d_v . From this study it follows that in order to create such a foam, $\frac{1}{4}\lambda > d_v$, or, $f < \frac{c}{4d_v}$.

For therapeutic purposes, it would be of great interest to induce microjetting on entire clusters towards a vessel wall, presumably causing sonoporation or sonolysis. Although ultrasound-induced microjetting has been observed with ultrasound contrast agents, its occurrence in *in vivo* situations is hard to control [112, 114]. Predictable sonic manipulation would be better feasible if the microbubbles would be forced to cluster to known size and position first.

4.5 Conclusions

The following stages of microfoam formation within a densely populated concentration of microbubbles was observed. After the sonication started, contrast microbubbles collided, forming small clusters, owing to secondary radiation forces. These clusters coalesced within the space of a quarter of the ultrasonic wavelength, owing to primary radiation forces. The resulting microfoams translated in the direction of the ultrasound field, hitting the capillary wall, also owing to primary radiation forces.

It has been demonstrated that as soon as the bubble clusters were formed and

as long as they were in the sound field, they behaved as one entity. At the acoustic settings used, it took seconds to force the bubble clusters to positions approximately a quarter wavelength apart. It also just took seconds to drive the clusters towards the capillary wall.

Subjecting ultrasound contrast agent microbubbles to a continuous low-amplitude signal makes them cluster to known positions and known microfoam sizes, allowing for straightforward sonic manipulation.

5

Laser-nucleated ultrasonic acoustic cavitation

Abstract

Acoustic cavitation can occur during therapeutic applications of high-amplitude focussed ultrasound. Studying acoustic cavitation has been challenging, because the location of nucleation is unpredictable. It is hypothesised that acoustic cavitation can be forced to occur at a specific location, using a laser to nucleate a microcavity in a pre-established ultrasound field. In this chapter a scientific instrument that is dedicated to this outcome, combining a focussed ultrasound transducer with a pulsed laser is described. High-speed photographic observations of laser-induced cavitation and laser-nucleated acoustic cavitation from laser pulses of energy above and below the optical breakdown threshold respectively, at frame rates of 0.5

Based on: Gerold B, Kotopoulis S, McDougall C, M^cGloin D, Postema M, Prentice P. Laser-nucleated acoustic cavitation in focussed ultrasound. *Rev Sci Instrum* **2011** accepted.

This work has been supported by EU FP7 Grant 230674 (Nanoporation), DFG Emmy Noether Programme Grant 38355133, and EPSRC Grants EP/G01213X/1 and EP/F037025/1. Bjoern Gerold has been supported supported by an EPSRC DTA award. I am very grateful to EPSRC loan pool, notably to Adrian Walker, for ongoing access to high-speed imaging devices; to Javier Grinfeld, Yoav Medan, Oleg Prus, and Alex Volovick, all from InSightec Ltd., Tirat Carmel, Israel, for ongoing technical support; and Joyce Joy for ultrasound calibration measurements.

million frames per second are presented. Acoustic recordings demonstrated inertial cavitation can be controllably introduced to the ultrasound focus. This technique will contribute to the understanding of cavitation evolution in focussed ultrasound, including its potential use in therapeutic applications.

5.1 Introduction

Cavitation is the formation of cavities, or bubbles, in liquids. Apart from mechanical or hydraulic cavitation, which occur in a rapidly flowing fluid [8], cavities can be generated using high-amplitude acoustic waves, or optically, induced via absorption of a laser pulse focussed into a liquid. Acoustic and optical cavitation both occur above some characteristic threshold intensity of the respective forms of radiation. For acoustic cavitation, the threshold is a function of the peak-negative pressure and frequency of the ultrasound; sometimes referred to as the Blake threshold [148].

Acoustic cavitation is perhaps best known for its role in ultrasonic cleaning, but it is also encountered during the application of focussed ultrasound surgery (FUS). FUS procedures involve high-intensity focussed ultrasound (HIFU) in the MHz range onto target tissue such as a tumour, for ablation via viscous absorption of the mechanical energy. This has the distinct advantage of avoiding any requirement for invasive surgical intervention. Cavitation is currently carefully avoided in clinical FUS procedures, as it may scatter incident ultrasound radiation, which may result in malformed and unpredictable lesions. However, it is under investigation for potential enhancement of therapeutic effects during FUS, including as a mechanism for rapid heat deposition, and for actively promoting drug delivery via tissue disruption [20, 53]. Distinguishing between the types of acoustic cavitation [76], is useful for considering the related effects that may be harnessed for therapeutic applications. Stable (non-inertial) cavitation refers to extended periodic oscillations around some equilibrium radius, which generate acoustic emissions at the driving frequency and its harmonics. Transient (or inertial) cavitation describes unstable growth followed by rapid collapse, driven by the inertia of the host medium. This form of cavitation is associated with high localised energy densities and broadband acoustic emissions [110], and may be monitored by way of a dose-control mechanism for possible enhanced FUS effects.

Current understanding of cavitation in focussed ultrasound is hampered by inherent difficulties in studying the phenomenon, including ultrafast dynamics at typical HIFU frequencies and the small cavitation nuclei, which are a few

micrometers in diameter. Moreover, the exact site of nucleation is difficult to predict, often occurring at an impurity or gaseous inclusion within the field. Addressing some of these issues provided the motivation for the work reported here. In contrast, laser-induced cavitation, where a short laser pulse is focussed into a liquid to form a plasma which rapidly expands to form a cavity [39, 50], is a well-established and understood approach used to study single-cavity dynamics in a range of fluidic environments [96]. The distinct advantage of this technique is the predetermined location of the cavity, defined by the point which the laser pulse is focussed. This allows the incorporation of high-speed cameras imaging at frame rates capable of resolving these cavitation dynamics. In this manner, cavitation-related activity such as the phenomenon of jet formation from collapsing cavities in the vicinity of a boundary [98], causing material erosion and surface cleaning, can be reliably and reproducibly investigated. The uncertainty of the positional and temporal occurrence of acoustic cavitation prevents meaningful implementation of high-speed cameras for studying the development of cavitation activity in ultrasound fields. A number of such studies have been attempted [15, 16], although the large field-of-view and long exposure times the investigators were required to employ limited the impact of the observations on the understanding of the acoustic cavity cloud evolution, particularly over the first few hundred cycles of ultrasound exposure. Laser-induced cavitation studies allow much higher temporally and spatially resolved dynamics, but have limited relevance to acoustic cavitation, as the pulse energy required to induce optical breakdown in the host medium results in cavity dimensions typically above a few $\varnothing 100 \mu\text{m}$, much larger than those typically encountered in MHz ultrasound fields. In this chapter, the development of an instrument that combines conventional approaches to studying acoustic and optical cavitation, and which permits the use of high-speed cameras at MHz frame rates, to observe the evolution of acoustically driven cavitation clouds is reported. Laser-induced cavitation in an ultrasound field has been previously investigated using high-speed photography [71]. To enhance cavitation collapse phenomena, bubble luminescence was studied as a function of seeding phase in a 44.6-kHz field. The current work is quite distinct in terms of employing low-energy nanosecond pulses in a well-characterised, moderate- to high-MI focussed field. Section 5.2 describes in detail the experimental arrangement, and the custom-designed chamber that allows optical access to the focal region of an ultrasound bowl transducer, whilst also allowing the ultrasound itself to propagate unimpeded. Section 5.4 presents sample results for each of the cavitation regimes possible with the instrument, including conventional

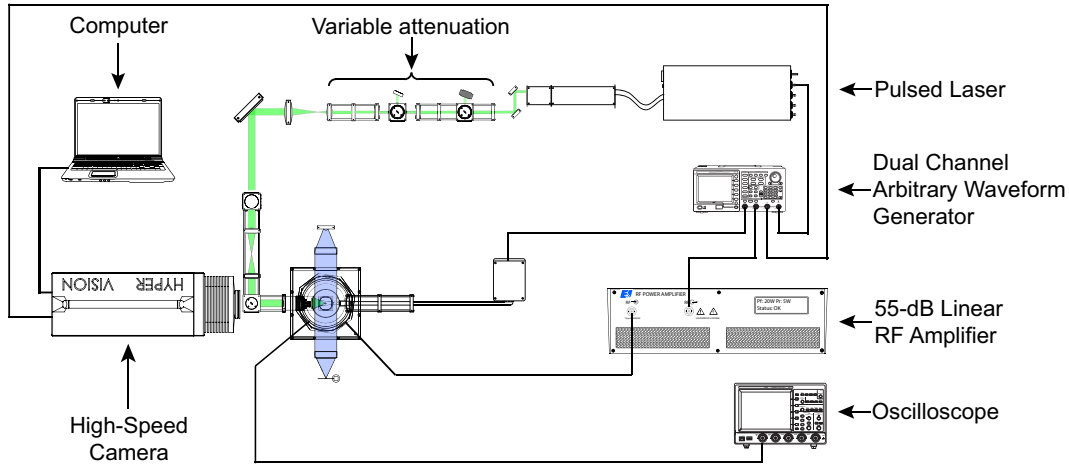


Figure 5.1: Schematic overview of apparatus, including BNC trigger lines and ultrasound electronics.

laser-induced cavitation, laser-induced cavitation in a pre-established ultrasound field, and the new phenomenon of laser-nucleated acoustical cavitation.

5.2 Methodology

In this section the experimental setup developed to observe distinct regimes of hybrid acoustic and optical cavitation is described. Figure 5.1 is a schematic representation of the apparatus. The ultrasound was generated by a focussed bowl transducer and accompanying electronics. The optical system was a standard laser-induced cavitation arrangement. The key feature of the instrument was the sonoptic chamber, shown in Figure 5.2, which permits irradiation of the ultrasound focus with a laser pulse, focussed through a long working distance objective lens, without disrupting the field, other than intentionally with cavitation activity. The entire device was constructed on an RS2000 active self-levelling and vibration damping optical table (Newport, Didcot, Oxfordshire, UK).

5.2.1 Acoustics

Focussed ultrasound

The ultrasound source was a single-element, 100-mm diameter, PZT, spherically focussed ultrasound transducer with a geometric focus of 80 mm (GE Healthcare, Waukesha, WI). The transducer had an efficiency of 30% at its impedance-matched resonance frequency of 1.47 MHz. The device was driven by an AFG3102 (Tektronix, Everett, WA) arbitrary function generator. The signal was passed via a

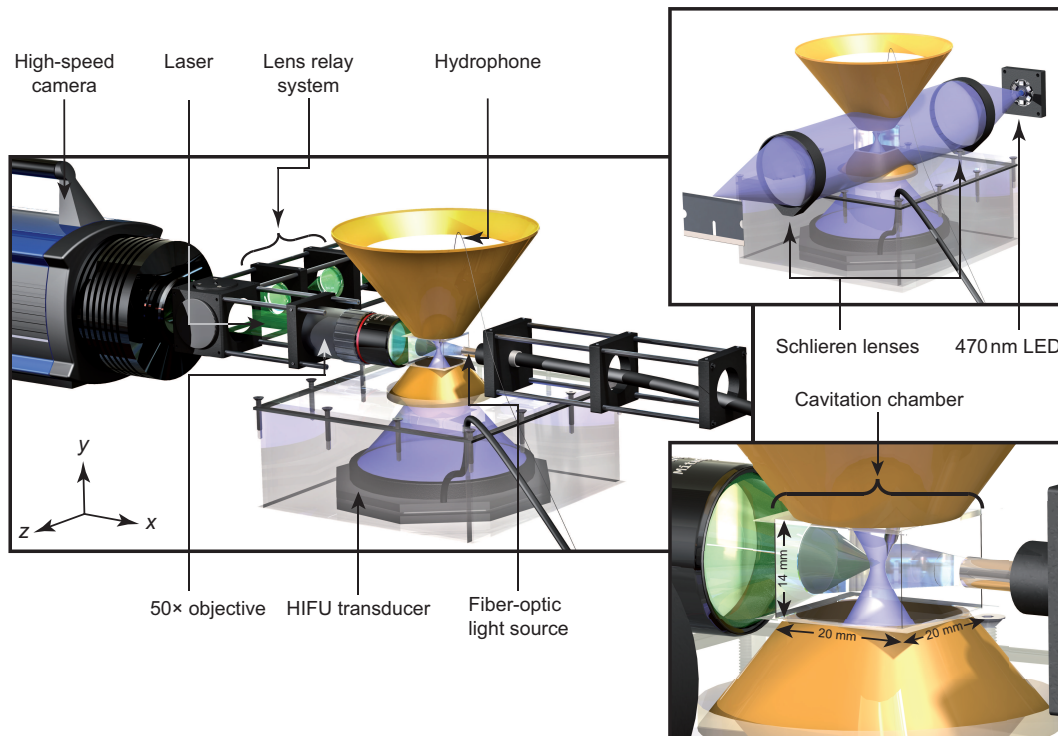


Figure 5.2: Representation of the custom-made sonoptic chamber, constructed according to the dimensions of the focussed ultrasound field. The Shimadzu HPV-1 high-speed camera is depicted. Inset top right is the Schlieren imaging arrangement for alignment of the ultrasonic and optical foci. Inset bottom right is a close up of the cavitation chamber which contains the ultrasound (blue) and laser (green) foci.

20-dB attenuator to a 3100LA, 55-dB RF amplifier (Electronics & Innovation Ltd., Rochester, NY). The ultrasound field generated was characterised, *cf.* Figure 5.3, in a custom-made 3-dimensional scanning tank, using a 200- μm PVDF needle hydrophone (Onda, Sunnyvale, CA). These free-field profiles were subsequently used to validate the field when the transducer was located within the sonoptic chamber.

The custom-made sonoptic chamber shown in Figure 5.2 was designed and constructed specifically for this transducer so that the ultrasound beam produced could propagate through the focus without scatter or reflection. The transducer housing was constructed out of 6-mm thick polycarbonate sheets and had internal dimensions of $188 \times 188 \times 89 \text{ (mm)}^3$. Above the transducer housing, two polyvinyl chloride (PVC) funnels connected via their tapered ends to a $20 \times 20 \times 14 \text{ (mm)}^3$ glass cavitation chamber, constructed from standard 155- μm thick microscope coverslips (Scientific Laboratory Supplies Ltd., Hessel, East Riding of Yorkshire, UK) and glued using Rapid ARALDITE™ epoxy (Bostik S.A., Paris la Défense,

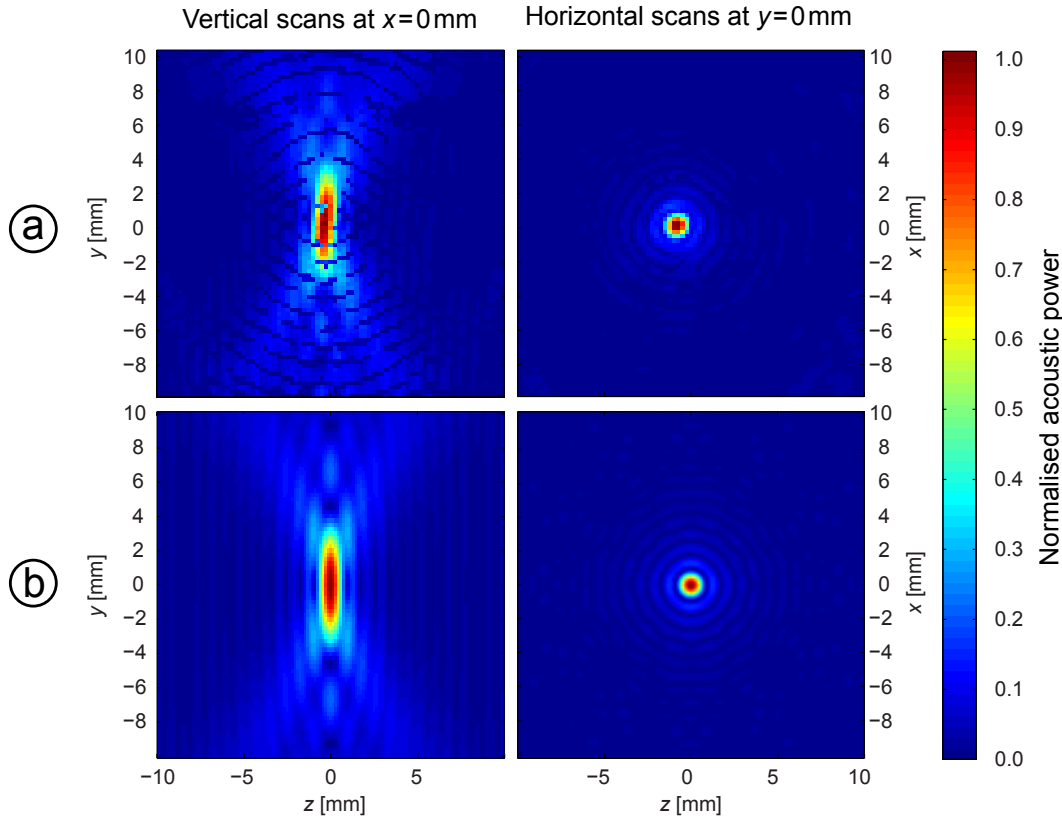


Figure 5.3: (a) Scanned axial and transverse pressure fields of the focussed bowl transducer used as the ultrasound source throughout the experiments, recorded in an ultrasound scanning tank. (b) Simulation of field based on the dimensions of the transducer.

France). The position of the cavitation chamber over the transducer as such that the centre aligned with the acoustic focus. The second inverted funnel was positioned above the cavitation chamber to allow unhindered acoustic propagation into the far field. The sonoptic chamber as mounted on an M-652 x - y - z micro-translation stage (Newport) for alignment of the ultrasonic focus to the optical focus. To verify the sonoptic chamber did not impede or scatter the acoustic beam at any point, pressure maps were taken in a plane across the focal region within the cavitation chamber shown in Figure 5.4, using a fibre-optic hydrophone (Precision Acoustics Ltd., Dorset, Dorchester, UK) [88], with a tapered tip of sensitivity 175 mV MPa^{-1} , at 1.5 MHz.

Acoustic detection

A custom-made 200- μm PZT hydrophone connected via an amplifier ($42\times$ at 1 MHz) to an MSO7104A oscilloscope (Agilent Technologies UK Limited, Wokingham, Berkshire, UK) was situated within the cavitation chamber, outside

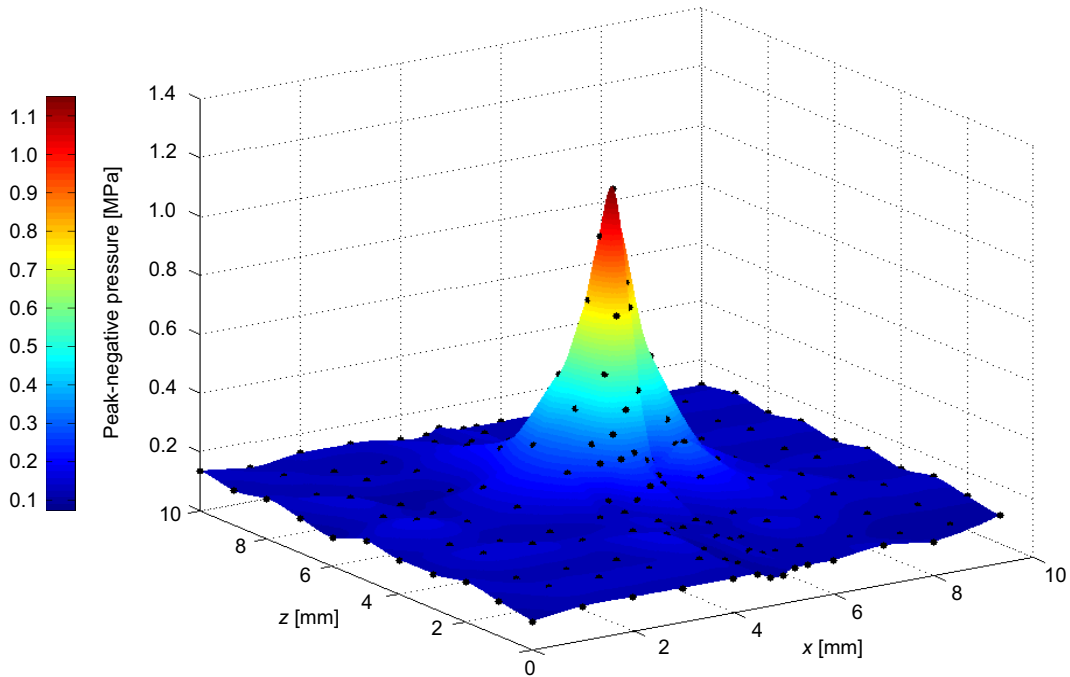


Figure 5.4: Cubic interpolation of the 2-dimensional scans, with sample pressure data measured in the acoustic focus within the sonoptic chamber (black dots), demonstrating ultrasound propagation.

the acoustic focus as depicted in Figure 5.5Ⓐ. Figure 5.5Ⓑ shows spectra generated at ① MI = 0.6 and ② MI = 5.5, from the hydrophone in this position, without laser-pulse generation. At low MI, the spectral content is concentrated around the fundamental at 1.47 MHz. At high MI the additional harmonics indicating the presence of stable cavitation, as may be anticipated in this acoustic regime. For the acoustic detection results presented, a notch filter was used to suppress the fundamental signal from the primary field. In all experiments degassed tap water was used. This is defined as water with a oxygen content of $< 4 \text{ mg L}^{-1}$ [122]. Degassing was achieved using liquid heating [37]. The gas content was measured before and after the experiments using a DO 110 dissolved oxygen meter (Oakton, Vernon Hill, IL), and determined to be less than 4 mg L^{-1} for all reported experiments.

5.2.2 Optics

Laser source

The laser source was a Nano S 130-10 Q-sitched Nd:YAG pulsed laser (Litron Lasers, Rugby, Warwickshire, UK) emitting up to 70 mJ at 532 nm with a pulse

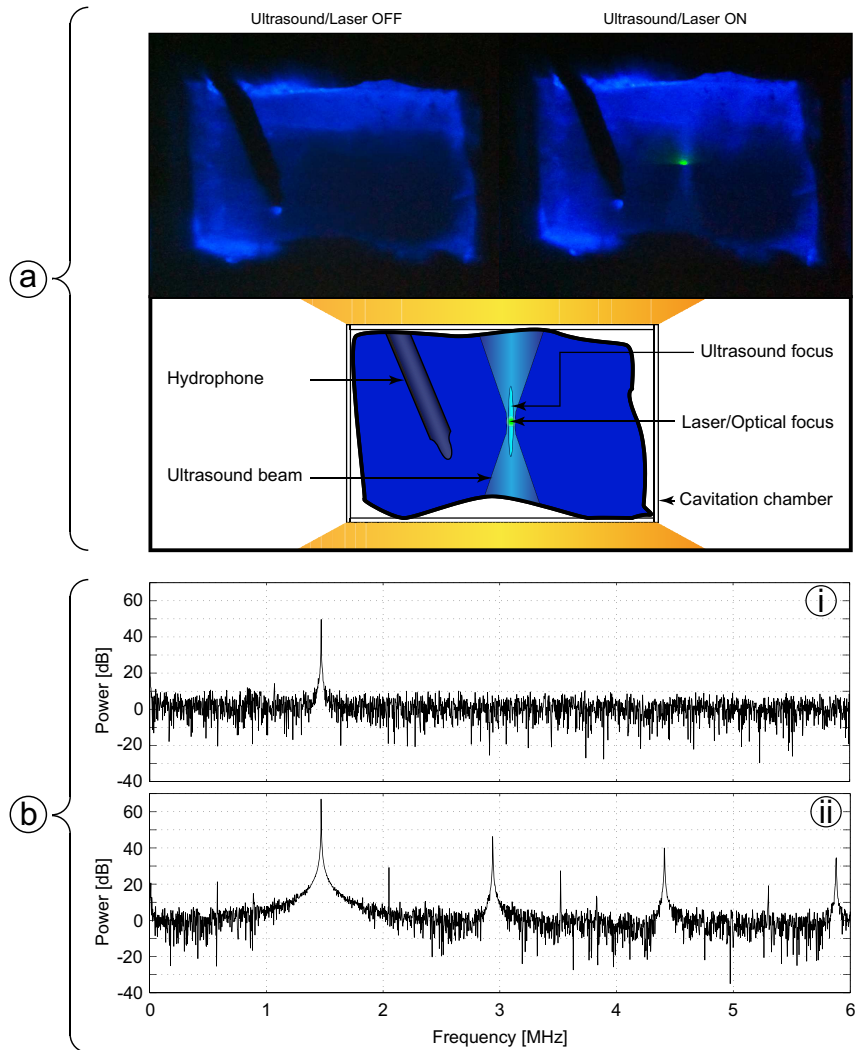


Figure 5.5: ④ Schlieren image of cavitation chamber, used to align the laser focus (green spot) to that of the ultrasound (lighter blue region). The omnidirectional needle hydrophone used to record acoustical emissions during cavitation activity is also visible. ⑤ Fourier spectra of sound field where ① MI = 0.6 and ② MI = 5.5.

duration of 6–8 ns and repetition rate of up to 10 Hz. To accurately control the pulse energy, 650–1050 nm, \varnothing 10 mm, GL10-B, anti-reflection coated, polarising cubes (Thorlabs, LTD., Ely, Cambridgeshire, UK) and 532 nm, \varnothing 12.7-mm $\frac{\lambda}{2}$ -wave plates (Thorlabs) were used. The first cube and wave-plate pair provided coarse attenuation and the second was used for fine tuning. The beam was expanded to slightly overfill the back aperture of the objective lens, ensuring diffraction limited focal volume. This was achieved with a two times expansion telescope constructed from $f_{150\text{mm}}$ and $f_{300\text{mm}}$ anti-reflection coated lenses. The pulse was redirected from a 532-nm, \varnothing 25.4-mm dichroic mirror (Thorlabs) into the back aperture of the objective. This permitted high-speed observation through the same objective, as

depicted in Figure 5.2. To control beam collimation prior to entering the objective lens, the pulse was passed through a $4f$ lens relay system comprised of two $f_{150\text{mm}}$ conjugate lenses. Two objective lenses were used for the observations presented; a $5\times/0.14$ NA, M Plan APO, infinity corrected lens (Mitutoyo, Aurora, IL), and a $50\times/0.42$ NA, M Plan, NIR, infinity corrected lens (Mitutoyo). The laser energy was measured at the back aperture of the objective using a S370C power meter (Thorlabs). Laser beam steering was achieved using $\varnothing 25.4\text{-mm}$ and $\varnothing 76.2\text{-mm}$ protected silver mirrors (Thorlabs). The high-speed camera was protected from scattered laser radiation using a dichroic band-pass filter 540 IB 50, $> 98\%$ at 532 nm (Comar Instruments, Cambridge, UK).

Schlieren imaging

Alignment between the acoustic and optical foci is critical to obtaining reproducible results. Therefore, a monochromatic Schlieren imaging setup was built around the optical windows of the cavitation chamber [93], orthogonal to the laser propagation axis. Schlieren imaging allows for the visualisation of density, or pressure, variations within transparent media [3]. A 30-lm, Lambertian Luxeon V Star, 470-nm light-emitting diode (LED) (Lumileds Lighting, LLC, San Jose, CA) was used as a continuous light source in combination with two $\varnothing 50.8\text{-mm}$, $f_{150\text{mm}}$ lenses (Comar Instruments) to generate a collimated beam across the optical window. Large lenses were used to fully cover the cavitation chamber. A razor blade was mounted on a vertical translation slide to provide the zero-order stop, whilst the image was projected onto a white screen. A Schlieren shadowgraph showing the laser spot and the acoustic focus during the alignment procedure is shown in Figure 5.5@. The shadow of the needle hydrophone used to record acoustical data during cavitation experiments is also apparent in this image.

5.3 High-speed photography

High-speed cameras may be incorporated into the experiment via one of two possible configurations. As depicted in Figures 5.1 and 5.2, imaging can be achieved through the same objective that focuses the laser into the ultrasound field. There is also the option of imaging through a second objective lens, orthogonal to the laser propagation direction, once the Schlieren optics have been removed, following the alignment procedure. The fibre optic bundle delivering the flash illumination to the cavitation chamber must also be rotated through 90° , from the position represented in Figure 5.1 and 5.2. This configuration offers the additional

advantage of image focussing independently from that of the laser pulse. The choice of high-speed camera is largely determined by the frame rate required to observe a particular cavitation-related phenomenon. In this chapter results obtained with two high-speed cameras: a Shimadzu HPV-1 (Shimadzu, Kyoto, Japan), and a Cordin Model 550-62 device (Cordin, Salt Lake City, UT) are presented. The former consists of a single CCD sensor capable of recording 100 frames of 312×260 pixels at frame rates up to 1 million frames per second (Mfps), at minimum exposure times of 125 ns. The latter is a gas-driven, rotating mirror camera capable of recording 62 frames of 1000×1000 pixels at frame rates up to 4 Mfps, when using compressed helium gas to rotate the turbine. The Model 550-62 is capable of minimum exposure times of 250 ns. For high-speed camera data acquisition rates that did not necessitate flash illumination, an LB60 continuous fibre-optic light source (Welch Allyn, Skaneateles Falls, NY) coupled to a \varnothing 4-mm fibre-optic cable; capable of providing 7.96×10^6 lux at the exit surface of the fibre-optic cable was used. For higher acquisition rates, a Model 659 (Cordin) Xenon flash system was used, coupled to the fibre-optic bundle via a condenser lens (Comar Instruments). The flash-head provided 3.23×10^6 lux at 3 m, with adjustable duration of up to 1 ms. The exit end of the fibre-optic cable was positioned 2 mm from the surface of the cavitation chamber. To ensure synchronisation of the laser pulse, flash illumination and high-speed camera operation, each component was electronically triggered with appropriately delayed TTL pulses. In the results presented, $t = 0 \mu\text{s}$ is defined as the frame at which the laser pulse is incident to the cavitation chamber. The pre-trigger option on the high-speed cameras was used to trigger the waveform generator providing the sinusoid for the ultrasound, which in turn sent two trigger pulses to the laser at $t = -120 \mu\text{s}$, to account for the Q-switch delay, and to the flash capacitor bank at $t = -70 \mu\text{s}$, to allow the intensity to rise for maximum illumination. High-speed camera operation was set internally to $t = -10 \mu\text{s}$ to capture a number of frames before cavitation activity was initiated.

5.4 Results and discussion

At the mechanical indices used here, no cavitation was observed within the field-of-view of the high-speed cameras, prior to laser pulse irradiation.

Figure 5.6 provides representative images extracted from high-speed sequences recorded at 0.5 Mfps of laser-induced cavitation. Figure 5.6@ demonstrates conventional, plasma-mediated cavitation, whereby optical breakdown resulted from absorption of a 1.2-mJ laser pulse, above the threshold pulse energy required

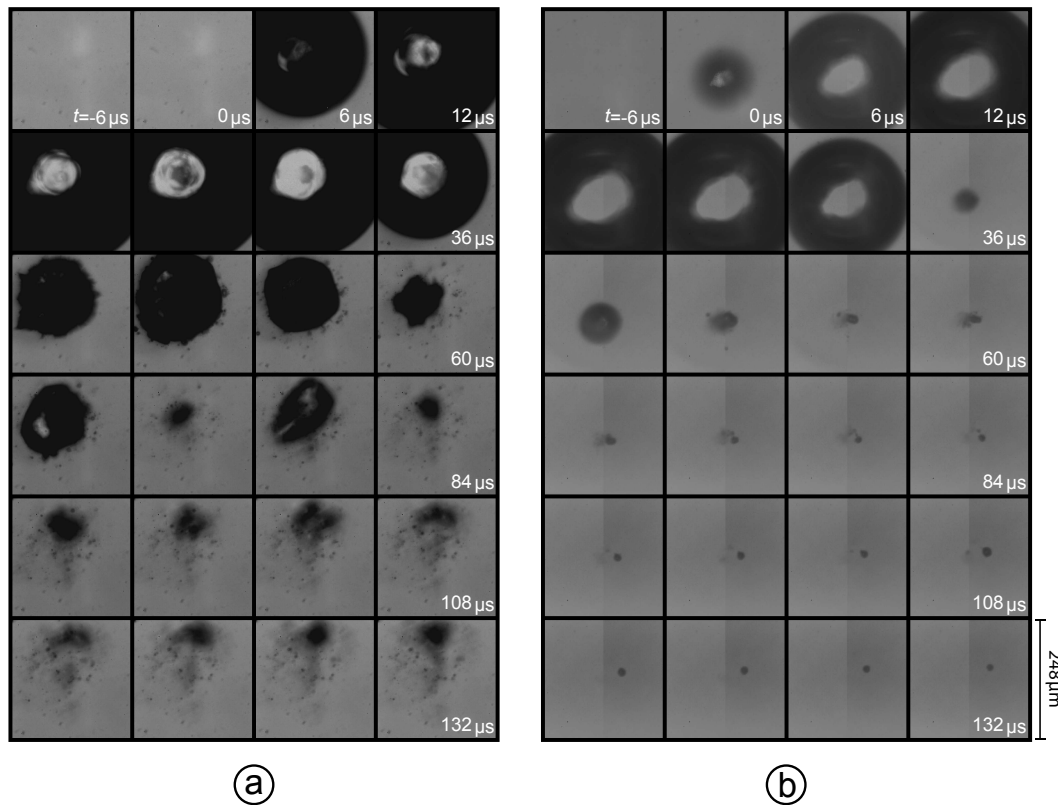


Figure 5.6: Cavitation recorded with the HPV-1 high-speed camera at 0.5 Mfps, with simultaneous imaging and focussing the laser pulse through the 50 \times objective lens. (a) Laser-induced cavitation from a 1.2-mJ laser pulse. (b) Laser-induced cavitation in a pre-established focussed ultrasound field of 1.47 MHz and MI=1.1. Each frame corresponds to a $248 \times 248 (\mu\text{m})^2$ area.

to generate a cavity. This threshold energy was determined to be 1.1 mJ for this system. Rapid expansion resulted in the $248 \times 248 (\mu\text{m})^2$ field-of-view becoming overfilled, within the first few microseconds after absorption, through to $36 \mu\text{s}$, when the cavity entered the first collapse phase. This was followed by a number of rebound inflations, at 48, 66, and $78 \mu\text{s}$, driven by the inertia of the liquid and compressibility of the gas. During these oscillations microbubble debris formed, and moved with the liquid surrounding the oscillating primary cavity. The cavity translated upward from $66 \mu\text{s}$ onwards. This may be associated with the asymmetry of the inflation at $78 \mu\text{s}$. Otherwise, the geometric centre of the activity remained static throughout the event, since buoyancy effects are negligible over these timescales.

Figure 5.6(b) shows an event where the same laser-pulse energy was incident to the focal region of a pre-established ultrasound field of MI=1.1. Similar to Figure 5.6(a), the initial $36 \mu\text{s}$ of the sequence were dominated by the rapid

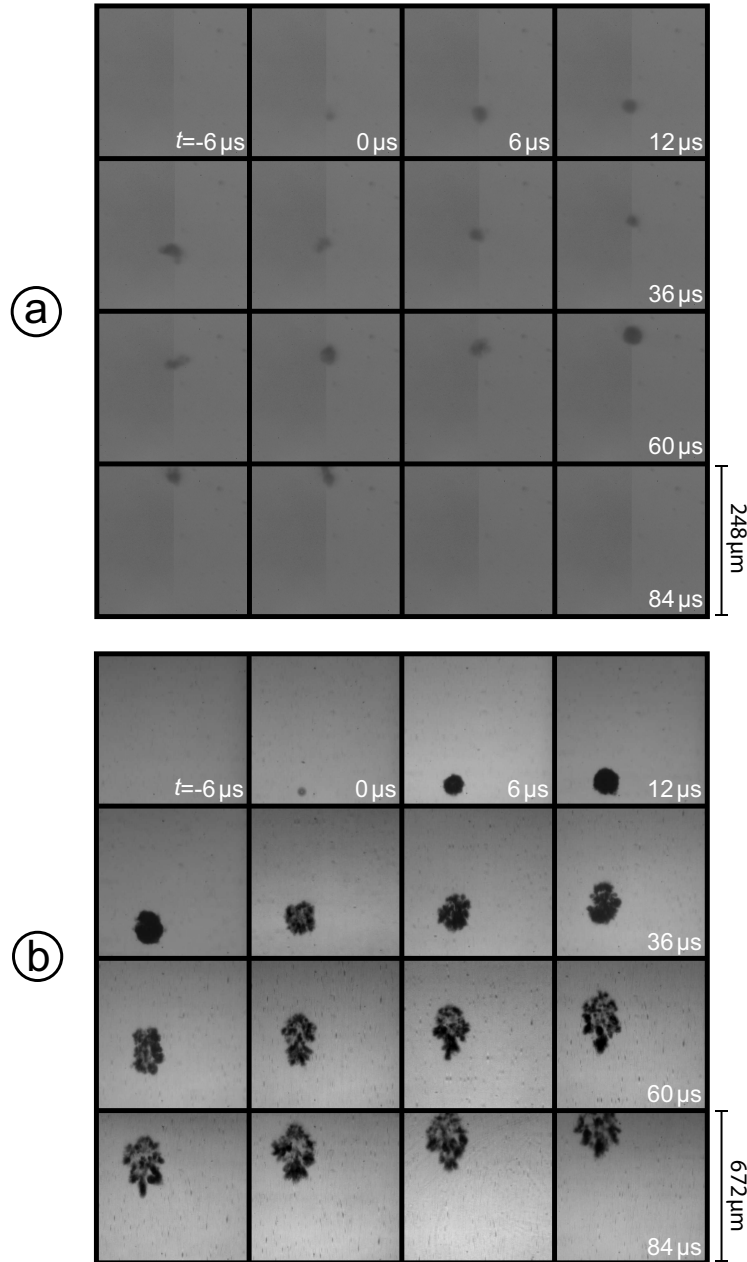


Figure 5.7: (a) Laser-nucleated acoustic cavitation recorded with the Shimadzu HPV-1 camera at 0.5 Mfps, with simultaneous imaging and focussing the laser pulse through the 50 \times objective lens. A 0.95 mJ laser pulse was focussed into the focal volume of the ultrasound field, of identical parameters to that of Figure 5.6(b). Each frame corresponds to a $248 \times 248 (\mu\text{m})^2$ area. (b) Laser-nucleated cavitation in a field of higher MI=3.4, recorded with the Cordin 550-62 high-speed camera, at 0.5 Mfps. For this sequence, imaging was performed through the 5 \times objective, in the orthogonal configuration described in Section 5.3, to achieve a larger field-of-view of $672 \times 672 (\mu\text{m})^2$. The laser pulse was focussed through the 50 \times objective.

expansion and subsequent collapse of the laser-induced cavity. A single secondary inflation was observed at 42 μs , of a maximum diameter notably smaller than at the equivalent time in Figure 5.6Ⓐ. Further re-inflations were suppressed by the presence of the ultrasound field, as was the level of microbubble debris. At 60 μs , a small cloud of debris started to translate upward, in the direction of ultrasound propagation, owing to primary radiation forces [66, 75], at an average velocity of 1.0 m s^{-1} . The formation of the cavitation clouds themselves is also determined by secondary radiation (Bjerknes) forces [66, 75, 85]. For a complete review on cloud dynamics, Section 12 of Lauterborn & Kurz [74] is referred to.

Figure 5.7Ⓐ represents a process termed laser-nucleated acoustic cavitation, to distinguish it from laser-induced cavitation in an ultrasound field, such as that of Figure 5.6Ⓓ. Here, a 0.95 mJ laser pulse, which is below the optical cavitation threshold for this system under ambient pressure conditions, nucleated cavitation activity in the pre-established ultrasound field. Rather than the rapid expansion of the laser-induced cavity, to a maximum diameter of a few hundred micrometers, a microcavity with a maximum diameter of 14 μm was formed at $t=0 \mu\text{s}$. It translated owing to primary radiation forces, at an average velocity of 1.5 m s^{-1} , whilst undergoing volumetric oscillations.

Figure 5.7Ⓑ represents selected images from a sequence of laser-nucleated acoustic cavitation in an ultrasound field of significantly increased acoustic pressure ($MI=3.4$) with a 0.95-mJ laser pulse. Here, a single cavity of 25 μm diameter formed at $t=0 \mu\text{s}$, and initiated that later revealed itself to be a cavitation cloud: a larger number of distinct cavities, interacting, coalescing and reforming, but also exhibiting collective behaviour as a single entity due to primary and secondary radiation forces [66, 75, 85]. The cloud retained sphericity for 18 μs , but elongated in the direction of the ultrasound propagation axis from 36 μs , before adopting a mushroom-shaped morphology at 54 μs , reminiscent of the cap-like structures reported previously [15]. These morphology changes were accompanied by rapid translation of the cloud, owing to primary radiation forces, with an average velocity of 7.0 m s^{-1} .

Figure 5.8Ⓐ shows the hydrophone signal recorded during the laser-nucleated acoustic cavitation of Figure 5.7Ⓑ, with the laser pulse incident to the ultrasound focus at $t=120 \mu\text{s}$. The sudden increase in signal corresponds to high-speed observations of the onset of cavitation activity, which decays as the cluster translates away from the hydrophone tip position, under the primary radiation force. Figure 5.8ⒷⒶ shows the spectrum of the notch-filtered hydrophone signal of the first 120 μs , *i.e.*, the signal of the pre-established ultrasound field. The presence of

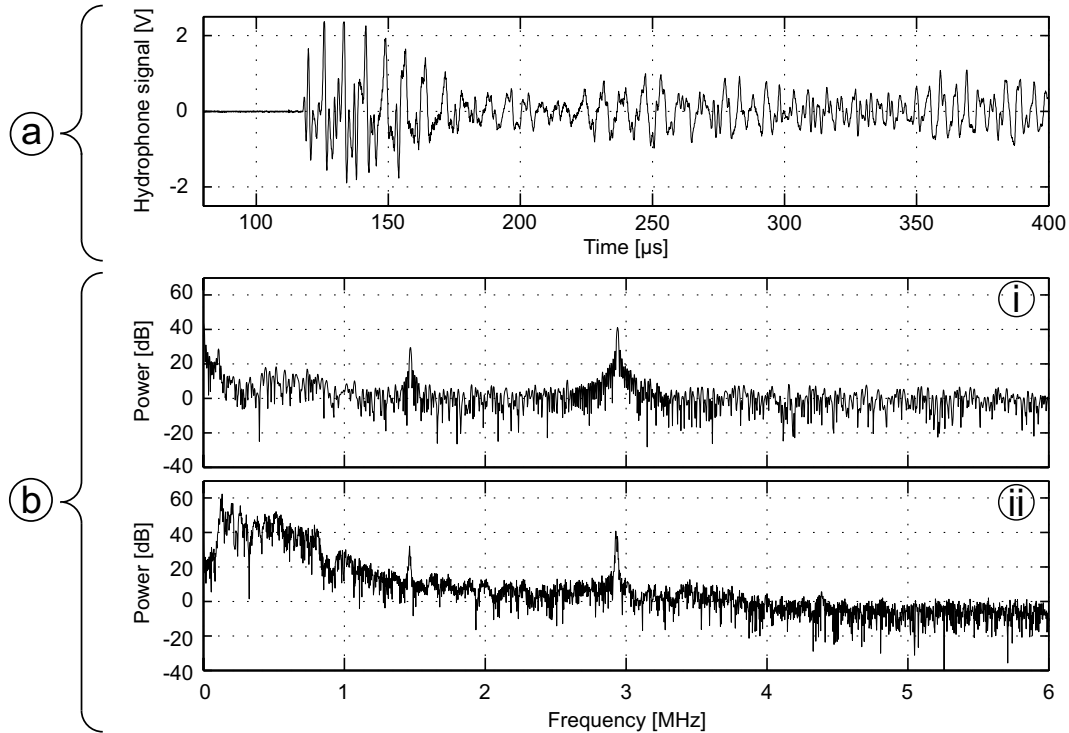


Figure 5.8: (a) The acoustic signal recorded from the hydrophone positioned within the cavitation chamber, as depicted in Figure 5.5, notch-filtered at 1.47 MHz, recorded during the high-speed images of laser-nucleated cavitation depicted in Figure 5.7(b). (i) The spectra of the first 120 μs of the signal and (ii) the remaining 280 μs , during laser-nucleated acoustic cavitation.

a second harmonic peak and the absence of broadband emissions suggest stable cavitation outside the field-of-view before the laser pulse had been generated. Figure 5.8(b)(ii) represents the spectrum of the hydrophone signal from 120–400 μs , which exhibits harmonic. In addition, a strong increase in acoustic emissions from 100 kHz to 1 MHz is evident. This suggests that the laser-nucleated acoustic cavitation of Figure 5.7(b) is inertial.

5.5 Conclusions

It has been demonstrated that acoustic cavitation can be forced to occur at a specific location in a liquid, by using a low energy, nanosecond laser pulse to nucleate activity in a pre-established ultrasound field. The low pulse energy avoids the large, plasma-mediated cavities, generally associated with optical cavitation. It also permits the incorporation of high-speed cameras to image the dynamics at microsecond temporal and micrometer spatial resolutions. This technique will contribute to the understanding of cavitation evolution in focussed ultrasound,

including for potential therapeutic applications in focussed ultrasound surgery.

6

Sonoporation at a low MI

Abstract

In this study the physical mechanisms of sonoporation are investigated in order to understand and improve ultrasound-assisted drug and gene delivery. Sonoporation is the transient permeabilisation and resealing of a cell membrane with the help of ultrasound and/or an ultrasound contrast agent, allowing for the trans-membrane delivery and cellular uptake of macromolecules between 10 kDa and 3 MDa.

The behaviour of ultrasound contrast agent microbubbles near cancer cells at low acoustic amplitudes was studied. After administering an ultrasound contrast agent, HeLa cells were subjected to 6.6-MHz ultrasound with a mechanical index of 0.2 and observed with a high-speed camera.

Microbubbles were seen to enter cells and rapidly dissolve. The quick dissolution after entering suggests that the microbubbles lose (part of) their shell whilst entering.

It was demonstrated that lipid-shelled microbubbles can be forced to enter cells

Based on: Delalande A, Kotopoulos S, Rovers T, Pichon C, Postema M. Sonoporation at a low mechanical index. *Bub Sci Eng Tech* **2011** 3(1):accepted.

This work has been supported by DFG Emmy Noether Programme Grant 38355133, EPSRC Grant EP/F037025/1, and the HERI Research Pump Priming Fund. The authors are grateful to Conseil Regional for A. Delalande's fellowship.

at a low mechanical index. Hence, if a therapeutic agent is added to the shell of the bubble or inside the bubble, ultrasound-guided delivery could be facilitated at diagnostic settings. In addition, these results may have implications for the safety regulations on the use of ultrasound contrast agents for diagnostic imaging.

6.1 Introduction

Sonoporation is the transient permeabilisation and resealing of a cell membrane with the help of ultrasound and/or an ultrasound contrast agent, allowing for the trans-membrane delivery and cellular uptake of macromolecules between 10 kDa and 3 MDa [104]. Many studies have demonstrated increased drug and gene uptake of sites under sonication [6, 17, 43, 64, 70, 77, 128, 132]. These studies presumed, that a physical membrane disruption mechanism, *i.e.*, sonoporation, caused the increased uptake, as opposed to naturally occurring active uptake processes, such as endocytosis, that are controlled by the system biology [6, 17, 43, 64, 70, 77, 128, 132]. Although mechanical disruption with the aid of ultrasound has been attributed to violent side effects of inertial cavitation and microbubble fragmentation, most notably, the increased uptake has also been observed at low acoustic amplitudes, *i.e.*, in acoustic regimes where inertial cavitation and microbubble fragmentation are not to be expected [28]. An ultrasound contrast agent microbubble might act as a vehicle to carry a drug or gene load to a perfused region of interest. If the same ultrasound field that has been implicated in the sonoporation process can cause release of the therapeutic load, this load could be delivered into cells. Apart from plainly mixing ultrasound contrast agents with therapeutic agents, several schemes have been proposed to incorporate therapeutic loads to microbubbles. These include loads to the microbubble shell [62], therapeutic gases inside the microbubble [100], gas-filled lipospheres containing drugs [123], and drug-filled antibubbles [103]. To understand and ameliorate ultrasound-assisted drug and gene delivery, the physics of controlled release and of sonoporation have been under investigation. That objective also forms the focus for this chapter. Moreover, the behaviour of ultrasound contrast agent microbubbles near cancer cells deliberately at low acoustic amplitudes in order to probe whether sonoporation in this regime was possible was studied; and if so, to ascertain what the microscopic mechanism might entail; and finally, to assess and scrutinise the safety aspects of ultrasound exposure in this regime.

6.1.1 Mechanical index

On commercial scanners, the MI has been limited to 1.9 for medical imaging [139]. At low MI, microbubbles pulsate linearly, whereas at high MI, their greater expansion phase is followed by a violent collapse. During the collapse phase, when the kinetic energy of the bubble surpasses its surface energy, a bubble may fragment into a number of smaller bubbles. Fragmentation has been exclusively observed with contrast agents with thin, elastic shells. Fragmentation is the dominant disruption mechanism for these bubble [111]. Although the fragmentation of therapeutic load-bearing microbubbles must release their loads, the actual drug or gene delivery is in this case a passive process, dependent on diffusion rate and proximity to the target cells. Fragmenting microbubbles may not create pores in cells, since fragmentation costs energy. However, if a microbubble collapses near a free or a solid boundary, the retardation of the liquid near the boundary may cause an asymmetry. This asymmetry causes differences in acceleration on the bubble surface. During further collapse, a funnel-shaped jet may protrude through the microbubble, shooting liquid to the boundary [98]. The pore size created by a jet has been empirically related to the microbubble expansion [63]. If jets could be directed to cell layers, in case of a microbubble carrying a therapeutic load, the load could be delivered into cells. The jet formation is affected by the cavitation topology, synergistically interacting with local fluid dynamics arising through the bubble's expansion and contraction due to the ultrasound field. However, as the fluid forming the microjet is just the bulk fluid which carries no therapeutic agent, then there is no guarantee that, even with the formation of a sonopore due to jet impact with the cell membrane, therapeutic agent will enter the cell. It needs to be dislodged and mobilised from the bubble first. Furthermore, jetting has not been observed at low or moderate MI [112], so that fragmentation is likely to occur before any delivery takes place. By pushing the loaded microbubbles towards the vessel all using primary radiation forces [24], release can take place closer to target vessels. In a recent study, Caskey *et al.* pushed bubbles into tissue-mimicking gels at MI=1.5 [13]. It was previously studied how microclusters consisting of lipid-encapsulated microbubbles can be formed using primary and secondary radiation forces, and how these clusters can be pushed towards vessel walls [66]. It was found that, even at MI<0.15, microbubble clusters can be formed and pushed towards a boundary within seconds.

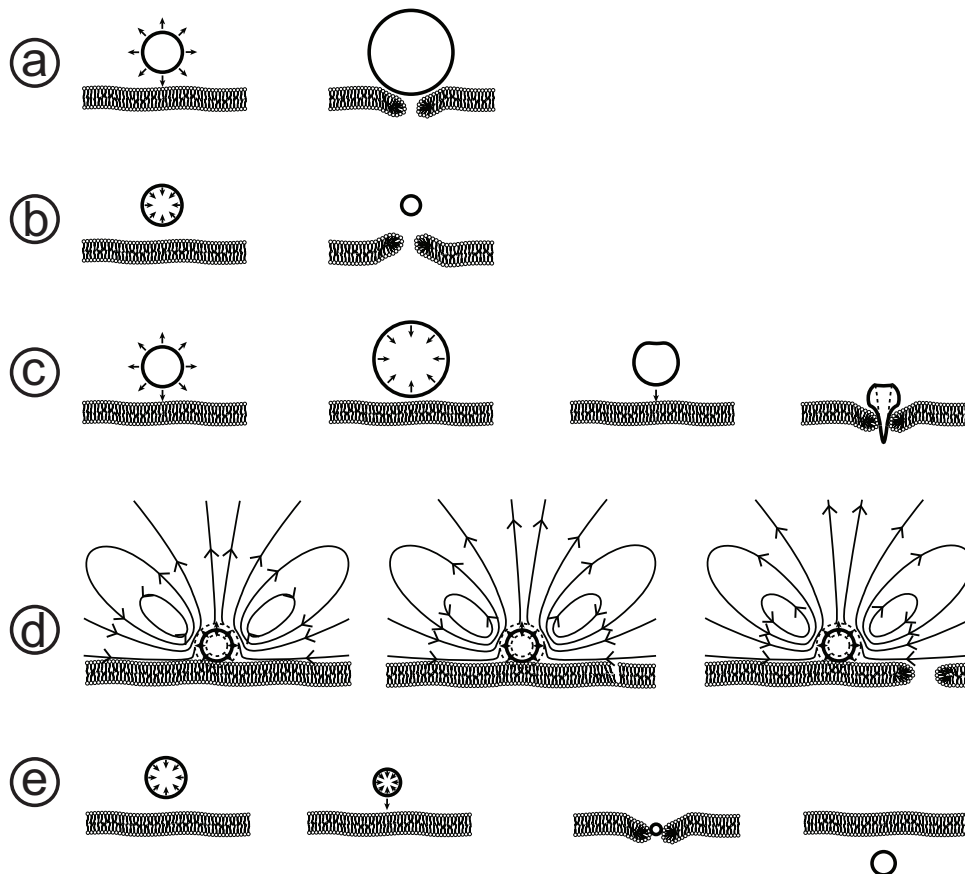


Figure 6.1: Possible mechanisms of sonoporation: ① push, ② pull, ③ jetting, ④ shear, ⑤ translation. Based on Figure 9.2 in Postema *et al.* [107].

6.1.2 Sonoporation

There are five non-exclusive hypotheses for explaining the sonoporation phenomenon. These have been summarised in Figure 6.1: push, pull, jetting, shear, and translation [107]. It has been hypothesised that expanding microbubbles might push the cell membrane inward, and that collapsing bubbles might pull cell membranes outward [141]. These mechanisms require microbubbles to be present in the close vicinity of cells. A separate release mechanism should then ensure localised delivery. Although jetting only occurs in a high-MI regime, it is very effective in puncturing cell membranes. Jetting has been observed through cells using ultrasound contrast agent microbubbles. However, the acoustic impedance of the solid cell substratum formed the boundary to which the jetting took place, not the cell itself [114]. Also, there has not been any proof yet of cell survival after jetting. In a separate study, the role of jetting as a dominant mechanism in sonoporation was excluded [105]. If a microbubble is fixed to a membrane, the fluid streaming around the oscillating bubbles creates enough shear

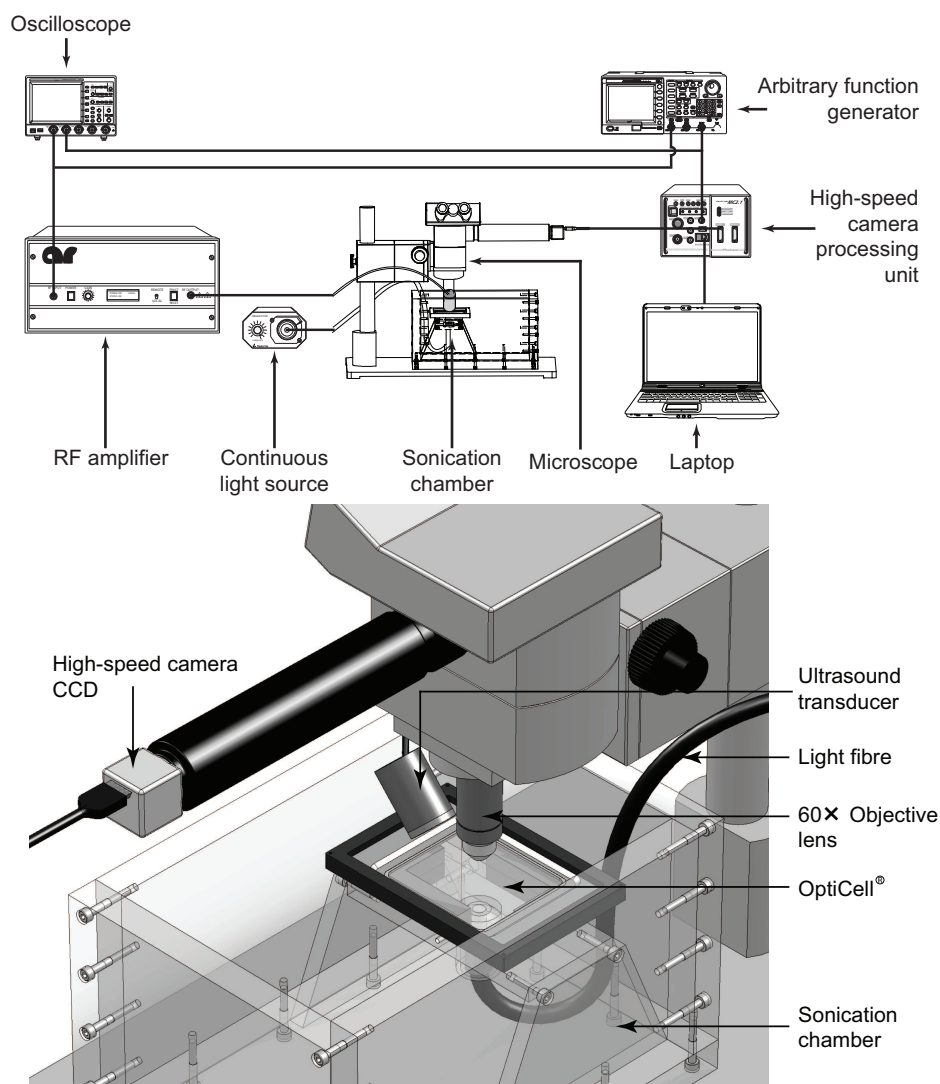


Figure 6.2: Experimental setup (*top*) and a close-up of the sonoporation configuration (*bottom*).

to rupture the membrane [82]. Here again, separate release mechanisms should then ensure localised delivery. Finally, it has been speculated that lipid-encapsulated microbubbles, in compressed phase, translate through cell membranes or channels in the cell membrane such as the receptor. In case of therapeutic loading, the load would be delivered directly into the target cell. The main advantage of the latter mechanism is that microbubble translation by means of ultrasonic radiation forces requires very low acoustic pressures. Hence, potential damaging bioeffects due to inertial cavitation can be ruled out.

6.2 Materials and methods

6.2.1 Sonoporation configuration

In previous studies, increased gene uptake was demonstrated at $MI < 0.3$ [27, 59]. Similar sonoporation configuration was used for these experiments. An overview of the experimental setup is shown in Figure 6.2. A signal consisting of 50 cycles with a centre frequency of 6.6 MHz and a pulse repetition frequency of 10 kHz, *i.e.*, a duty cycle of 7.5%, was generated by an AFG 3102, dual channel arbitrary function generator (Tektronix, Inc., Beaverton, OR), amplified by a 150A250 radio-frequency (RF) amplifier (Amplifier Research, Souderton, PA) set to maximum gain, and fed to a custom-built 6.6-MHz ultrasound transducer with a hexagonal Y-36° lithium niobate element with a maximum diameter of 25 mm [67]. The peak-negative acoustic pressure was measured to be 0.5 MPa in a separate tank and in the sonication chamber itself. This corresponds to an MI of 0.2. The transducer was placed in a custom-built, $260 \times 160 \times 150$ (mm)³ Perspex sonication chamber, in which an OptiCell® cell culture chamber (Nunc GmbH & Co. KG, Langenselbold, Germany) was placed. One side of the cell culture chamber contained a monolayer of 1.6×10^6 HeLa cells that had been cultured in MEM with Earl's salts medium (PAA Laboratories GmbH, Pasching, Austria) supplemented with 10% v/v heat-inactivated foetal calf serum, GlutaMAX™ (Life Technologies Gibco, Paisley, Renfresshire, UK), 1% v/v of non-essential amino-acids (PAA), penicillin ($100 \text{ units ml}^{-1}$) and streptomycin ($100 \mu\text{g ml}^{-1}$) (PAA), at 37°C in a humidified atmosphere containing 5% CO₂. The cells were used when there was 60–80% confluency. Ultrasound contrast agent was injected into the cell culturing chamber before each experiment. Several lipid-shelled ultrasound contrast agents were tested in this study. In this chapter, results of a 3.33% dilution of MicroMarker® (VisualSonics B.V., Amsterdam, Netherlands), a lipid-shelled agent with a mean diameter of 2.5 μm are presented. A customised BXFM-F microscope unit with an LCach N 20×/0.40 NA PhC (Olympus Deutschland GmbH, Hamburg, Germany) and a LUMPlanFL 60×/0.90 NA water-immersion objective (Olympus) was placed on top of the sonication chamber with the objective lens immersed in the water. The colour charge coupled device (CCD) of a PHOTRON FastCam MC-2.1 high-speed camera (VKT Video Kommunikation GmbH, Pfullingen, Germany) was connected to the microscope. The sensor was rotated to make sure that in all recorded movies, the ultrasound is directed from the left to the right of the frame.

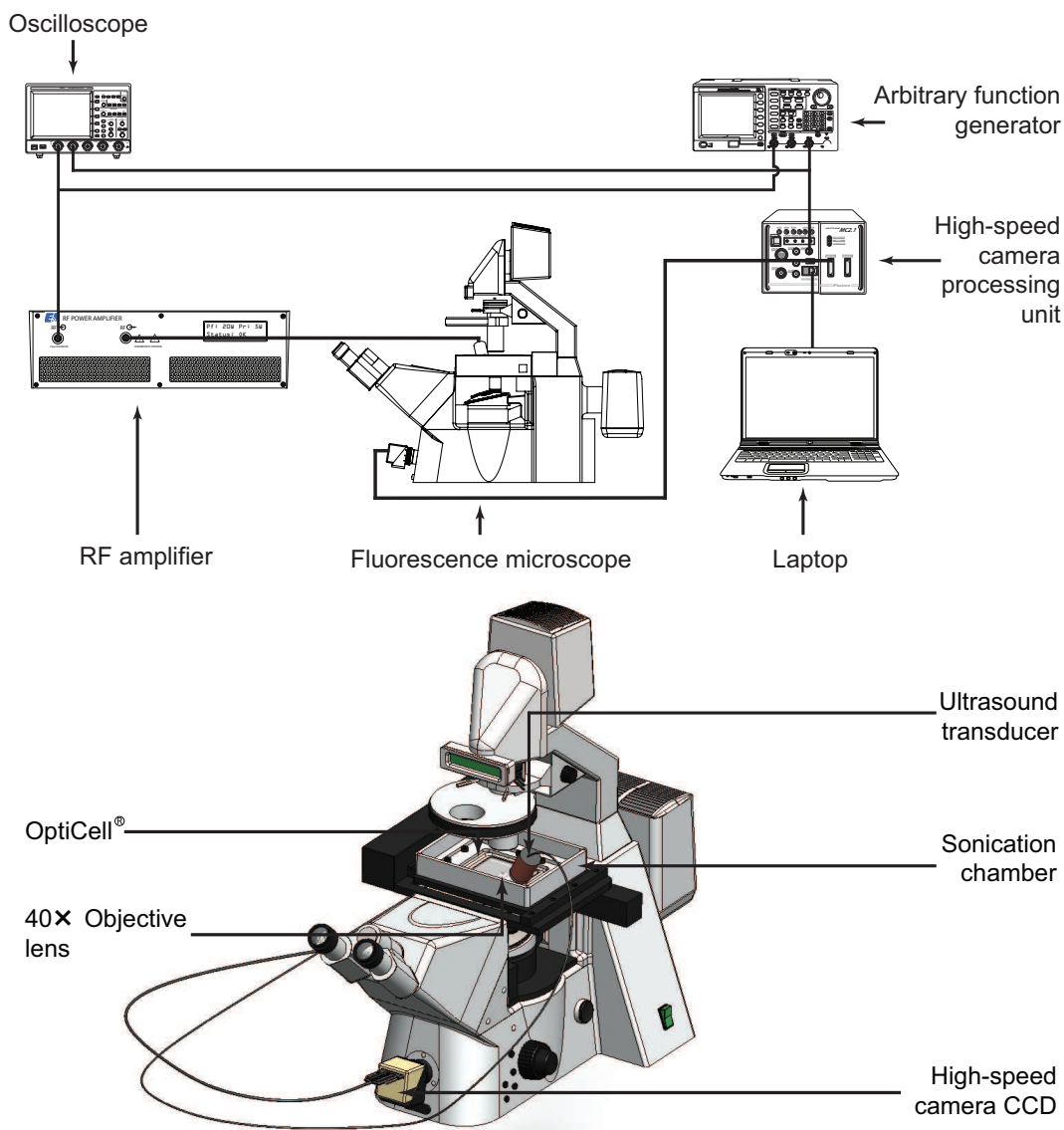


Figure 6.3: Experimental setup (*top*) and a close-up of the fluorescence configuration (*bottom*).

6.2.2 Fluorescence configuration

An overview of the setup used for the fluorescence experiments is shown in Figure 6.3. It is almost identical to the setup described in the previous section. However, here, the signal consisted of 40 cycles with a centre frequency of 6.6 MHz and a pulse repetition frequency of 10 kHz, *i.e.*, a duty cycle of 6.1%, was amplified using a 2100L, 50-dB RF amplifier (Electronics & Innovation Ltd., Rochester, NY) and fed to a custom-built 6.6-MHz ultrasound transducer [67]. In this configuration the ultrasound propagated from the bottom-right, to the top-left of the frame.

Prior to injection in the OptiCell[®], the MicroMarker[®] contrast agent was labelled using a DiD (DiI_{C₁₈(5)}) lipophilic fluorescent probe (Vybrant[™] Molecular

probes, Invitrogen, San Diego, CA). A ratio of 1 μl of DiD to 40 μl MicroMarker[®] was homogenised by pipetting and incubating for 5 minutes at room temperature. Figure 6.4 shows how the DiD fluorescent probe bonded to the phospholipid [78]. Emitted $\lambda=649\text{--}703$ nm fluorescence was localised on the microbubble shell when exciting at $\lambda=633$ nm.

A custom-made aluminium sonication chamber with internal dimensions of $130 \times 170 \times 35$ (mm)³ was locked into to the $x - y$ -stage of a 200M inverted confocal microscope (Carl Zeiss AG, Oberkochen, Germany) coupled with a LSM Axiovert 510 laser scanning device (Carl Zeiss), using an EC Plan-Neofluar 40 \times /1.30 NA Oil DIC M27 objective (Carl Zeiss AG), with automated z -stack functionality.

The peak-negative acoustic pressure was measured at the objective's field of view and corresponded to $MI=0.2$.

To evaluate the possible electrostatic attraction between microbubbles and cells, 30 μl MicroMarker[®] was diluted into 700 μl of distilled water and tested for electrophoretic mobility (ζ -potential) using a Zetasizer 3000 (Malvern Instruments, Malvern, Worcestershire, United Kingdom).

To measure the thickness of the cultured cells 10^5 HeLa cells were seeded into a OptiCell[®]. The cell plasma membrane was labelled with DiD lipophilic fluorescent probe (Vybrant[™] Molecular probes) according to the manufacturer's protocol. The membrane fluorescence was measured using a 200M confocal microscope. Cell thickness was calculated from the difference between the upper and lower slices where fluorescence was seen. In all fluorescence recordings, the slice thickness was set to <1 μm .

Twenty-three movies under 6.6-MHz sonication at frame rates between 500 and 2000 frames per second, representing 15 minutes of real-time exposure were recorded. Of these, 11 movies were recorded using fluorescence. In addition 10 control movies were recorded, with a total duration of 22 minutes.

6.3 Results and discussion

Throughout this section, the optical z -axis is defined from distal-to-focus (negative) to proximal-to-focus (positive), with $z = 0$ as the focal plane.

Figure 6.5 shows z -stacks of fluorescence emitted by the DiD dye attached to the membranes of four typical HeLa cells, representing the cell geometry. In total, the thicknesses of 42 cells were measured. The cultured cells were found to be 13 ± 2 μm thick. Clearly, these cells had thicknesses much greater than ultrasound contrast agent microbubble oscillations amplitudes at $MI=0.2$.

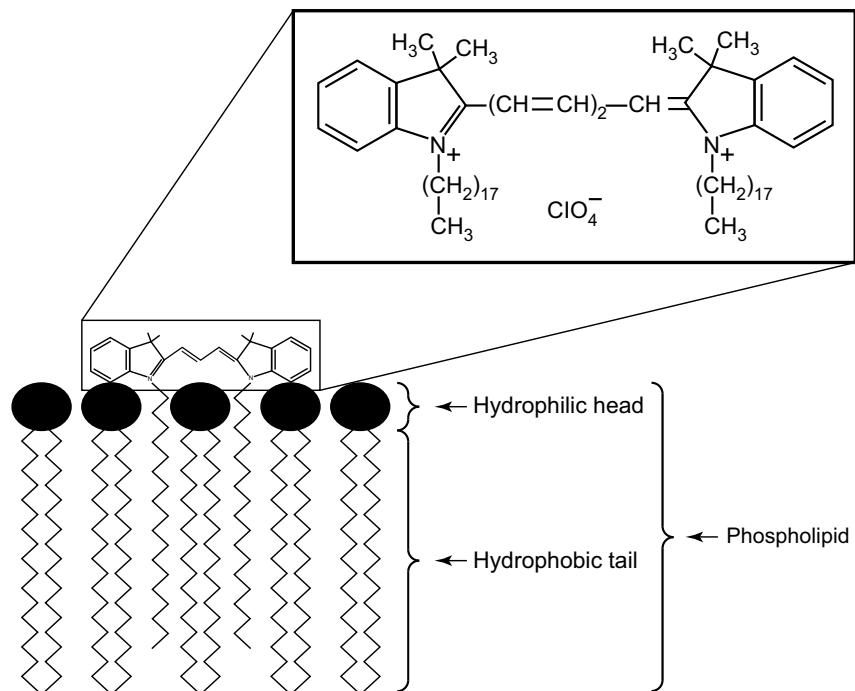


Figure 6.4: Schematic representation of DiD (DiI₁₈(5)) lipophilic fluorescent probe bonding to phospholipids [78].

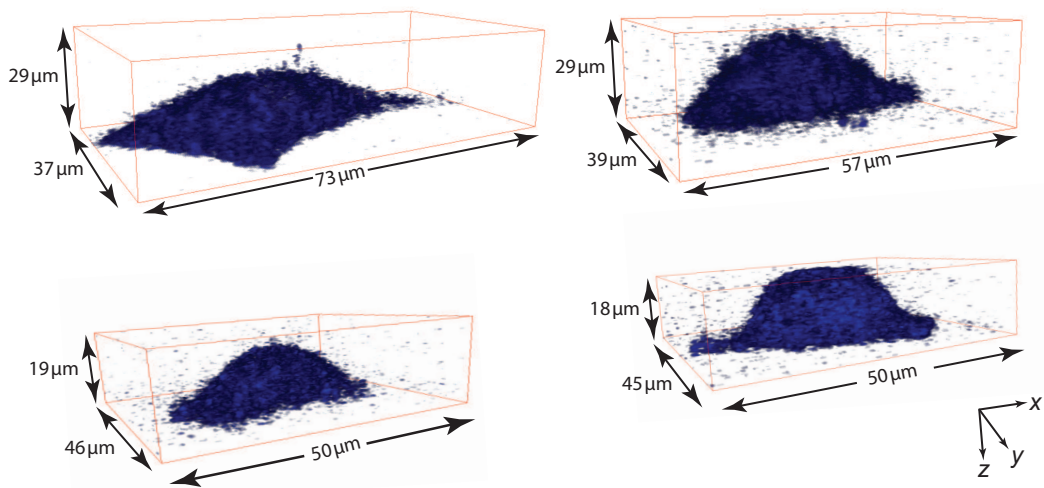


Figure 6.5: z-stacks of fluorescence emitted by the DiD dye attached to the membranes of four typical HeLa cells, representing the cell geometry.

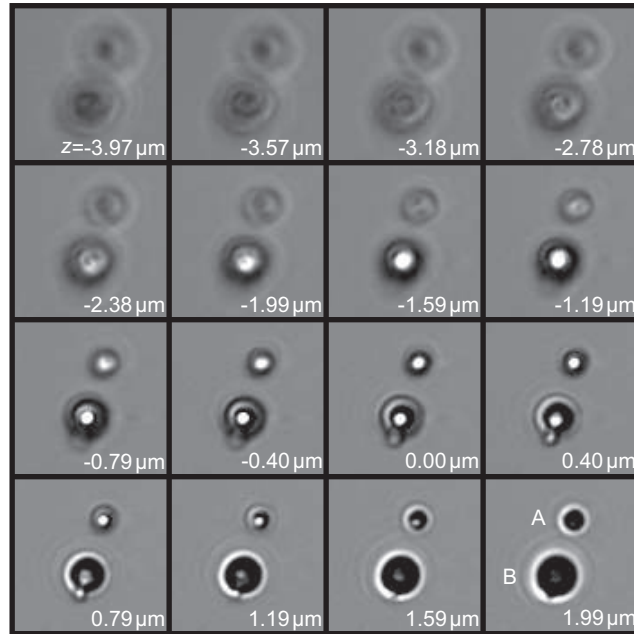


Figure 6.6: z -stack of two ultrasound contrast agent microbubbles. Proximal-to-focus Airy disks can be seen around the bubbles, whereas distal-to-focus the bubble boundaries are blurred. Microbubble “A” has a diameter of $2\ \mu\text{m}$, whereas microbubble “B” has a diameter of $3\ \mu\text{m}$. Each frame corresponds to a $11 \times 11\ (\mu\text{m})^2$ area.

The optical system was analysed and the results were compared to bubbles and cells that were slightly out of focus, to rule out that the movement of the bubble takes place in a plane different from that of the cell. Figure 6.6 shows a z -stack of two ultrasound contrast agent microbubbles, similar to Figure 10 of Postema *et al* [101]. Proximal-to-focus Airy disks can be seen around the bubbles, whereas distal-to-focus the bubble boundaries are blurred. Note that the boundary contrast is maximal just proximal-to-focus [101].

At a centre frequency of $6.6\ \text{MHz}$, 17 events of microbubbles entering HeLa cells were recorded. After entering, the microbubbles were observed to quickly dissolve. As an example, Figure 6.7 shows an event resampled at $3.4\ \text{Hz}$ and $40\ \text{Hz}$, respectively, here two bubbles were pushed to a cell during 11 s of sonication. A microbubble “A” of $4\text{-}\mu\text{m}$ diameter entered the cell and dissolved, whereas a microbubble “B” of $2\text{-}\mu\text{m}$ diameter stuck to the cell membrane.

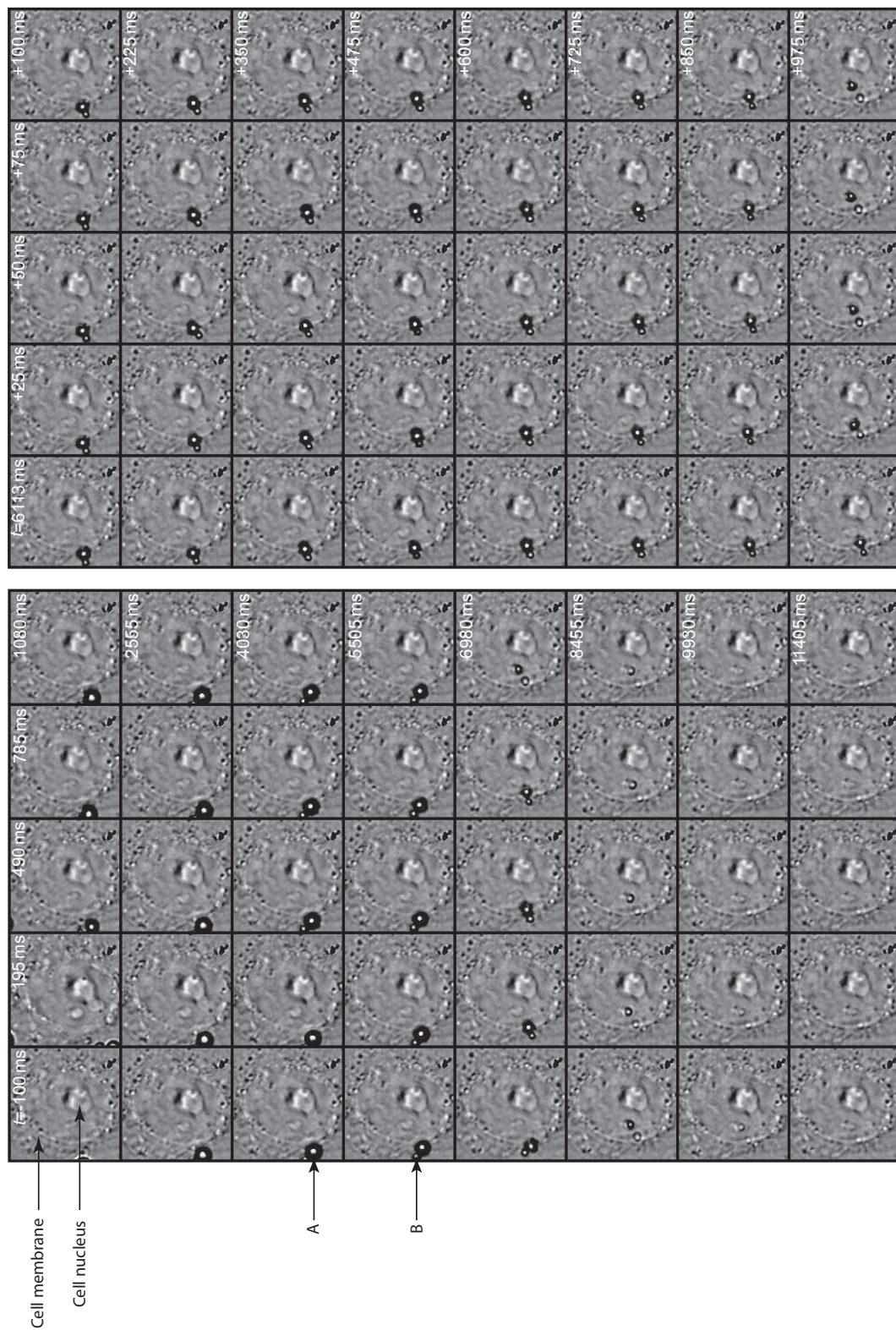


Figure 6.7: A sonoporation event including microbubble dissolution during 11 s of sonication (*left*) and selected frames of the microbubble entering a cell (*right*). Microbubble “A” entered the cell and dissolved, whereas microbubble “B” stuck to the cell membrane. Each frame corresponds to a $23 \times 23 \text{ } (\mu\text{m})^2$ area.

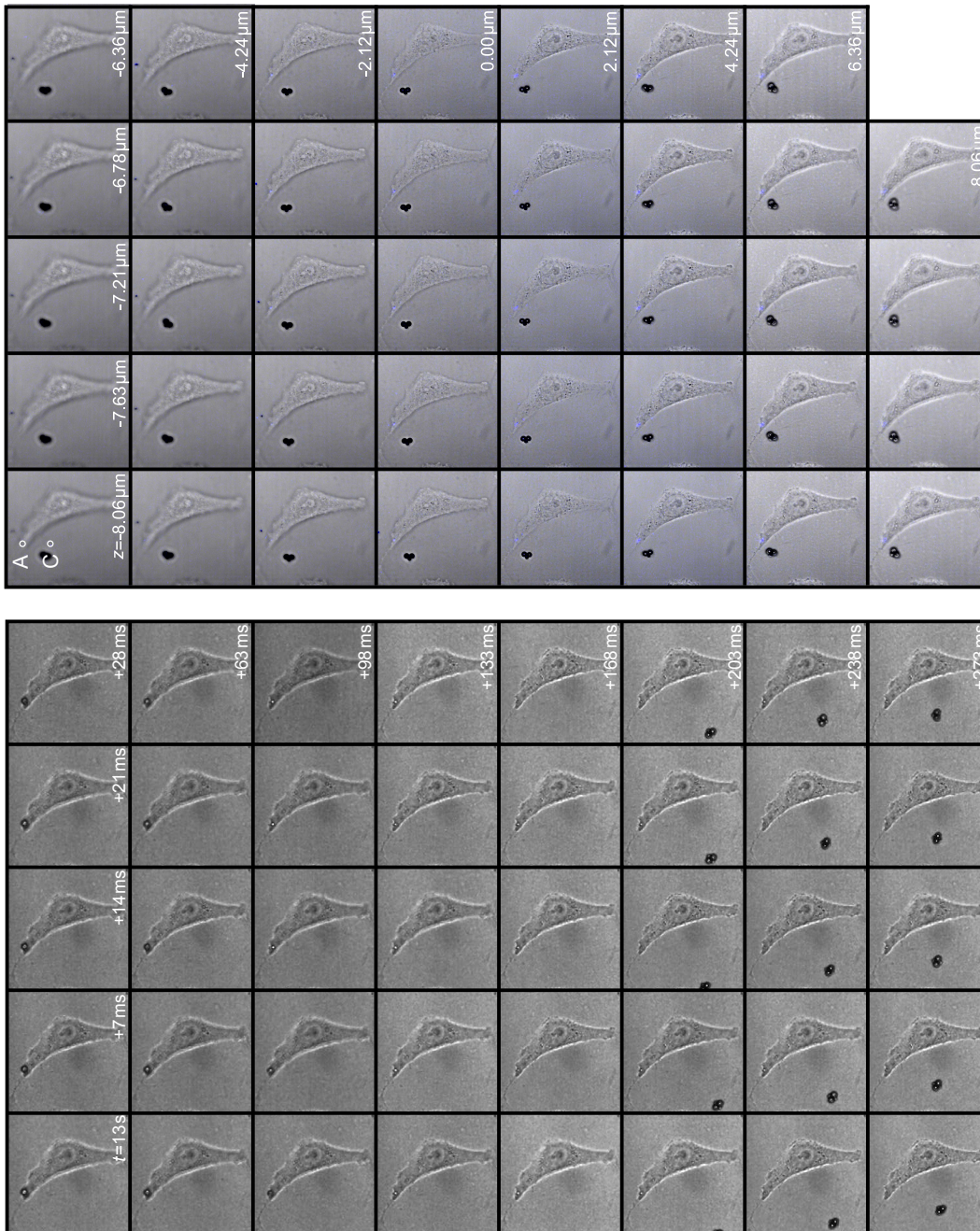


Figure 6.8: Microbubble of 5- μm diameter apparently penetrating through the cell membrane in optical focus (*left*); z-stack through the entire cell, to record whether the apparent microbubble entry is actually into the cell (*right*). Areas “A” and “C” are regions of interest inside and outside the cell, respectively. Each frame corresponds to a $76 \times 76 (\mu\text{m})^2$ area.

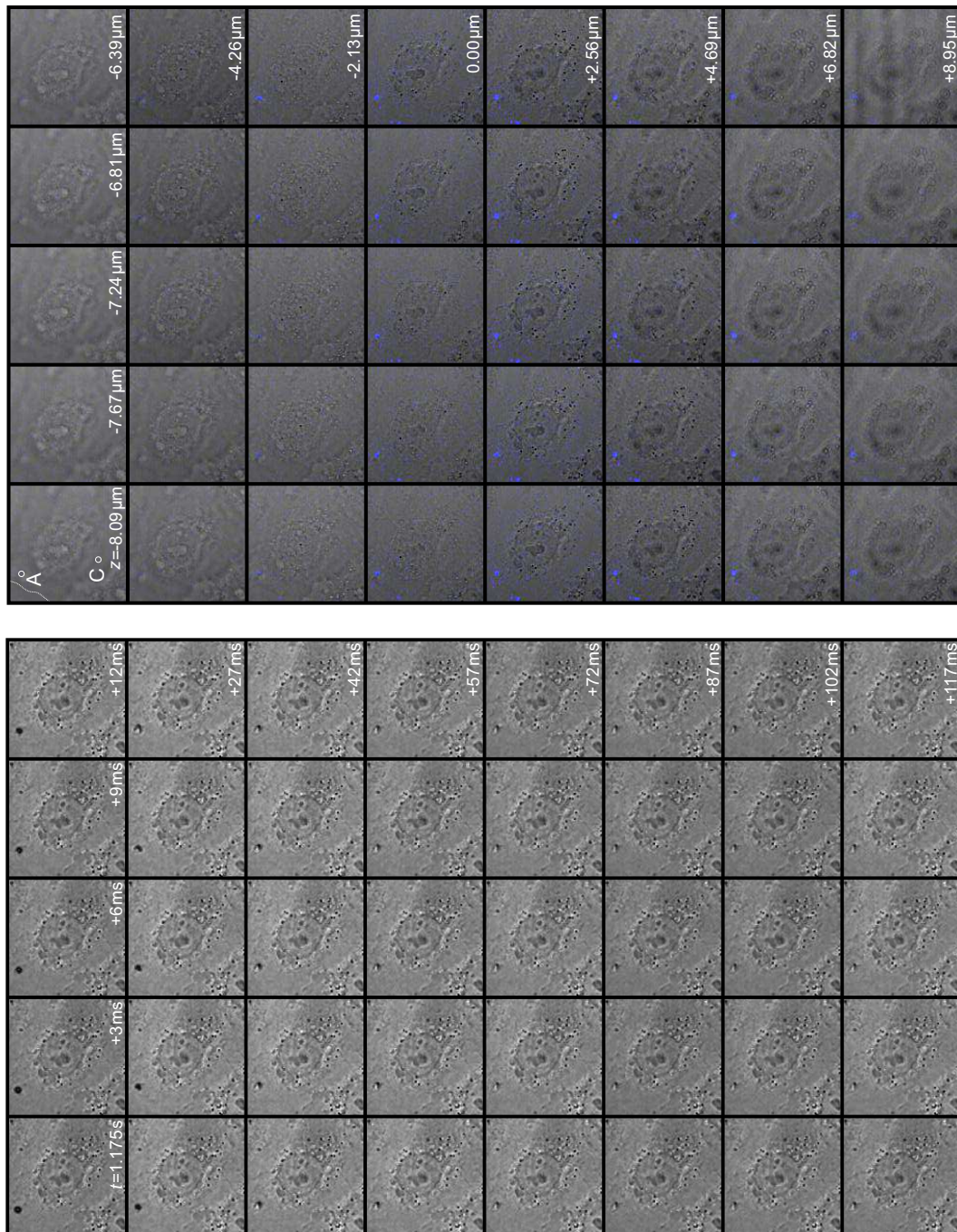


Figure 6.9: Microbubble of 4- μm diameter apparently penetrating through the cell membrane in optical focus (*left*); z-stack through the entire cell, to record whether the apparent microbubble entry is actually into the cell (*right*). Areas “A” and “C” are regions of interest of high fluorescence and low fluorescence, respectively, inside the cell. The white dotted lines in the upper left frame of the right panel indicates the cell membrane. Each frame corresponds to a $52 \times 52 (\mu\text{m})^2$ area.

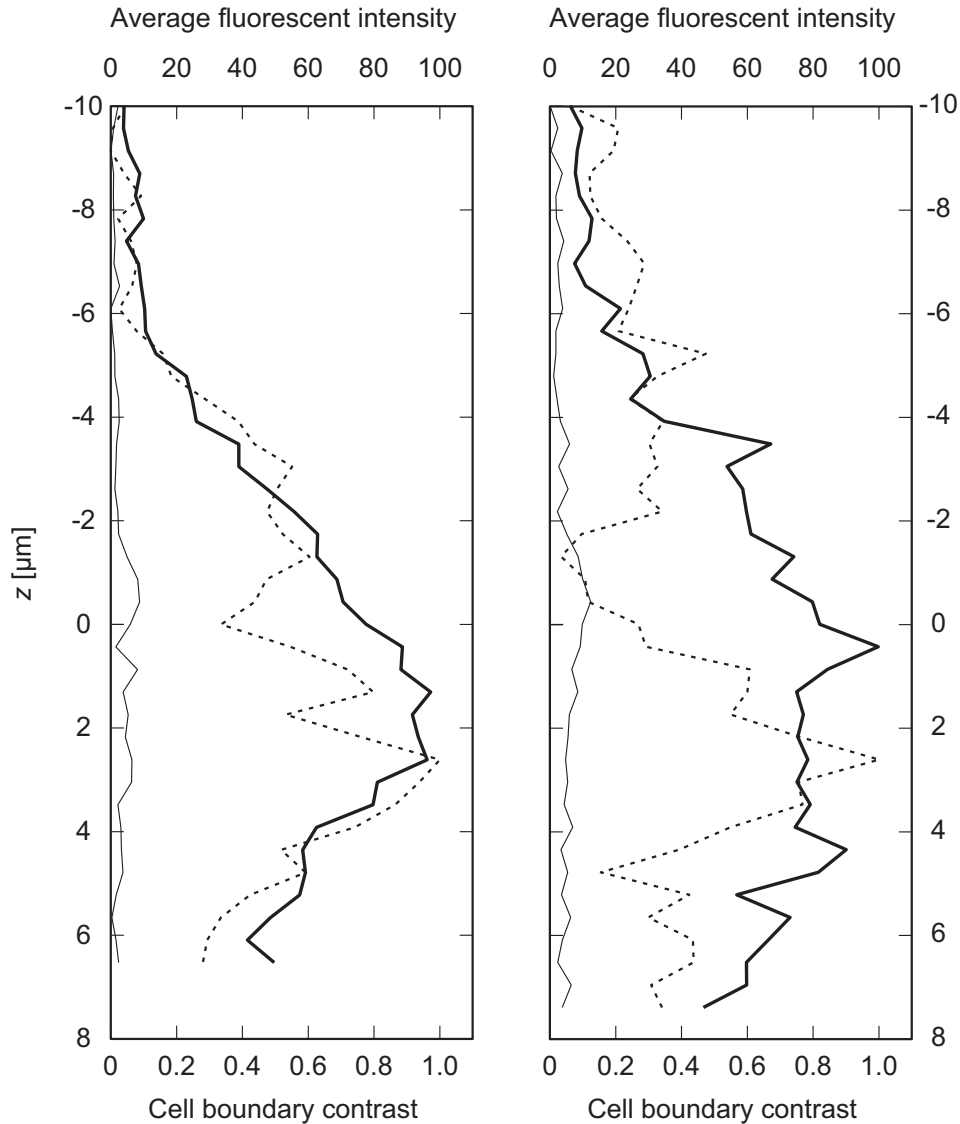


Figure 6.10: Average fluorescent intensities in the regions of interest (ROI) of Figures 6.8 (*left*) and 6.9 (*right*). Bold lines represent ROI “A” inside the cells, whereas hairlines represent ROI “C” the control regions. The dotted line represents the cell boundary contrast. Note that the cell boundary contrast is maximal just proximal-to-focus.

Figures 6.8 and 6.9 show two similar events, where fluorescence-coated microbubbles were used. The left panels show a microbubble apparently penetrating through the cell membrane in optical focus. Approximately 70 ms after the ultrasound is switched on a microbubble is seen to penetrate through the cell membrane in Figure 6.8. In Figure 6.9 the microbubble is seen to penetrate through the cell membrane approximately 24 ms after the ultrasound has been switched on. The right panels show a z -stack through the entire cell, to record whether the apparent microbubble entry is actually into the cell.

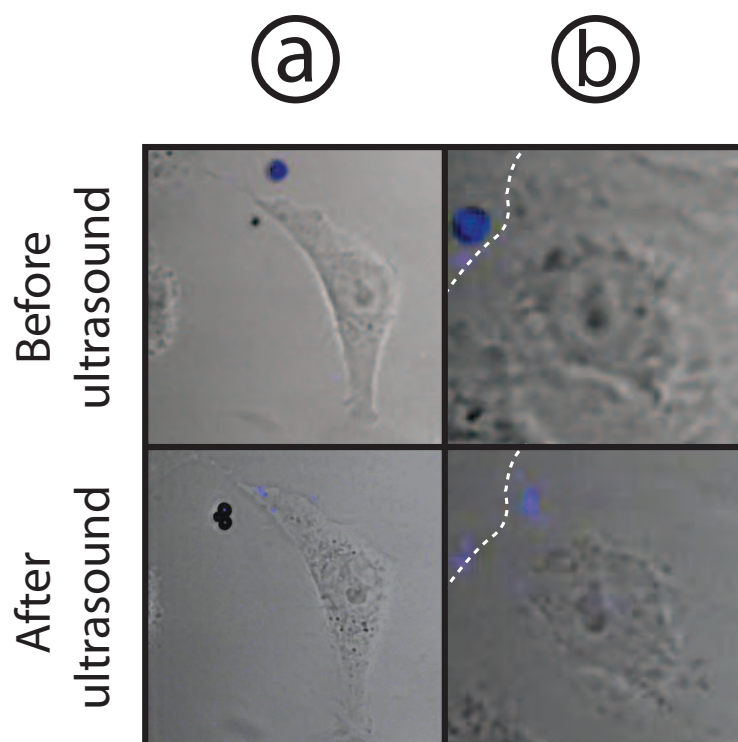


Figure 6.11: Columns (a) and (b) represent frames in optical focus from the events in Figures 6.8 and 6.9, respectively, before sonication and approximately 8 minutes after sonication. The white dotted lines in the right frames indicate the cell membrane boundary. The left frames correspond to $76 \times 76 (\mu\text{m})^2$ areas, whereas the right frames correspond to $45 \times 45 (\mu\text{m})^2$ areas.

For both events, Figure 6.10 shows average fluorescent intensities in two regions of interest, one inside the cell, and one control region. In both events, most fluorescence from apparent microbubble entry can be observed within $5 \mu\text{m}$ proximal to optical focus, thus well within the cells themselves.

Figure 6.11 shows frames in optical focus from the events in Figures 6.8 and 6.9, before sonication and approximately 8 minutes after sonication. Clearly, fluorescence has transferred into the cells and remained inside the cells long after sonication.

At these low acoustic amplitudes, inertial cavitation, fragmentation, and jetting should not occur. Hence, as a mechanism in sonoporation at low MI, these phenomena might justifiably be neglected.

Our observations do not explain why some microbubbles enter a cell and others don't. The quick dissolution after entering suggests that the microbubble loses (part of) its shell whilst entering.

The ζ -potential measurements showed that the microbubble shells had a charge of $-43.9 \pm 2.4 \text{ mV}$. As cells have a natural negative charge [33, 129], the ultrasound

contrast agent should be repelled by the cells. In all recordings it was seen that once the ultrasound was turned on, the microbubbles were attracted to the closest cell, independent of the direction of the sound field. This supports the recent finding that cell membranes can be acoustically active [68], and therefore interact with microbubbles.

Other cell types than HeLa cells must be used in follow-up studies, to investigate differences in bubble–cell interaction.

6.4 Conclusions

It has been demonstrated that lipid-shelled microbubbles can be forced to enter cells at a low MI. Hence, if a therapeutic load is added to the bubble, ultrasound-guided delivery could be facilitated at diagnostic settings.

In addition, these results may have implications for the safety regulations on the use of ultrasound contrast agents for diagnostic imaging.

7

Summary and discussion

The use of ultrasound for non-invasive diagnostics in both industry and medical imaging has proven itself to be invaluable due to its low price per examination and ease of use [19, 54, 133, 137].

In medical-diagnostics, guidelines state an $MI < 0.3$ can be considered safe for pregnant women and neonatals, but yet diagnostic imaging machines allow the use of MI up to 1.9, putting the acoustic intensity used at the examiners discretion. The current regulations are based on the likelihood of inertial cavitation. It is known that inertial cavitation can cause damage not only to cells but also to metals, such as boat propellers and car injectors [5, 38, 41, 97]. Due to technical challenges, studying the formation and interaction of ultrasound generated cavities is minimal. Therefore, current understanding of the consequences of cavitation near or inside cells is limited.

Previous studies on non-invasive, ultrasound-induced therapeutics used acoustic amplitudes corresponding to mechanical indices between 0.2 and 7.0 [9, 29, 115].

In Chapter 2 the manufacture of efficient, high-frequency, HIFU transducers, capable of high-resolution tissue ablation was analysed. It was shown that these transducers could be manufactured at low material cost ($< \pounds 25$) compared

Based on: Delalande A, Kotopoulis S, Pichon C, Postema M. Cancer cell sonoporation at low acoustic amplitudes. *Proc 18th Int Congr Sound Vibration* **2011** #4320.

This work has been supported by EPSRC Grants EP/F037025/1 and Statoil grant SH2011.

to commercial HIFU PZT transducers, yet these low-budget transducers were capable of generating acoustic amplitudes equivalent to an $MI > 3.0$. Furthermore, single-element high-frequency high-intensity transducers cost even less (<£7 in material costs) to manufacture. These transducers were capable of acoustic amplitudes equivalent to an $MI = 2.7$ at a centre transmit frequency of 6.6 MHz, and worked up to the 5th harmonic of 35 MHz, generating a sound field equivalent to an $MI = 0.4$. These transducers surpassed the safety threshold for diagnostic use even at the 5th harmonic.

In addition to being economic and time effective, these transducers were also more environmentally friendly when compared to traditional piezo-ceramics, as the piezo-electric crystal used was lead-free and did not require poling.

A limitation in the use of LiNbO_3 as a piezo-electric element is its fragility. The LiNbO_3 elements were seen to be very sensitive to stress concentrations and tended to crack when small physical loads were applied in comparison to PZT piezo-ceramics, *e.g.*, when lapping or dicing to the desired thickness or shape. This fragility was also noticed when applying a high voltage over these elements. For this reason, higher tolerances need to be used when manufacturing transducers with LiNbO_3 active elements. In addition LiNbO_3 is a very poor receiver compared to traditional PZTs due to its low d_{33} value, thus it can't be used for imaging and diagnostics.

High-frequency transducers capable of FUS would allow for smaller lesion formation which might surpass the precision of invasive surgery, whilst avoiding the risks associated with invasive surgery [47]. Affordable transducers capable of high-resolution FUS will open a whole new field in ultrasound-induced therapeutics.

Chapters 2 and 6 show that coagulative necrosis can occur in less than 90 seconds at an $MI < 2.0$ and cellular damage can occur in the presence of microbubbles at an $MI < 0.2$.

Medical ultrasound has also been of use in biological control. Chapter 3 treats the sonication of cyanobacteria using pulsed ultrasound at a low MI. The blue-green algae was seen to sink under laboratory conditions. Thus, ultrasound promotes a natural death of this species without the release of toxins.

Some cyanobacteria have been said to be harmful to humans and aquatic animals. Therefore, it would be beneficial to control their blooming. Ultrasound might be used to clean contaminated water.

Since these investigations were only performed in a laboratory setup and only on a single species, it is unlikely that a similar effect would be seen on a larger scale,

or outdoors in natural surroundings.

Similar low-MI ultrasound fields were used to study ultrasound contrast agents in artificial capillaries. Chapter 4 showed that continuous 2.2-MHz and 7.0-MHz ultrasound at an $MI < 0.015$ formed clusters of more than 2000 microbubbles at precise locations. This cluster-formation phenomenon might be used to purposely block vessels, *e.g.*, to temporarily stop blood supply to a tumour, or to gather drug-loaded microbubbles to a specific location for ultrasound-enhanced drug delivery.

The formation of such clusters only occurred at high microbubble concentrations, *i.e.*, at concentrations only theoretically feasible in the human body with undiluted bolus injections. The influence of the flow rate to cluster formation has to be investigated.

To understand the effects of high-intensity ultrasound in tissue, knowledge in acoustic cavitation needs to be improved. Acoustic cavitation typically occurs within a few acoustic cycles at unpredictable locations. To study cavitation with high-speed photography, the site of nucleation needs to be precisely known. In Chapter 5 a scientific instrument that is dedicated to this outcome, combining a focussed ultrasound transducer with a pulsed laser is described. It was demonstrated that inertial cavitation can be controllably introduced to the ultrasound focus. Acoustic cavitation was seen to occur at acoustic amplitudes equivalent to an $MI = 0.7$. At higher MI, dynamic cavitation clouds were formed. Our findings will contribute to the understanding of cavitation evolution in focussed ultrasound, including for potential therapeutic applications.

All previous sonoporation publications involved high-MI ultrasound to deliver compounds into cells. In Chapter 6 low-MI methods for drug and gene delivery was explored. Lipid-shelled microbubbles were forced into cells using pulsed ultrasound at $MI = 0.2$ at transmit frequencies of 1.0 MHz and 6.6 MHz. This phenomenon typically takes 2 s from the moment a bubble contacts the cell membrane, to complete dissolution of the gas inside the cell. Most bubble–cell penetration occurred within 8 s from the start of sonication. These results were easily reproducible, independent of the setup geometry. These are the first recorded and validated observations of entire microbubbles translating into cells. Since bubbles can be forced into cells, release mechanisms to detach drugs from microbubbles may be of lesser importance.

Targeted drug delivery down to the cellular level, with the use of encapsulated bubbles will allow the use of high-toxicity drugs to be injected into the body, but only delivered to a specific area. Thus, leaving healthy tissue unaffected.

Our sonoporation observations could be attributed to the long pulse lengths used. The bubble-cell attraction then may be attributed to secondary Bjerknes forces, similar to those described in Chapter 4. In diagnostic imaging, much shorter pulse lengths are used. Although cells themselves are acoustically active, this acoustic activity is probably negligible to that of microbubbles in high concentrations. Therefore, it is expected that bubble-cell interactions are more likely to occur in very low bubble concentrations. This type of bubble-cell attraction is less likely to occur using common clinical diagnostic equipment.

In this thesis, it has been shown that it is possible to manufacture low-cost therapeutic transducers, ultrasound can be used to kill single cells or increase drug uptake, and acoustic cavitation can be induced at precise locations.

Future work

To ensure reliable performance of LiNbO_3 transducers, several flaws must be addressed. As the Ag-paint electrodes were damaged due to heat and cavitation at the electrode–crystal interface, different electrode materials need to be investigated, *e.g.*, Cr-Au or Ti-Pt. In addition to more reliable electrode application techniques need to be explored. Sputter coating thin film electrodes should eliminate gas pockets at the electrode–crystal interface, leading to better coupling, thus less crystal heating. Other improvements include transducer designs where the natural foci of each active element could be aligned more accurately, lighter support materials, and protective outer layers

In the field of cyanobacteria eradication, other species must be examined in laboratory conditions and in their natural environments. Lower frequencies need to be investigated for outdoor eradication.

Our preliminary laser-nucleated acoustic cavitation results show the formation of cavitation clouds at high MI. Very little is known on the dynamics of cavitation clouds. Because clouds are easily induced, their role in FUS must be studied.

The viability of cells penetrated by microbubbles still needs to be assessed, and subsequently suitability of this sonoporation technique for localised drug delivery needs to be evaluated. This, of course, requires therapeutics to be incorporated in the microbubbles. Although encapsulation processes go beyond the scope of this thesis, they are essential to the future success of ultrasound-guided drug and gene delivery. If drug and genes can be successfully coupled to acoustically active vehicles, sonoporation might revolutionise non-invasive therapy as we know it.

Bibliography

- [1] Abdollahi A, Domhan S, Jenne J, Hallaj M, Dell'Aqua G, Mueckenthaler M, Richter A, Martin H, Debus J, Ansorge W, Hynynen K, Huber P. Apoptosis signals in lymphoblasts induction by focussed ultrasound. *FASEB J* **2004** 18(12):1412–1432.
- [2] Allen MB, Arnon DI. Studies on nitrogen-fixing blue-green algae. I. Growth and nitrogen fixation by *Anabaena Cylindrica* lemm. *Plant Physiol* **1955** 30(4):366–372.
- [3] Alvarez-Herrera C, Moreno-Hernández D, Barrientos-García B, Guerrero-Viramontes J. Temperature measurement of air convection using a Schlieren system. *Opt Laser Technol* **2008** 41(3):233–240.
- [4] Ashush H, Rozenszajn LA, Blass M, Barda-Saad M, Azimov D, Radnay J, Zipori D, Rosenschein U. Apoptosis induction of human myeloid leukemic cells by ultrasound exposure. *Cancer Research* **2000** 60:1014–1120.
- [5] Asi O. Failure of diesel engine injector nozzle by cavitation. *Eng Fail Anal* **2006** 13(7):1126–1133.
- [6] Bao S, Thrall BD, Miller DL. Transfection of a reporter plasmid into cultured cells by sonoporation in vitro. *Ultrasound Med Biol* **1997** 23:953–959.
- [7] Bekeredjian R, Grayburn PA, Shohet RV. Use of ultrasound contrast agents for gene or drug delivery in cardiovascular medicine. *J Am Coll Cardiol* **2005** 45(3):329–335.
- [8] Bell A. *Forced Induction Performance Tuning: A practical guide to supercharging and turbocharging*. Yeovil: Haynes **2010**.
- [9] Bigelow T, Northagen T, Hill T, Sailer F. The destruction of *Escherichia coli* biofilms using high-intensity focussed ultrasound. *Ultrasound Med Biol* **2009** 35(6):1026–1031.

- [10] Bowen C, Jensen T. Blue-green algae: Fine structure of the gas vacuoles. *Science* **1965** 147(3664):1460–1462.
- [11] Bury N. The toxicity of cyanobacteria (blue-green algae) to freshwater fish. *Comp Biochem Physiol A* **2007** 146(4):S92–S93.
- [12] Cannata J, Ritter T, Chen WH, Silverman R, Shung K. Design of efficient, broadband single-element (20–80 MHz) ultrasonic transducers for medical imaging applications. *IEEE Trans Ultrason Ferroelectr Freq Control* **2003** 50(11):1548–1557.
- [13] Caskey C, Qin S, Dayton PA, Ferrara KW. Microbubble tunneling in gel phantoms. *J Acoust Soc Am* **2009** 125(5):EL183–EL189.
- [14] Chen B, Huang J, Wang J, Huang L. Ultrasound effects on the antioxidative defense systems of porphyridium cruentum. *Colloids Surf B* **2008** 61(1):88–92.
- [15] Chen H, Li X, Wan M. Spatial-temporal dynamics of cavitation bubble clouds in 1.2 MHz focussed ultrasound field. *Ultrason Sonochem* **2006** 13:480–486.
- [16] Chen H, Xiaojing L, Wan M, Wang S. High-speed observation of cavitation bubble cloud structures in the focal region of a 1.2 MHz high-intensity focussed ultrasound transducer. *Ultrason Sonochem* **2007** 14:291–297.
- [17] Chen S, Shohet RV, Bekeredjian R, Frenkel P, Grayburn PA. Optimization of ultrasound parameters for cardiac gene delivery of adenoviral or plasmid deoxyribonucleic acid by ultrasound-targeted microbubble destruction. *J Am Coll Cardiol* **2003** 42(2):301–308.
- [18] Conway J. A vascular abnormality in hypertension. *Circulation* **1963** 27:520–529.
- [19] Courtney C, Drinkwater B, Neild S, Wilcox P. Factors affecting the ultrasonic intermodulation crack detection technique using bispectral analysis. *NDT & E Int* **2008** 41:223–234.
- [20] Coussios C, Farny C, ter Haar G, Roy R. Role of acoustic cavitation in the delivery and monitoring of cancer treatment by high-intensity focussed ultrasound (HIFU). *Int J Hyperthermia* **2007** 23(2):105–120.

- [21] Crum LA Bjerknes forces on bubbles in a stationary sound field. *J. Acoust. Soc. Am.* **1975** 57(6):1363–1370.
- [22] Culture Collection of Algae and Protozoa. *Media Recipes*, volume EG:JM **2007**.
- [23] Dauta A, Devaux J, Piquemal F, Bouminch L. Growth rate of four freshwater algae in relation to light and temperature. *Hydrobiologia* **1990** 207(1):221–226.
- [24] Dayton PA, Allen JS, Ferrara KW. The magnitude of radiation force on ultrasound contrast agents. *J Acoust Soc Am* **2002** 112(5):2183–2192.
- [25] Dayton PA, Morgan KE, Klivanov AL, Brandenburger G, Nightingale KR, Ferrara KW. A preliminary evaluation of the effects of primary and secondary radiation forces on acoustic contrast agents. *IEEE Trans Ultrason Ferroelectr Freq Control* **1997** 44(6):1264–1277.
- [26] Deane C, Lees C. Doppler obstetric ultrasound: a graphical display of temporal changes in safter indicies. *Ultrasound Obstet Gynecol* **2000** 15:418–423.
- [27] Delalande A, Bureau MF, Midoux P, Bouakaz A, Pichon C. Ultrasound-assisted microbubbles gene transfer in tendons for gene therapy. *Ultrasonics* **2009** 50:269–272.
- [28] Deng CX, Lizzi FL. A review of physical phenomena associated with ultrasonic contrast agents and illustrative clinical applications. *Ultrasound Med Biol* **2002** 28(3):277–286.
- [29] Deng CX, Pan S, Cui J. Ultrasound-induced cell membrane porosity. *Ultrasound Med Biol* **2004** 30:519–526.
- [30] Detre J, Leigh J, Williams D, Koretsky A. Perfusion imaging. *Magn Res Med* **1992** 23(1):37–45.
- [31] Di Marco P, Grassi W, Memoli G. Experimental study on rising velocity of nitrogen bubbles in FC-72. *Int J Therm Sci* **2003** 42:435–446.
- [32] Duineveld PC. Bouncing and coalescence phenomena of two bubbles in water. In: Blake JR, Boulton-Stone JM, Thomas NH, Eds. *Bubble Dynamics and Interface Phenomena*. Dordrecht: Kluwer **1994** 447–456.

- [33] Ehrenberg B, Montana V, Wei MD, Wuskell J, Loew L. Membrane potential can be determined in individual cells from the nernstain distribution of cationic dyes. *Biophys J* **1988** 53:785–794.
- [34] Feril Jr L, Kondo T, Takaya K, Riesz P. Enhanced ultrasound-induced apoptosis and cell lysis by a hypotonic medium. *Int J Radiat Biol* **2004** 80(2):165–175.
- [35] Ferrier MD, Butler Sr BR, Terlizzi DE, Lacouture RV. The effects of barley straw (*hordeum vulgare*) on the growth of freshwater algae. *Biores Tech* **2005** 96(16):1788–1795.
- [36] Fleming LE, Rivero C, Burns J, Williams C, Bean JA, Shea KA, Stinn J. Blue green algal (cyanobacterial) toxins, surface drinking water, and liver cancer in Florida. *Harmful Algae* **2002** 1(2):157–168.
- [37] Fowlkes J, Carson P. Systems for degassing water used in ultrasonic measurements. *J Acoust Soc Am* **1991** 90(2):1197–1200.
- [38] Fuciarelli A, Sisk E, Thomas R, Miller D. Induction of base damage in DNA solutions by ultrasonic cavitation. *Free Radic Biol Med* **1995** 18(2):231–238.
- [39] Fujimoto J, Lin W, Ippen E, Puliafito C, Steinert R. Time-resolved studies of Nd:YAG laser-induced breakdown. Plasma formation, acoustic wave generation, and cavitation. *Invest Ophthalmol Vis Sci* **1985** 26(12):1771–1777.
- [40] Gerold B, Reynolds S, Melzer A, Cochran S. Early exploration of MRI-compatible diagnostic ultrasound transducers. *Proc IEEE Ultrason Symp* **2010** accepted.
- [41] Gerr D, Ed. *The Propeller Handbook: The complete reference for choosing, installing, and understanding boat propellers*. Maidenhead: McGraw-Hill **2001**.
- [42] Gorce JM, Arditi M, Schneider M. Influence of bubble size distribution on the echogenicity of ultrasound contrast agents: a study of SonoVue™. *Invest Radiol* **2000** 35(11):661–671.
- [43] Greenleaf WJ, Bolander ME, Sarkar G, Goldring MB, Greenleaf JF. Artificial cavitation nuclei significantly enhance acoustically induced cell transfection. *Ultrasound Med Biol* **1998** 24(4):587–595.

- [44] Gregersen E, Ed. *The Britannica Guide to Sound and Light*. New York: The Rosen Publishing Group **2011**.
- [45] ter Haar G. Safety and bio-effects of ultrasound contrast agents. *Med Biol Eng Comput* **2009** 47:893–900.
- [46] ter Haar GR. Ultrasound focal beam surgery. *Ultrasound Med Biol* **1995** 21:1089–1100.
- [47] Hakim N, Papalois V. *Surgical Complications: Diagnostics and Treatment*. London: Imperial College Press **2007**.
- [48] Hallow D, Mahajan A, McCutchen T, Prausnitz M. Measurement and correlation of acoustic cavitation with cellular bioeffects. *Ultrasound Med Biol* **2006** 32(7):1111–1122.
- [49] Hao H, Wu M, Chen Y, Tang J, Wu Q. Cavitation mechanism in cyanobacterial growth inhibition by ultrasonic irradiation. *Colloids Surf B* **2004** 33(3–4):151–156.
- [50] Hentschel W, Lauterborn W. Acoustic-emission of single laser-produced cavitation bubbles and their dynamics. *Appl Sci Res* **1982** 38:225–230.
- [51] Heymsfield S. *Human Body Composition*. Champaign: Human Kinetics **2005**.
- [52] Hill C, ter Haar GR. High intensity focussed ultrasound: potential for cancer treatment. *Brit J Radiol* **1995** 68:1296–1303.
- [53] Holt R, Roy R. Measurements of bubble-enhanced heating from focussed, MHz-frequency ultrasound in a tissue-mimicking material. *Ultrasound Med Biol* **2001** 27(10):1399–1412.
- [54] Houze M, Nonailard B, Gazalet M, Rouvaen J, Bruneel C. Measurement of the thickness of thin layers by ultrasonic interferometry. *J Appl Phys* **1984** 55(1):194–198.
- [55] Huston T, Simmons R. Ablative therapies for the treatment of malignant diseases of the breast. *Am J Surg* **2005** 189(6):694–701.
- [56] Hylland K, Sköld M, Gunnarsson JS, Skei J. Interactions between eutrophication and contaminants. IV. Effects on sediment-dwelling organisms. *Mar Poll Bull* **1996** 33(1–6):90–99.

- [57] Hynynen K. MRI-guided focussed ultrasound treatments. *Ultrasonics* **2010** 50(2):221–229.
- [58] de Jong N, Cornet R, Lancée CT. Higher harmonics of vibrating gas-filled microspheres. Part one: simulations. *Ultrasonics* **1994** 32(6):447–453.
- [59] Kaddur K, Lebegue L, Tranquart F, Midoux P, Pichon C, Bouakaz A. Transient transmembrane release of green fluorescent proteins with sonoporation. *IEEE Trans Ultrason Ferroelectr Freq Control* **2010** 57(7):1558–1567.
- [60] Karshafian R, Samac S, Banerjee M, Bevan PD, Burns PN. Ultrasound-induced uptake of different size markers in mammalian cells. *Proc IEEE Ultrason Symp* **2005** 13–16.
- [61] Kimmel E, Krasovitski B, Hoogi A, Razansky D, Adam D. Subharmonic response of encapsulated microbubbles: condition for existence and amplification. *Ultrasound Med Biol* **2007** 33(11):1767–1776.
- [62] Klibanov AL. Targeted delivery of gas-filled microspheres, contrast agents for ultrasound imaging. *Adv Drug Deliv Rev* **1999** 37:139–157.
- [63] Kodama T, Takayama K. Dynamic behavior of bubbles during extracorporeal shock-wave lithotripsy. *Ultrasound Med Biol* **1998** 24(5):723–738.
- [64] Kondo I, Ohmori K, Oshita A, Takeuchi H, Fuke S, Shinomiya K, Noma T, Namba T, Kohno M. Treatment of acute myocardial infarction by hepatocyte growth factor gene transfer: the first demonstration of myocardial transfer of a “functional” gene using ultrasonic microbubble destruction. *J Am Coll Cardiol* **2004** 44(3):644–653.
- [65] Kooiman K, Böhmer M, Emmer M, Vos H, Chlon C, Foppen-Harteveld M, Versluis M, de Jong N, van Wamel A. Ultrasound-triggered local release of lipophilic drugs from a novel polymeric ultrasound contrast agent. *J Control Release* **2008** 132(3):e41–e42.
- [66] Kotopoulis S, Postema M. Microfoam formation in a capillary. *Ultrasonics* **2010** 50(2):260–268.
- [67] Kotopoulis S, Wang H, Cochran S, Postema M. Lithium niobate ultrasound transducers for high-resolution focussed ultrasound surgery. *Proc IEEE Ultrason Symp* **2010** accepted.

- [68] Krasovitski B, Frenkel V, Shoham S, Kimmel E. Subcellular sonophores: ultrasound induced intramembrane cavitation. *Proc Nat Acad Sci* **2011** 108(8):3258–3263.
- [69] Kudo N, Miyaoka T, Kuribayashi K, Yamamoto K. Study of the mechanism of fragmentation of a microbubble exposed to ultrasound using a high-speed observation system. *J Acoust Soc Am* **2000** 108(5Pt2):2547.
- [70] Kudo N, Okada K, Yamamoto K. Sonoporation by single-shot pulsed ultrasound with microbubbles adjacent to cells. *Biophys J* **2009** 96(12):4866–4876.
- [71] Kurz T, Kröninger D, Geisler R, Lauterborn W. Optic cavitation in an ultrasonic field. *Phys Rev E* **2006** 74(6):066 307.
- [72] Kuttruff H. *Acoustics: An introduction*. London: Taylor & Francis **2007**.
- [73] Lang N, Krupp J, Koller A. Morphological and ultrastructural changes in vegetative cells and heterocysts of *Anabaena Variabilis* grown with fructose. *J Bacteriol* **1987** 169(2):920–923.
- [74] Lauterborn W, Kurz T. Physics of bubble oscillations. *Rep Prog Phys* **2010** 73:106501.
- [75] Leighton T. Bubble population phenomena in acoustic cavitation. *Ultrason Sonochem* **1995** 2(2):S123–S136.
- [76] Leighton TG. *The Acoustic Bubble*. London: Academic Press **1994**.
- [77] Lindner J, Kaul S. Delivery of drugs with ultrasound. *Echocardiography* **2001** 18(4):329–337.
- [78] Livanec P, Dunn R. Single-molecule probes of lipid membrane structure. *Langmuir* **2008** 24(24):14 066–14 073.
- [79] Lockwood G, Ryan L, Hunt J, Foster F. Measurement of the ultrasonic properties of vascular tissues and blood from 35–65 MHz. *Ultrasound Med Biol* **1991** 17(7):653–666.
- [80] Lyons M, Parker J. Absorbtion and attenuation in soft tissues ii– experimental results. *IEEE Trans Ultrason Ferroelectr Freq Control* **1988** 35(4):511–521.

- [81] Ma B, Chen Y, Hao H, Wu M, Wang B, Lv H, Zhang G. Influence of ultrasonic field on Microcystins produced by bloom-forming algae. *Colloids Surf B* **2005** 41(2–3):197–201.
- [82] Marmottant P, Hilgenfeldt S. Controlled vesicle deformation and lysis by single oscillating bubbles. *Nature* **2003** 423:153–156.
- [83] Mateos-Naranjo E, Redondo-Gómez S, Cambrollé J, Enrique Figueroa M. Growth and photosynthetic responses to copper stress of an invasive cordgrass, *spartina densiflora*. *Marine Environ Res* **2008** 66(4):459–465.
- [84] Medwin H. Counting bubbles acoustically: a review. *Ultrasonics* **1977** 15:7–13.
- [85] Mettin R, Akhatov I, Parlitz U, Ohl CD, Lauterborn W. Bjerknes forces between small cavitation bubbles in a strong acoustic field. *Phys Rev E* **1997** 56(3):2924–2931.
- [86] Miller DL, Dou C, Song J. DNA transfer and cell killing in epidermoid cells by diagnostic ultrasound activation of contrast agent gas bodies in vitro. *Ultrasound Med Biol* **2003** 29(4):601–607.
- [87] Miller M, Miller D, Brayman AA. A review of *in vitro* bioeffects of inertial ultrasonic cavitation from a mechanistic perspective. *Ultrasound Med Biol* **1996** 22(9):1131–1154.
- [88] Morris P, Hurell A, Shaw A, Zhang E, Beard P. A Fabry-Pérot fiber-optic ultrasonic hydrophone for the simultaneous measurement of temperature and acoustic pressure. *J Acoust Soc Am* **2009** 125(6):3611–3622.
- [89] Nakazawa M, Kosugi T, Nakamura K, Ueha S, Maezawa A, Hirao Y. A high frequency variable focus ultrasonic transducer using polyurea thin film. *Proc IEEE Ultrason Symp* **2005** 4:2313–2316.
- [90] National Council on Radiation Protection & Measurements. *Exposure Criteria for Medical Diagnostic Ultrasound* **2002**.
- [91] NATO Undersea Research Centre. Human diver and marine mammal risk mitigation rules and procedures. Technical report, NURC-SP-2006-008 **2006**.
- [92] Neuhoff J, Ed. *Ecological Psychoacoustics*. London: Elsevier **2004**.

- [93] Neumann T, Ermert H. Schlieren visualization of ultrasonic wave fields with high spatial resolution. *Ultrasonics* **2006** 44(1):e1561–e1566.
- [94] Ng K. International guidelines and regulations for the safe use of diagnostic ultrasound in medicine. *J Med Ultrasound* **2002** 10:5–9.
- [95] Ohl C, Wolfrum B. Detachment and sonoporation of adherent HeLa-cells by shock wave-induced cavitation. *Biochim Biophys Acta* **2003** 1624(1-3):131–138.
- [96] Ohl CD, Ory E. Aspherical bubble collapse — comparison with simulations. In: Lauterborn W, Kurz T. Eds. *Nonlinear Acoustics at the Turn of the Millennium*. New York: American Institute of Physics **2000** 393–396.
- [97] Palanker D, Vankov A, Miller J, Friedman M, Strauss M. Prevention of tissue damage by water jet during cavitation. *J Appl Phys* **2003** 94(4):2654–2661.
- [98] Philipp A, Lauterborn W. Cavitation erosion by single laser-produced bubbles. *J Fluid Mech* **1998** 361:75–116.
- [99] Postema M. Onderzoek naar de veilige toepassing van ultrageluid gebruikt om blauwalg te bestrijden. Memo, The University of Hull **2007**.
- [100] Postema M, Bouakaz A, ten Cate F, Schmitz G, de Jong N, van Wamel A. Nitric oxide delivery by ultrasonic cracking: some limitations. *Ultrasonics* **2006** 44(S1):e109–e113.
- [101] Postema M, Bouakaz A, Chin CT, de Jong N. Simulations and measurements of optical images of insonified ultrasound contrast microbubbles. *IEEE Trans Ultrason Ferroelectr Freq Control* **2003** 50(5):523–536.
- [102] Postema M, Bouakaz A, Versluis M, de Jong N. Ultrasound-induced gas release from contrast agent microbubbles. *IEEE Trans Ultrason Ferroelectr Freq Control* **2005** 52(6):1035–1041.
- [103] Postema M, ten Cate FJ, Schmitz G, de Jong N, van Wamel A. Generation of a droplet inside a microbubble with the aid of an ultrasound contrast agent: first result. *Lett Drug Des Discov* **2007** 4(1):74–77.
- [104] Postema M, Gilja OH. Ultrasound-directed drug delivery. *Curr Pharm Biotechnol* **2007** 8(6):355–361.

- [105] Postema M, Gilja OH. Jetting does not cause sonoporation. *Biomed Eng* **2010** 55:S19–S20.
- [106] Postema M, Gilja OH. Contrast-enhanced and targeted ultrasound. *World J Gastroenterol* **2011** 17(1):28–41.
- [107] Postema M, Gilja OH, van Wamel A. CEUS and sonoporation. In: Postema M. *Fundamentals of Medical Ultrasonics*. London: Spon press **2011** 205–217.
- [108] Postema M, Marmottant P, Lancée CT, Hilgenfeldt S, de Jong N. Ultrasound-induced microbubble coalescence. *Ultrasound Med Biol* **2004** 30(10):1337–1344.
- [109] Postema M, Mleczko M, Schmitz G. Mutual attraction of oscillating microbubbles. In: Buzug TM, Holz D, Weber S, Bongartz J, Kohl-Bareis M, Hartmann U. Eds. *Advances in Medical Engineering*, volume 19 of *Methods of experimental physics*. Berlin: Springer **2007** 75–80.
- [110] Postema M, Schmitz G. Bubble dynamics involved in ultrasonic imaging. *Expert Rev Mol Diagn* **2006** 6(3):493–502.
- [111] Postema M, Schmitz G. Ultrasonic bubbles in medicine: influence of the shell. *Ultrason Sonochem* **2007** 14(4):438–444.
- [112] Postema M, van Wamel A, ten Cate FJ, de Jong N. High-speed photography during ultrasound illustrates potential therapeutic applications of microbubbles. *Med Phys* **2005** 32(12):3707–3711.
- [113] Postema M, van Wamel A, Lancée CT, de Jong N. Ultrasound-induced encapsulated microbubble phenomena. *Ultrasound Med Biol* **2004** 30(6):827–840.
- [114] Prentice P, Cuschieri A, Dholakia K, Prausnitz M, Campbell P. Membrane disruption by optically controlled microbubble cavitation. *Nature Phys* **2005** 1:107–110.
- [115] Pua E, Zhong P. Ultrasound-mediated drug delivery. *IEEE Eng Med Biol* **2009** 28(1):64–75.
- [116] de la Rosette JJMCH, Mouraviev V, Polascik T. Focal targeted therapy will be a future treatment modality for early stage prostate cancer. *Eur Urol Suppl* **2009** 8(5):424–432.

- [117] Rouvière O, Mège-Lechevallier F, Chapelon JY, Gelet A, Bouvier R, Boutille F, Lyonnet D. Evaluation of color doppler in guiding prostate biopsy after HIFU ablation. *Eur Urol* **2006** 50(3):490–497.
- [118] San Diego-McGlone ML, Azanza RV, Villanoy CL, Jacinto GS. Eutrophic waters, algal bloom and fish kill in fish farming areas in Bolinao, Pangasinan, Philippines. *Mar Poll Bull* **2008** 57(6–12):295–301.
- [119] Sboros V. Response of contrast agent to ultrasound. *Adv Drug Deliv Rev* **2008** 60:1117–1136.
- [120] Schiener E, Freeman J, Abramowicz J. Acoustic output as measured by mechanical and thermal indices during routine obstetric ultrasound examinations. *J Ultrasound Med* **2005** 24(1665-1670).
- [121] Schmerr L, Lopez-Sanchez A, Huang R. Complete ultrasonic transducer characterization and its use for models and measurements. *Ultrasonics* **2006** 44(1):e753–e757.
- [122] Shaw A, ter Haar GR. Requirements for measurements standards in high intensity focussed ultrasound (HIFU) fields. Technical Report DQL AC 015, National Physical Laboratory **2006**.
- [123] Shortencarier MJ, Dayton PA, Bloch SH, Schumann PA, Matsunaga TO, Ferrara KW. A method for radiation-force localized drug delivery using gas-filled lipospheres. *IEEE Trans Ultrason Ferroelectr Freq Control* **2004** 51(7):822–831.
- [124] Snook K, Zhao JZ, Alves C, Cannata J, Chen WH, Meyer R, Ritter T, Shung K. Design, fabrication, and evaluation of high frequency, single-element transducers incorporating different materials. *IEEE Trans Ultrason Ferroelectr Freq Control* **2002** 49(2):169–176.
- [125] Stewart I, Schluter PJ, Shaw GR. Cyanobacterial lipopolysaccharides and human health: a review. *Environ Health* **2006** 5(7):1–23.
- [126] Stride E, Saffari N. Microbubble ultrasound contrast agents: a review. *Proc Inst Mech Eng H J Eng Med* **2003** 217:429–447.
- [127] Tachibana K, Tachibana S. Albumin microbubble echo-contrast material as an enhancer for ultrasound accelerated thrombolysis. *Circulation* **1995** 92(5):1148–1150.

- [128] Tachibana K, Uchida T, Ogawa K, Yamashita N, Tamura K. Induction of cell-membrane porosity by ultrasound. *Lancet* **1999** 353:1409.
- [129] Takahashi A, Yamaguchi H, Miyamoto H. Change in K⁺ current of HeLa cells with progression of the cell cycle studied by patch-clamp technique. *Am J Physiol* **1993** 265(2):C328–C336.
- [130] Takeshi Y, Toshinobu U, Kitayama T. Piezoelectricity of a high-content lead zirconate titanate/polymer composite. *J Appl Phys* **1982** 53(6):4328–4332.
- [131] Tang J, Wu Q, Hao H, Chen Y, Wu M. Growth inhibition of the cyanobacterium spirulina (arthrospira) platensis by 1.7 MHz ultrasonic irradiation. *J Appl Phycol* **2003** 15(1):37–43.
- [132] Tinkov S, Bekeredjian R, Winter G, Coester C. Microbubbles as ultrasound triggered drug carriers. *J Pharm Sci* **2009** 98(6):1935–1961.
- [133] Tiu CM, Chou YH, Chen JD, Chiou YY, Chiou SY, Wang HK, Chen SP, Wei CF, Chin TW. Ultrasound diagnosis of acute appendicitis: impact on cost and outcome in pediatric patients. *J Med Ultrasound* **2004** 12(3):69–74.
- [134] Tortoli P, Michelassi V, Corsi M, Righi D, Takeuchi Y. On the interaction between ultrasound and contrast agents during Doppler investigations. *Ultrasound Med Biol* **2001** 27(9):1265–1273.
- [135] Turner PC, Gammie AJ, Hollinrake K, Codd GA. Pneumonia associated with contact with cyanobacteria. *Br Med J* **1990** 300:1440–1441.
- [136] Unger EC, Matsunaga TO, McCreery T, Schumann P, Sweitzer R, Quigley R. Therapeutic applications of microbubbles. *Eur J Radiol* **2002** 42:160–168.
- [137] Vachhani M, Hamer F, Clarke F. Cost effectiveness of ultrasound scan by middle grade doctors in Gynae Assessment Unit (GAU). *Int J Gynecol Obstet* **2009** 107(2):S470.
- [138] Ventrella A, Catucci L, Agostiano A. Effect of aggregation state, temperature and phospholipids on photobleaching of photosynthetic pigments in spinach photosystem: ii- core complexes. *Bioelectrochemistry* **2008** 73(1):43–48.
- [139] Voigt JU. Ultrasound molecular imaging. *Methods* **2009** 48:92–97.
- [140] van Wamel A, Bouakaz A, ten Cate F, de Jong N. Effects of diagnostic ultrasound parameters on molecular uptake and cell viability. *Proc IEEE Ultrason Symp* **2002** 1387–1390.

- [141] van Wamel A, Kooiman K, Hartevelde M, Emmer M, ten Cate FJ, Versluis M, de Jong N. Vibrating microbubbles poking individual cells: drug transfer into cells via sonoporation. *J Control Release* **2006** 112(2):149–155.
- [142] Warner AW, Onoe M, Coquin G. Determination of elastic and piezoelectric constants for crystals in class (3m). *J Acoust Soc Am* **1968** 42(6):1223–1231.
- [143] Weber JC, Navarra G, Jiao L, Nicholls J, Jensen S, Habib N. New technique for liver resection using heat coagulative necrosis. *Ann Surg* **2002** 236(5):560–563.
- [144] Weis R, Gaylord T. Lithium niobate: Summary of physical properties and crystal structure. *Appl Phys A* **1985** 37:191–203.
- [145] White W, Makin I, Barthe P, Slayton M, Gliklich R. Selective creation of thermal injury zone in the superficial musculoaponeurotic system using intense ultrasound therapy. *Arch Facial Plast Surg* **2007** 9:22–29.
- [146] Willinsky R, Taylor S, ter Brugge K, Farb R, Tomlinson G, Montanera W. Neurological complications of cerebral angiography: Prospective analysis of 2,899 procedures and review of the literature. *Neuroradiology* **2003** 227(2):522–528.
- [147] Wu J, Nyborg W. Eds. *Emerging Therapeutic Ultrasound*. Hackensack: World Scientific **2006**.
- [148] Young FR. *Cavitation*. Maidenhead: McGraw-Hill **1989**.
- [149] Zhang G, Zhang P, Fan M. Ultrasound-enhanced coagulation for Microcystis Aeruginosa removal. *Ultrason Sonochem* **2009** 16(3):334–338.
- [150] Zhang G, Zhang P, Liu H, Wang B. Ultrasonic damages on cyanobacterial photosynthesis. *Ultrason Sonochem* **2006** 13(6):501–505.
- [151] Zhang G, Zhang P, Wang B, Liu H. Ultrasonic frequency effects on the removal of Microcystis Aeruginosa. *Ultrason Sonochem* **2006** 13(5):446–450.

List of Figures

1.1	Typical applications of electromagnetic (top) and acoustic (bottom) frequencies.	12
1.2	Guidelines for the safe use of biomedical sound.	16
2.1	Transducer manufacturing: ① position of plates in single wafer used for each transducer, ② dimensions of plates for each transducer, ③ computer-aided design representation of transducers, and ④ completed transducers.	21
2.2	① MRI side view of sonication setup where brightness indicates water content. Image is rotated 90° anticlockwise from true position. ② Schematic representation of sonication setup ③ perspex water bath, ④ xDucer 3, ⑤ water, ⑥ DQA gel phantom. The transducer generates negligible artefacts in the MRI image. The minor artefacts generated by the silver paint and coaxial cable are not in the acoustic path thus do not affect the image or temperature measurement.	26
2.3	Resonance frequency and third harmonic as a function of element thickness for single element LiNbO ₃ microballoon backed transducers. The diamonds indicate the Z-cut LiNbO ₃ simulations, the circles indicated the experimental measurements and the five-point stars indicate the Y-36° LiNbO ₃ cut simulations. The grey data points show the 3 rd harmonic.	27
2.4	Acoustic power as a function of transducer input voltage for 17×17 (mm) ² single element LiNbO ₃ transducers.	27
2.5	Minimum impedance magnitude and equivalent phase as a function of element thickness for single-element LiNbO ₃ microballoon-epoxy backed transducers. The black diamonds indicate the impedance magnitude whereas the grey circles indicate the phase.	29

2.6	Electrical impedance of xDucer 3 device in the frequency range from 1–60 MHz plotted on a Smith chart.	30
2.7	MRI view of sonication area. The focal region had a size of $2.5 \times 3.4 \text{ (mm)}^2$. The orange cross indicates the temperature measurement marker. The green areas represent pixels of equal temperature, the blue areas represent the acoustic field, whereas the red areas represent pixels of temperature $> 70^\circ\text{C}$	31
2.8	Temperature increase was a function of time for xDucer 3 at the acoustic focus in ultrasonic phantom measured using MRI. The black diamonds indicate the temperature of the selected pixel, whereas the grey circles indicate average temperature of the eight surrounding pixels.	32
2.9	MRI view of sonication setup using xDucer 3. During sonication at certain frequencies artefacts are generated with MRI. The blue area represents the acoustic field.	32
2.10	Photographs showing lesions formed on chicken tissue using xDucer 3. (a) lesion formed after 30 s sonication with the acoustic focus on tissue surface, (b) lesion formed after 90 s sonication with the acoustic focus beneath tissue surface. The lesion was formed 6 mm beneath the tissue surface.	33
2.11	Lesion size on chicken breast surface as a function of sonication time using xDucer 3 set at 8-W acoustic power output.	34
3.1	Nitrogen-fixating body in <i>Anabaena sphaerica</i> algae. Under fluorescent light the body does not illuminate red, proving there is no chlorophyll in the body. Each frame corresponds to $565 \times 565 \mu\text{m}^2$	37
3.2	(a) 2.2-MHz ultrasound transducer with $d = 1''$ diameter and $r_a = 35 \text{ mm}$ acoustic lens. (b) 200-kHz ultrasound transducer with $h_{\text{PG}} = 10 \text{ mm}$ matching layer.	38
3.3	Experimental setup: (a) white paper sheet; (b) control sample; (c) clamp stand; (d) transducer; (e) sonicated sample; (f) pulser-receiver. Areas A1–B2 represent brightness measurement areas, C1 represents the calibration area.	39
3.4	Schematic showing use of microscope. A $10\times$ objective lens was used. (a) Blue-green algae under tungsten lighting; (b) Blue-green algae under fluorescent lighting.	40

3.5	Microscopic image sequence showing the effect of 200 kHz–2.2 MHz ultrasound on the floating bodies of blue-green algae. Each frame corresponds to $565 \times 565 \mu\text{m}^2$	42
3.6	Water brightness as a function of ultrasonic exposure time for samples containing floating blue-green algae or sunken blue-green algae.	43
3.7	Microscopic image sequence showing the effect of 200 kHz–2.2 MHz ultrasound on sunken blue-green algae. Each frame corresponds to $565 \times 565 \mu\text{m}^2$	44
3.8	Water clarity 30 days after sonication.	45
4.1	Collision times of individual encapsulated microbubbles as a function of driving frequency at given distances d_0 , using $p_a=20 \text{ kPa}$, $R_0=1.25 \mu\text{m}$, $\kappa=5 \times 10^{-6} \text{ m}^2 \text{ N}^{-1}$ and $\rho=998 \text{ kg m}^{-3}$	49
4.2	Schematic overview of the experimental setup.	53
4.3	Close-up of the sonication tank with coinciding sound, light beam, and objective focus (top) and definitions of the azimuth and elevation of the transducer relative to the North of the container (bottom).	53
4.4	Microfoam formation during continuous sonication at 2 MHz and 20-kPa peak-negative acoustic pressure. Each frame corresponds to a $120 \times 120 (\mu\text{m})^2$ area. Time $t = 0$ was defined by the start of the sonication.	56
4.5	Cluster positions as a function of time, during continuous sonication at 2 MHz and 20-kPa peak-negative acoustic pressure. Position in the capillary is defined from East ($0 \mu\text{m}$) to West ($500 \mu\text{m}$). Bold lines indicate merged clusters. The beginning (left) of a line indicated the formation of a cluster of diameter $>6.8 \mu\text{m}$. The end (right) of a line indicates the disintegration or contraction of a cluster to a diameter $<6.8 \mu\text{m}$	57
4.6	Cluster positions as a function of time, during continuous sonication at 7 MHz and 22 kPa peak-negative acoustic pressure. Position in the capillary is defined from East ($0 \mu\text{m}$) to West ($500 \mu\text{m}$). Bold lines indicate merged clusters. The beginning (left) of a line indicated the formation of a cluster of diameter $>6.8 \mu\text{m}$. The end (right) of a line indicates the disintegration or contraction of a cluster to a diameter $<6.8 \mu\text{m}$	58

4.7	Two clusters, with 22- μm diameters and an initial distance of 55- μm , colliding and merging during continuous sonication at a 2-MHz driving frequency and a 20-kPa peak-negative pressure. The frame size corresponds to $81 \times 81 (\mu\text{m})^2$. Times are relative to the start of the sonication ($t = 0$).	59
4.8	Clusters forming during sonication at 7 MHz and 22 kPa peak-negative pressure. The frame size corresponds to $560 \times 264 (\mu\text{m})^2$. Time $t = 0$ was defined by the start of the sonication.	60
4.9	Morphing microfoam during sonication at 7 MHz and 86 kPa peak-negative pressure, and a schematic representation of the event. The frame size corresponds to $274 \times 198 (\mu\text{m})^2$. Time $t = 0$ was defined by the start of the sonication.	61
4.10	Morphing microfoam during sonication at 7 MHz and 86 kPa peak-negative pressure, and a schematic representation of the event. The frame size corresponds to $274 \times 198 (\mu\text{m})^2$. Time $t = 0$ was defined by the start of the sonication.	62
4.11	Schematic representation of the four stages of microfoam formation in a capillary: (left-right) random bubble distribution before ultrasound arrival, bubbles colliding during sonication, cluster mergence within the space of a quarter of the wavelength, microfoam translation.	63
5.1	Schematic overview of apparatus, including BNC trigger lines and ultrasound electronics.	68
5.2	Representation of the custom-made sonoptic chamber, constructed according to the dimensions of the focussed ultrasound field. The Shimadzu HPV-1 high-speed camera is depicted. Inset top right is the Schlieren imaging arrangement for alignment of the ultrasonic and optical foci. Inset bottom right is a close up of the cavitation chamber which contains the ultrasound (blue) and laser (green) foci.	69
5.3	Ⓐ Scanned axial and transverse pressure fields of the focussed bowl transducer used as the ultrasound source throughout the experiments, recorded in an ultrasound scanning tank. Ⓞ Simulation of field based on the dimensions of the transducer.	70
5.4	Cubic interpolation of the 2-dimensional scans, with sample pressure data measured in the acoustic focus within the sonoptic chamber (black dots), demonstrating ultrasound propagation.	71

- 5.5 ① Schlieren image of cavitation chamber, used to align the laser focus (green spot) to that of the ultrasound (lighter blue region). The omnidirectional needle hydrophone used to record acoustical emissions during cavitation activity is also visible. ② Fourier spectra of sound field where ① MI = 0.6 and ② MI = 5.5. 72
- 5.6 Cavitation recorded with the HPV-1 high-speed camera at 0.5 Mfps, with simultaneous imaging and focussing the laser pulse through the 50× objective lens. ① Laser-induced cavitation from a 1.2-mJ laser pulse. ② Laser-induced cavitation in a pre-established focussed ultrasound field of 1.47 MHz and MI=1.1. Each frame corresponds to a $248 \times 248 (\mu\text{m})^2$ area. 75
- 5.7 ① Laser-nucleated acoustic cavitation recorded with the Shimadzu HPV-1 camera at 0.5 Mfps, with simultaneous imaging and focussing the laser pulse through the 50× objective lens. A 0.95 mJ laser pulse was focussed into the focal volume of the ultrasound field, of identical parameters to that of Figure 5.6②. Each frame corresponds to a $248 \times 248 (\mu\text{m})^2$ area. ② Laser-nucleated cavitation in a field of higher MI=3.4, recorded with the Cordin 550-62 high-speed camera, at 0.5 Mfps. For this sequence, imaging was performed through the 5× objective, in the orthogonal configuration described in Section 5.3, to achieve a larger field-of-view of $672 \times 672 (\mu\text{m})^2$. The laser pulse was focussed through the 50× objective. 76
- 5.8 ① The acoustic signal recorded from the hydrophone positioned within the cavitation chamber, as depicted in Figure 5.5, notch-filtered at 1.47 MHz, recorded during the high-speed images of laser-nucleated cavitation depicted in Figure 5.7②. ① The spectra of the first 120 μs of the signal and ② the remaining 280 μs , during laser-nucleated acoustic cavitation. 78
- 6.1 Possible mechanisms of sonoporation: ① push, ② pull, ③ jetting, ④ shear, ⑤ translation. Based on Figure 9.2 in Postema *et al.* [107]. 84
- 6.2 Experimental setup (*top*) and a close-up of the sonoporation configuration (*bottom*). 85
- 6.3 Experimental setup (*top*) and a close-up of the fluorescence configuration (*bottom*). 87
- 6.4 Schematic representation of DiD (DiI_{C₁₈(5)}) lipophilic fluorescent probe bonding to phospholipids [78]. 89

- 6.5 z -stacks of fluorescence emitted by the DiD dye attached to the membranes of four typical HeLa cells, representing the cell geometry. 89
- 6.6 z -stack of two ultrasound contrast agent microbubbles. Proximal-to-focus Airy disks can be seen around the bubbles, whereas distal-to-focus the bubble boundaries are blurred. Microbubble “A” has a diameter of 2 μm , whereas microbubble “B” has a diameter of 3 μm . Each frame corresponds to a $11 \times 11 (\mu\text{m})^2$ area. 90
- 6.7 A sonoporation event including microbubble dissolution during 11 s of sonication (*left*) and selected frames of the microbubble entering a cell (*right*). Microbubble “A” entered the cell and dissolved, whereas microbubble “B” stuck to the cell membrane. Each frame corresponds to a $23 \times 23 (\mu\text{m})^2$ area. 91
- 6.8 Microbubble of 5- μm diameter apparently penetrating through the cell membrane in optical focus (*left*); z -stack through the entire cell, to record whether the apparent microbubble entry is actually into the cell (*right*). Areas “A” and “C” are regions of interest inside and outside the cell, respectively. Each frame corresponds to a $76 \times 76 (\mu\text{m})^2$ area. 92
- 6.9 Microbubble of 4- μm diameter apparently penetrating through the cell membrane in optical focus (*left*); z -stack through the entire cell, to record whether the apparent microbubble entry is actually into the cell (*right*). Areas “A” and “C” are regions of interest of high fluorescence and low fluorescence, respectively, inside the cell. The white dotted lines in the upper left frame of the right panel indicates the cell membrane. Each frame corresponds to a $52 \times 52 (\mu\text{m})^2$ area. 93
- 6.10 Average fluorescent intensities in the regions of interest (ROI) of Figures 6.8 (*left*) and 6.9 (*right*). Bold lines represent ROI “A” inside the cells, whereas hairlines represent ROI “C” the control regions. The dotted line represents the cell boundary contrast. Note that the cell boundary contrast is maximal just proximal-to-focus. . . 94
- 6.11 Columns ④ and ⑤ represent frames in optical focus from the events in Figures 6.8 and 6.9, respectively, before sonication and approximately 8 minutes after sonication. The white dotted lines in the right frames indicate the cell membrane boundary. The left frames correspond to $76 \times 76 (\mu\text{m})^2$ areas, whereas the right frames correspond to $45 \times 45 (\mu\text{m})^2$ areas. 95

List of publications

Peer-reviewed articles

Kotopoulos S, Wang H, Cochran S, Postema M. Lithium niobate transducers for MRI-guided ultrasonic microsurgery. *IEEE Trans Ultrason Ferroelectr Freq Control* **2011** accepted.

Gerold B,[†] Kotopoulos S,[†] McDougall C, M^cGloin D, Postema M, Prentice P. Laser-nucleated acoustic cavitation in focussed ultrasound. *Rev Sci Instrum* **2011** accepted.

Delalande A, Kotopoulos S, Rovers T, Pichon C, Postema M. Sonoporation at a low mechanical index. *Bub Sci Eng Tech* **2011** 3(1):accepted.

Kotopoulos S, Postema M. Microfoam formation in a capillary. *Ultrasonics* **2010** 50(2):260–268.

Kotopoulos S, Schommartz A, Postema M. Sonic cracking of blue-green algae. *Appl Acoust* **2009** 70(10):1306–1312.

Conference proceedings

Delalande A, Kotopoulos S, Midoux P, Postema M, Pichon C. Investigations of microbubble–cell interactions during the sonoporation process. *Proc 18th Int Congr Sound Vibration* **2011** #4436.

Delalande A, Kotopoulos S, Pichon C, Postema M. Cancer cell sonoporation at low acoustic amplitudes. *Proc 18th Int Congr Sound Vibration* **2011** #4320.

Kotopoulos S, Delalande A, Pichon C, Postema M. On cells and sound. In: Korneliussen RJ, Ed. *Proceedings of the 34th Scandinavian Symposium*

[†]Gerold B and Kotopoulos S share first author responsibility.

on Physical Acoustics, Geilo, Norway, 30 January – 2 February 2011.
Trondheim: Norwegian Physical Society **2011** accepted.

Kotopoulis S, Wang H, Cochran S, Postema M. Lithium niobate ultrasound transducers for high-resolution focussed ultrasound surgery. *Proc IEEE Ultrason Symp* **2010** accepted.

Kotopoulis S, Postema M. Forming morphing microfoam. *Proc Int Congr Acoust* **2010** #25.

Kotopoulis S, Schommartz A, Postema M. Safety radius for algae eradication at 200 kHz–2.5 MHz. *Proc IEEE Ultrason Symp* **2008** 1706–1709.

About the author



Mr. Spiros Kotopoulos was born in Athens, Greece, in 1987. He received a first-class B.Eng. (Hons) in Mechanical Engineering from The University of Hull, Kingston upon Hull, England, in 2008. He is currently pursuing a Ph.D. in the Department of Engineering at the University of Hull under the supervision of Prof. Dr. Michiel Postema. His particular expertise lies in high-speed photography, microscopy, ultrasound transducer manufacture, and sonoporation.

Summary

This thesis treats biomedical ultrasonics, cavitation and sonoporation.

Focussed ultrasound surgery can heat tissue to a temperature that causes protein denaturation and coagulative necrosis. For high-resolution focused ultrasound microsurgery, high working frequencies are necessary. We manufactured a high-frequency, high-intensity focussed ultrasound transducer, using lithium niobate as the active element. The transducer was capable of creating 2.5×3.4 (mm)² lesions without affecting surrounding tissue.

Such disruptive effects of ultrasound also have applications outside medicine. Since cyanobacteria contain gas vesicles, we hypothesised that these can be disrupted with the aid of ultrasound. During 1-hour sonication in the clinical diagnostic range, we forced blue-green algae to sink, thus promoting natural decay.

In medical diagnostics, ultrasound contrast agents are added to the blood stream to differentiate between blood and other tissue types. We injected such lipid-shelled microbubbles into a synthetic capillary and sonicated using continuous ultrasound. The microbubbles formed clusters at a quarter wavelength apart owing to radiation forces. We observed cluster coalescence and translation towards the capillary wall.

To study acoustic cavitation, we designed and built a scientific instrument combining a pulsed laser and a high-intensity focussed ultrasound transducer, capable of nucleating at precise locations. The cavitation dynamics were recorded using high-speed cameras. At high acoustic intensities, interacting cavitation clouds were formed.

Microbubbles under sonication have been observed to create transient pores in adjacent cell membranes. This so called sonoporation has been associated with highly non-linear bubble phenomena. We observed lipid-shelled microbubbles near cancer cells under quasi-continuous low-amplitude sonication. Typically within a second of sonication, microbubbles were seen to enter the cells and dissolve. This new explanation of sonoporation was verified using high-speed photography and confocal fluorescence microscopy.

If drug and genes can be successfully coupled to acoustically active vehicles, sonoporation might revolutionise non-invasive therapy as we know it.